Optofluidic thin-film sensors prepared by Oblique Angle Deposition

CONSEJO SUPERIOR DE INVESTIGACIONES CIENTÍFICAS

Manuel Oliva Ramírez

Instituto de Ciencia de Materiales de Sevilla (US-CSIC)

Universidad de Sevilla

PhD thesis, 2016

Optofluidic thin-film sensors prepared by Oblique Angle Deposition

A dissertation submitted for the degree of

Philosophiæ Doctor (PhD)

Memoria presentada para optar al grado

de Doctor por la Universidad de Sevilla

Seville, January 2016

Manuel Oliva Ramírez

Directed by:

Pr. Agustín Rodríguez González-Elipe
Profesor de Investigación CSIC
Instituto de Ciencia de Materiales de Sevilla
(CSIC-Universidad de Sevilla)

Dr. Francisco Yubero Valencia
Investigador Científico CSIC
Instituto de Ciencia de Materiales de Sevilla
(CSIC-Universidad de Sevilla)

Tutor:

Pr. Alfonso Caballero Martínez
Catedrático Universidad de Sevilla
Dpt. Química Inorgánica
(Universidad de Sevilla)

Index

Chapter 6

Chapter 7

Chapter 1

Introduction

As an emerging field, Optofluidics presents many challenges and opportunities for nanotechnology fabrication methods such as Oblique Angle Deposition (OAD). The goal of the present thesis has been to explore the possibilities of OAD thin films as sensors by means of the comprehension of their optofluidic response.

In this Introduction, we present first a brief overlook on thin films trends and applications and what is the role of OAD thin films on it. Afterward, we explain the preparation of OAD thin films, beginning with the particular geometry of the deposition process and with emphasis on the shadowing effect. Following with a description of their microstructure possibilities, we explore how they lead to the control of the porosity and optical properties.

Once we have introduced OAD thin films, we introduce the field of Optofluidics and how it has emerged taking advantages of the developed techniques of Microfluidics and how it has suppose another step in the concept of “lab on a chip”. Among the several kinds of optofluidic sensors, we introduce the refractive index (RI) sensors and its advantages focusing in the photonic crystals sensors. Finally, we show an optofluidic RI sensor by OAD developed by Lola García et al. (REF) consisting in a porous photonic crystal. This device established the basis of the present thesis.

1.1 Preparation of Oblique Angle Deposition (OAD) thin films.

Surface engineering by thin films deposition is an important technological field thanks to the wide set of applications benefitting from its contributions such as optics and displays, microelectronics and information processing, energy generation and storage, and many other every-day devices. The thin film field covers all these applications not only because of the wide variety of deposited materials, but also due to the possibility of engineering thin film properties through physical structuring at sub-micrometre scales. Control of porosity is a typical example of this capability and, through it, of the optical properties of the films[1–6].

Among the wide variety of available thin films deposition processes, we will focus in electron beam assisted Physical Vapour Deposition (PVD). The term PVD originally appeared in the 1966 book: *Vapor Deposition* by C. F. Powell, J. H. Oxley and J. M. Blocher Jr., although Michael Faraday was already using this technique to deposit coatings as far as 1838. During the deposition of thin films by electron beam evaporation, electrons are produced by a heated wolfram filament in high vacuum conditions and directed to anode of the material intended for evaporation. The electron beam heats the target and causes its partial evaporation in the form of a vapour flux that, upon deposition on a substrate located in a "line of sight" configuration (and on the whole vacuum chamber), produces a deposited layer of the anode material. The controlled deposition rate enabled by this technique offers ideal conditions to achieve a strict structural and morphological control of the deposited thin film as it will be further discussed in this introductory chapter[7].

Within this context, Oblique Angle Deposition (OAD) constitutes a straightforward method to fabricate nanostructured columnar architectures that takes advantage of prevalent physical vapour deposition processes based on evaporation or sputtering. One of the most remarkable aspects of this technique involving tilting and rotating the substrates at the macroscale relies on the three-dimensional precision achievable by the fabrication on nanosculptured arrays[8].

Even though the application of the method was reported by the first time more than a hundred years ago,[9,10] systematic applications of OAD thin films due to their peculiar columnar microstructure and the factors controlling its development were only apparent in the period 1950-1970 [1–6,11]. Thereafter, a renewed interest in this technique has arisen during the last 20-25 years, when the OAD procedure has been systematically utilized for the development of a wide variety of applications and devices requiring a strict control over porosity, anisotropy and/or crystallographic texture of the deposited thin films. Very interesting examples in fields such as sensor technology, photovoltaic cells, magnetism, optical devices, electrochemistry and catalysis can be quoted to prove this assertion[12–22].

1.1.1. Geometry of the deposition process and shadowing effects.

With respect to the substrate, electron beam deposition is a low temperature process and as such thermally activated mobility processes of ad-atoms on the surface are rather limited. This means that the diffusion of particles during the growth of the film becomes negligible, meaning that the vapor particles are incorporated at their point of impact, a process that is usually recognized as ballistic deposition. As a consequence, the main mechanistic factor controlling the nanostructural evolution of the films is a “shadowing effect” that prevents the deposition of particles behind the initially formed nuclei (i.e., shadowed regions)[2,13].

Figure 1.1 presents a scheme of the OAD geometrical configuration during deposition from an e-beam evaporation source. The scheme (**Figure 1.1 a)**) describes the geometrical parameters relevant to the OAD growth, namely the zenithal angle of alignment between the source and the film (α), the azimuthal angle (ϕ) and the polar angles (δ) and (θ). By the approximation of considering a nearly punctual source, the zenithal and azimuthal angles are well defined in e-beam assisted evaporation experiments.

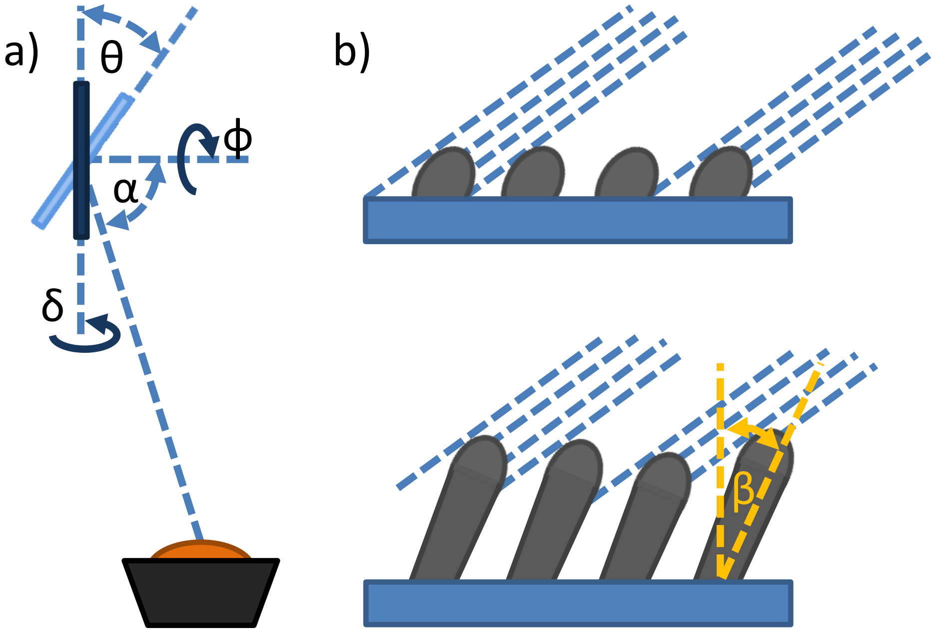

Figure 1.1. OAD deposition process. a) Definition of deposition angles from a punctual source. b) Scheme showing the effect of shadowing during the initial and subsequent stages of deposition and the control mechanism of the tilting angle of the nanocolumns.

Figure1.1 b) illustrates the most basic notions of OAD of thin films[2,12–14] showing than the first nuclei formed during the earliest stages of deposition project a shadow behind them that prevents the deposition of any further evaporated material within the ”shadowed” areas. As the deposition progresses, these nuclei induce the formation of tilted and separated nanocolumns which is the most characteristic feature of OAD thin films. This nanocolumnar arrangement gives rise to some of the outstanding properties of these thin films such as porosity, birefringence and magnetic anisotropy.

The low kinetic energy of the particles when landing onto the surface (the energy of evaporated atoms is around 0.2 eV) excludes kinetic energy-induced processes during the competitive growth of the tilted nanocolumns and supports the relevance the arrival angle of vapour species (α) for the control of the final microstructure of the films[7].

The existence of a direct relationship between the tilt angle of the nanocolumns (β) and the zenithal evaporation angle (α) has been recognized since the early works about OAD thin films and several attempts made to correlate them with simple formulas (see Fig. 1.1(b)). The two most popular heuristic expressions correlating the oblique angle of evaporation and the tilt angle of the nanocolumns are the tangent rule proposed by Nieuwenhuizen and Haanstra[2,4] and the cosine rule proposed by Tait et al.[23] Despite some concordances, none of these heuristic approaches succeed in accounting for the experimental tilting angles, failing for most deposition conditions. Taking into account the interaction between the deposition particles and the surface of the deposited material, Álvarez et al.[24,25] have succeeded in accounting for the dependence between α and β by means of a new concept named “surface trapping mechanism” based on atomistic considerations.

1.1.2 Microstructure and Sculptured thin films.

Figure 1.2 shows some examples of thin films grown by means of OAD varying different geometric parameters. The cross section images in **Figure1.2** a) show the different microstructures obtained during a simple deposition as a function of the deposition angle α. Meanwhile, the top view micrographs included as insets highlight the dependence of film roughness and porosity on the deposition angle α. This columnar morphology typical of OAD thin films converts into more complex thin film microstructures when the substrate of the films moves during deposition. The term/concept “sculptured thin film”, has been coined to describe these thin film topologies in which the orientation and/or width of the nanocolumns adopt a singular forms (e.g., oblique matchsticks, chevrons, multiple zigzags, S’s, C’s, helices and even superhelices) in response to the movement of the substrate during deposition[15]. Ii is remarkable that tailoring the microstructure of these sculptured thin films is used to enhance some specific properties of the films to give rise to new potential applications[18–20].

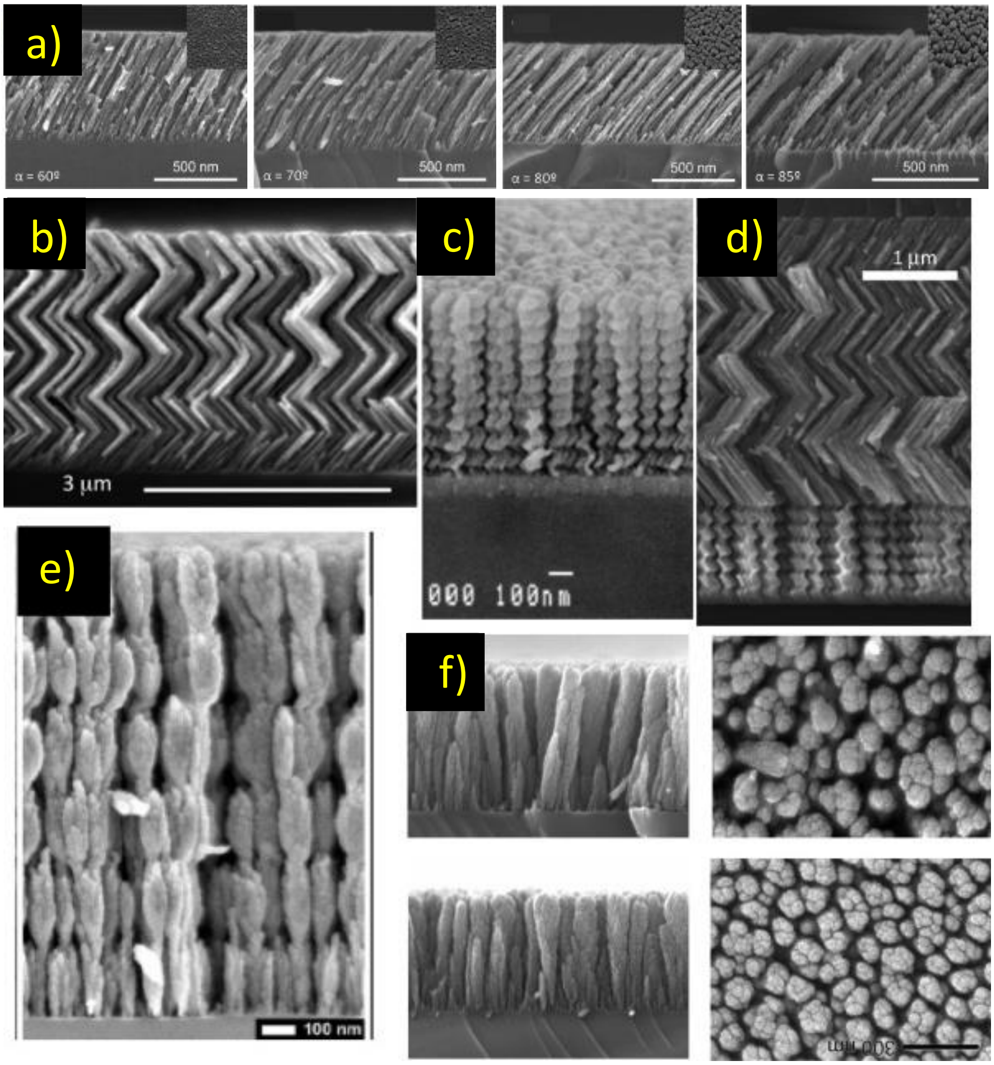

Figure 1.2. Selected SEM micrographs of OAD sculptured TiO_2 thin films. a) Cross sectional and normal (inset) SEM micrographs of a series of TiO_2 thin films e-beam deposited at zenithal angles varying from 60° (left) to 85° (rigth)[26]. Cross sectional SEM images of b) zig-zag nanocolumns obtained by back and forth azimuthal turning of the substrate[27], c) spiral nanocolumns obtained by continuous azimuthal rotation (i.e., dynamic OAD)[28], d) zig-zag plus spiral nanocolumns (author's unpublished results), e) nanocolumns with width modulation obtained by azimuthal rotation and back and forth polar angle tilting[23], and f) vertical nanocolumns obtained by rapid azimuthal rotation at two different rates[29].

Typical sculptured thin films are obtained by changing, either alternatively or simultaneously, the zenithal (α), azimuthal (φ) and/or polar (θ) angles (c.f., **Figure 1.1 a)**) to alter the incoming direction of the vapour flux during growth. Combinations of different materials have been also reported during the fabrication of sculptured thin films[30]. In all cases, shadowing effects are considered as one of the main factors determining the appearance of the large variety of nanocolumnar morphologies obtained. Some examples are presented in **Fig. 1.2** b) showing a series of selected SEM micrographs of TiO_2 thin films depicting different morphologies resulting from tilting and/or rotation of the substrate during the deposition. Brett et al.[18,19] and other authors[27–29,31–57] have carried out a systematic work in this area and proved the possibility of controlling the film morphology by systematically moving the substrate during deposition.

1.2. Porosity and optical properties of OAD Thin Films.

Optical properties of OAD thin films are closely related not only with their composition but also their microstructure. One of the possibilities brought about by the oblique deposition configuration is the tunability of the refractive index of the films by tuning their porosity/density which, in turn, can be controlled by the deposition angle α. Bruggeman's and Maxwell-Garnett's models based on the effective medium approximation have been used to estimate an effective refractive index $\mathbf{n}_{\text{eff}}$ depending on the porosity and composition of the thin films. Thanks to the high porosity achievable by OAD, thin films with very low refractive indices can be fabricated[54–57].

Another outstanding property stemming from the tilting nanocolumnar structure of OAD thin films is their optical anisotropy, an effect well-known since the earliest studies on this matter[5,6]. Thus, even if at atomic scale the constituent material is isotropic, asymmetric columnar structure, lateral connectivity and bundling association[12,58] of nanocolumns may contribute to induce the development of an anisotropic optical response[32,59]. Light propagation through these film exhibits a polarization-sensitive behavior which is often exploited in optical devices such as polarizers or waveplates. In the natural world it is quite common to find optical anisotropic materials, as the Iceland spar (a type of calcite) where their intrinsic birefringence only depends on the type of material not on its mesoscopic structure as it happens with OAD thin films.

Figure 1.3 shows some examples of the microstructure of anisotropic and isotropic thin films prepared by OAD, together with a schematic description of their optical behavior using a refractive index ellipsoid**.** The anisotropic OAD thin films depicted in **Figures1.3** a) and b) are characterized by a tilted columnar shape (side view) and a larger growth in a particular direction (down column axis view). As a result of this asymmetry, we can see in **Figure 1.3 c)** the biaxial anisotropy of its corresponding refractive index ellipsoid accounting for a surface optical anisotropy for these OAD thin films. On the other hand, **Figure 1.3 d)** and **e)** present a vertical oriented OAD thin film microstructure as an example of an isotropic morphology. In this case the rotational symmetry in the surface plane yields a symmetric refractive index ellipsoid (**Figure1.3 f)**) accounting for an optically isotropic thin film.

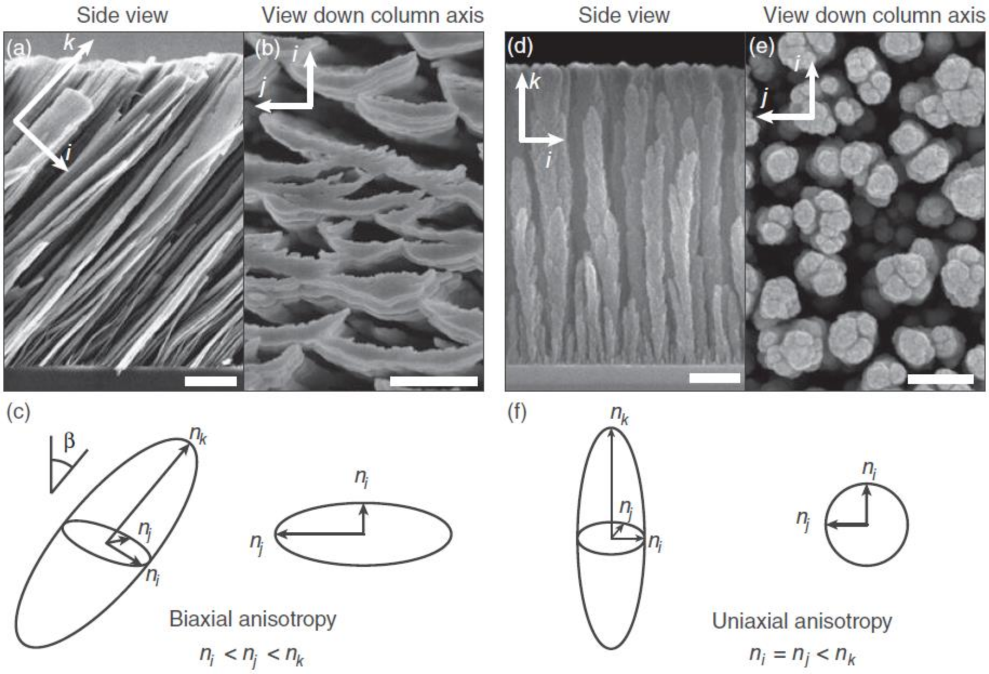

Figure 1.3. Cross sectional and top view SEM micrographs of TiO_2 thin films prepared by OAD: a) & b) anisotropic and d) & e) isotropic microstructures. c) & d) Schemes of the refractive index ellipsoids of these microstructures.

The optical anisotropy in OAD thin films can be easily described by means of a planar birefringence, defined as the difference between the refractive index along a slow axis and a fast axis with respect to a light beam impinging at normal incidence on the film surface. This difference will be zero in the case of isotropic materials (as the reported in **Figure 1.3 d**) and **e)**) but have a non zero value for anisotropic materials (**Figure 1.3 a)** and **b)**). In general, the planar birefringence can be written as:

$$\Delta\lambda = n_s - n_f$$

As an example, **Figure 1.4** shows the evolution of the planar birefringence as a function of the deposition angle α for TiO2 thin films prepared by OAD[60]. Planar birefringence of another inorganic oxides deposited by OAD have been reported in the literature[8,59]. The series of top view SEM micrographs and the corresponding Fourier transforms included as insets highlight the anisotropic growth of some of these films.

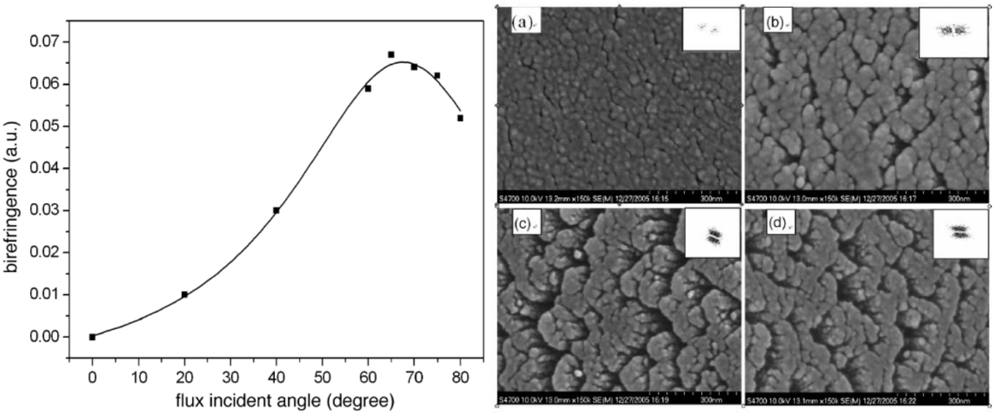

Figure 1.4. Left) Birefringence of GLAD TiO2 films at different flux angles. Right) Top view SEM images of GLAD TiO2 films. (a) $\alpha=60^{\circ}$; (b) $\alpha=70^{\circ}$; (c) $\alpha=75^{\circ}$; (d) $\alpha=80^{\circ}$. Inset is a two dimensional FFT of the corresponding surface images.

1.3. Optofluidics.

Optofluidics, as described by the name, describes an emerging field integrating optics with fluidics and, more specifically, the synergistic integration of photonics and microfluidics. Although liquid enabled optical devices, such as the liquid mirror telescope[61] or dye lasers[62], were invented a long time ago, the term *Optofluidics* was only adopted after the successful efforts in the area of microfluidics by many optical and microfluidic groups worldwide[63-73]. In particular, following the miniaturization and integration works in the semiconductor field, the microfluidics area emerged in the early 1990s when researchers saw the potential of developing the 'lab on a chip'[74,75] concept. Some of the first successful steps towards the development of integrated devices involved the incorporation of optical elements such as waveguides[76] and plasmonic surfaces[77] together with the microfluidic channels. Thus, new concepts for using microfluidic elements as a fundamental part of photonic devices start to emerge in the early 2000s with the development of technologies such as the bubble switch[78], liquid-crystal switchable gratings[79] and microfluidically tunable photonic crystal fibers[80]. In the mid-2000s these research directions began to merge into the new field of '*Optofluidics*'.

The significance of fluids for an efficient control of optical performance of devices stands from their unique properties that, overpassing those of equivalent solid materials, can be used to design and fabricate astonishing novel optical systems. Examples of such properties include the optically smooth interface formed between two immiscible fluids; the ability of flowing streams of miscible fluids to create gradients in optical properties by diffusion; and the ability to change the optical property of a fluid medium within a device by simply replacing a liquid by another.

The two major advantages of *Optofluidics* are associated with the concepts of integration and reconfigurability. Although photonics has long been used to study non-solid materials such as liquids, traditionally the fluidic media have not comprised any functional part of the photonic device or system. However, *Optofluidics* has significantly progressed in the integration of liquids as optical components enabling new photonic functionalities and devices that were previously impossible[81]. In addition, *Optofluidics* permits the fast and tailored change in the optical properties of the devices by fluidic reconfigurability[82–86].

These unique features of *Optofluidics* provided by the integration and management of non-solid media are well-suited for a broad range of applications as photonic components, optical manipulation[81] and energy systems[87]. In particular, *Optofluidics* is well-suited for biological and chemical analysis and analysis of extremely small detection volumes (femtoliters to nanoliters) because it enables small-volume sample handling and it even makes possible to integrate sample preparation and delivery within a single analytical mechanism[88]. These enhanced analytical capabilities rely on singular optical properties of fluids such as refractive index (RI), fluorescence, Raman scattering, absorption or polarization that exploited individually or in combination, can be used to generate the sensing signal.

1.3.1. Optofluidic Refractive Index (RI) sensors.

One of the most popular liquid analysis methods used in optofluidic sensors consists of measuring the RI of a liquid sample. The label-free character of this method is the main advantage with respect to fluorescence labelling. Optofluidic RI sensors measure the changes in refractive index of a bulk solution due to the presence of dissolved analytes with a different RI (or excess polarizability) from that of the background solvent. RI detection is particularly attractive for the analysis of extremely small volumes because this is an intensive magnitude which scales up with the analyte concentration, rather than with the total number of molecules. To enable the detection of an ultralow quantity of molecules, many optofluidic RI photonic sensors confine the electric field into a small volume (femtolitres to nanolitres). Looking for maximizing the light-analyte interaction under these conditions, various optofluidic architectures, including metallic nanohole-array-based plasmonics[89–94] (Fig. 1.5 a)), photonic crystals and photonic crystal fibers[95–105] (Fig. 1.5 b), c)), interferometric structures such as ring resonators[106–111] (Fig. 1.5 d), e)), Mach–Zehnder interferometers[112,113] and Fabry–Pérot cavities[114–117] (Fig. 1.5 f)) have been explored.

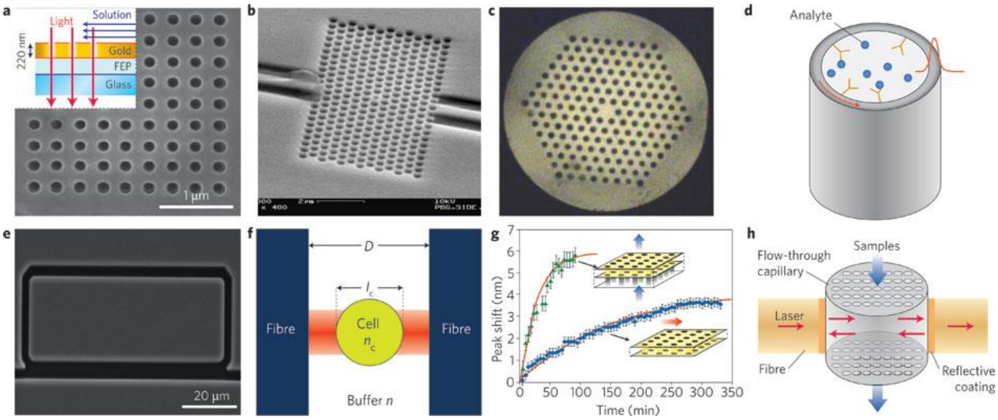

Figure 1.5. Examples of photonic structures used for RI analysis of liquids. a) Metallic nanohole-array-based plasmonic sensor[91]. b) Dielectric planar photonic crystal sensor[98]. c) PCF-based sensor[101]. d) Capillary-based OFRR sensor. e) ARROW-based OFRR[111]. f) Fabry–Pérot interferometric sensor for cell detection[113]. g) Flow-through and flow-over plasmonic sensors, together with each system's sensing response[89]. h) Fabry–Pérot sensor with flow-through micro- and nanofluidic channels[114].

Optofluidic RI sensors based on plasmonics, photonic crystals or photonic crystals fibers are primarily composed of periodic metallic or dielectric structures that are used to confine and guide the light (Fig. 1.5 a)-c)). Inherently, the voids in these structures are excellent microfluidic channels that can be filled with liquid samples for liquid sensing. Although ultra-small volumes could be detected, in practice, higher volumes are needed because of the rudimentary nature of the sample delivery systems, which are often unable to selectively deliver the analyte at the locations of the photonic structure where the light–matter interaction is stronger.

Other reported optofluidic techniques integrate a photonic device with a microfluidic channel for simple and repeatable sample delivery. The optofluidic ring resonator (OFRR)[106–111] (Fig. 1.5 d),e)) and the Fabry–Pérot cavity sensor[115–117] are examples of such optofluidic configuration. In some cases, the microfluidic channel forms part of the photonic structure to avoid the problem of transporting a large number of target molecules to the sensor surface. Very recently, researchers replaced this 'flow-over' technique, where the fluid infiltrates the porous structure by diffusion, by an optofluidic 'flow-through' strategy to mitigate the slow mass-transport issues constraining the use of most optical sensors. This optofluidic technique integrates nanofluidic channels through the optical sensing structure such that the entire sample interacts directly with the sensing surface. Mass transport to the sensing surface is almost entirely convective (instead of diffusive), which provides a stronger signal in significantly shorter time than in the conventional flow-over sensor. An example of this kind of devices based on arrays of nanoholes consists of plasmonic nanofluidic sensors and photonic crystal nanofluidic sensors fabricated by photolithography as exhibits **Figure 1.5 g)**[89,93–95]. The wafer substrate is back-etched for the liquid to pass through a thin (~100 nm) holey metal or dielectric membrane. An outstanding development in this domain was due to Guo et al. who developed an alternative flow-through system, (c.f., Fig. 1.5 h)[114]. The functioning of this optonanofluidic sensor concept is similar to that of the nanoporous sensors[118,119] except in that it uses well-defined flow-through holes fabricated using the fiber drawing method.

1.3.2. Optofluidic planar RI structures prepared by OAD of thin films.

OAD is a suitable technique for the preparation of highly uniform and reflecting planar Bragg mirrors as evidenced by notorious examples of conducting[120] and photoconducting[121] Bragg stacks made of a single type of oxide (e.g., TiO2 or ITO, respectively) deposited by this method. In these stacked layers, a periodic refractive index variation was achieved by modulating the porosity of the films along the stacking direction. These systems present a potential interest as sensing materials, since they combine an accessible porosity with well-defined optical properties that are predictively modulated when exposed to different relative humidity environments[122]. Lola García et al. presented by the first time the fabrication a of a Bragg mirror by OAD combining two different materials (SiO2 and TiO2) that kept the connectivity of the intercolumnar pores through the alternate layers of the structure [30] (**Figure 1.6**). To enhance the uniformity of the Bragg mirror, they used an azimuthal rotation of the substrate from one layer to the next leading to a zigzag shape of the nanocolumns, (**Figure 1.6 a)** and **b)**). IN this preliminary work with liquids, the accessibility and good connectivity of the porous network of the multilayer made than when they are filled with liquids of different refractive indices the spectral position of the Bragg reflection linearly red-shifts, as can be observed in **Figure 1.6 c)** and d). The potential use of similar OAD thin films and stacks as sensors, as well as a deeper study of their optofluidics properties and of their applications for liquid analysis will be the subject of this thesis work.

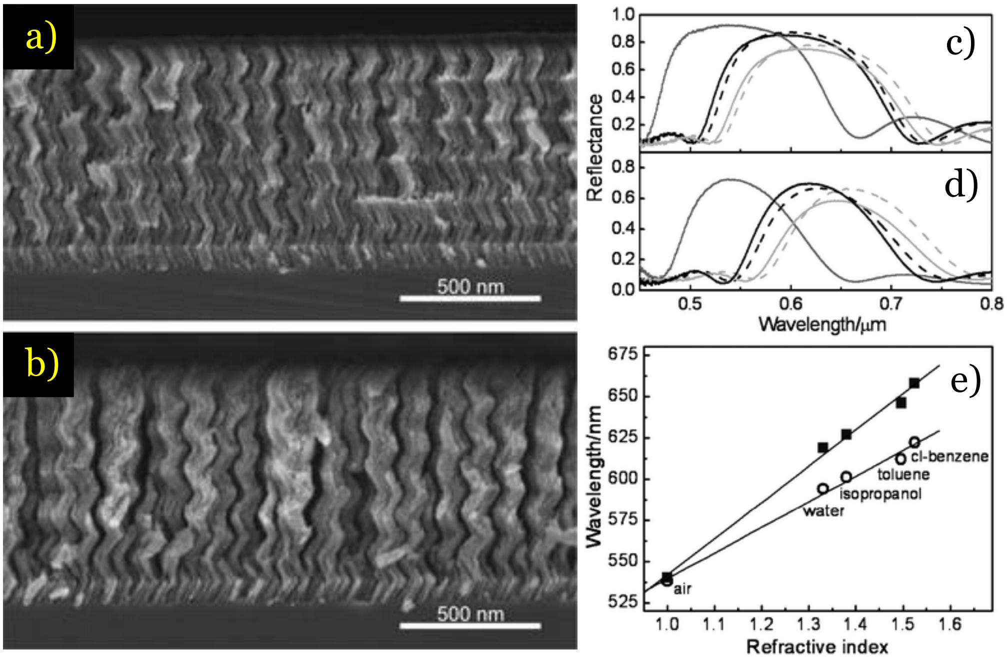

Figure 1.6. Cross sectional SEM micrographs of TiO2–SiO2 multilayers prepared by OAD at a) α =60° and b) α =85°. Normal incidence specular reflectance spectra of these multilayers: c) α = 60° and d) α = 85°. Each curve corresponds to a different fluid filling the voids, namely, air (dark grey solid line), water (black solid line), isopropanol (black dashed line), toluene (light grey solid line), Cl-benzene (light grey dashed line). e) A plot of the spectral position at which the maximum Bragg reflection is observed versus the refractive index of the infiltrated liquid.

1.4. Objectives

The main aims of this thesis have been to explore the opportunities of PVD-OAD thin films in *Optofluidics* and the development of transductors for their implementation in optofluidics sensors for liquid analysis. These aims have been developed through the chapters of this thesis in more specifics items as follows:

- To prove that the optical properties of porous OAD microcavities can be accurately controlled without incurring in light dispersion effects very common when dealing with other type of porous materials.
- To integrated OAD porous structures in the form of planar microfluidic components through which liquids can circulate easily.
- To use planar Bragg microcavities, made by stacking several porous TiO_2 and SiO_2 OAD thin films, as efficient optofluidic responsive systems for measuring the solute concentrations of liquid solutions or for the analysis of liquid mixtures.
- To model the optical response of this PVD-OAD BM when infiltrating with liquids and tilting by using a conventional interference optical model.
- To fabricate polarization active systems behaving as wavelength dependent retarders in the form of two-oxide BMs prepared by PVD-OAD.
- To determine the nanostructural features responsible for the polarization activity of these porous BM.
- To study the systematic and continuous control of polarization activity in BM by PVD-OAD by adjusting the refractive index of the liquids circulating through these porous layer structures.
- To develop a simple optical model considering the degree of birefringence of each particular layer in the stack and its variation with the refractive index of the liquid filling the pores.
- To carry out a thorough and critical study of the different analytical possibilities of the synthesized PVD-OAD BMs, are they optically active or inactive.
- To measure colored solutions characterized by a high absorption band coefficient by means of the anomalous refractive index dispersion using a PVD-OAD BM.

1.5. Scheme of the thesis.

Optofluidic thin-film sensors prepared by Oblique Angle Deposition

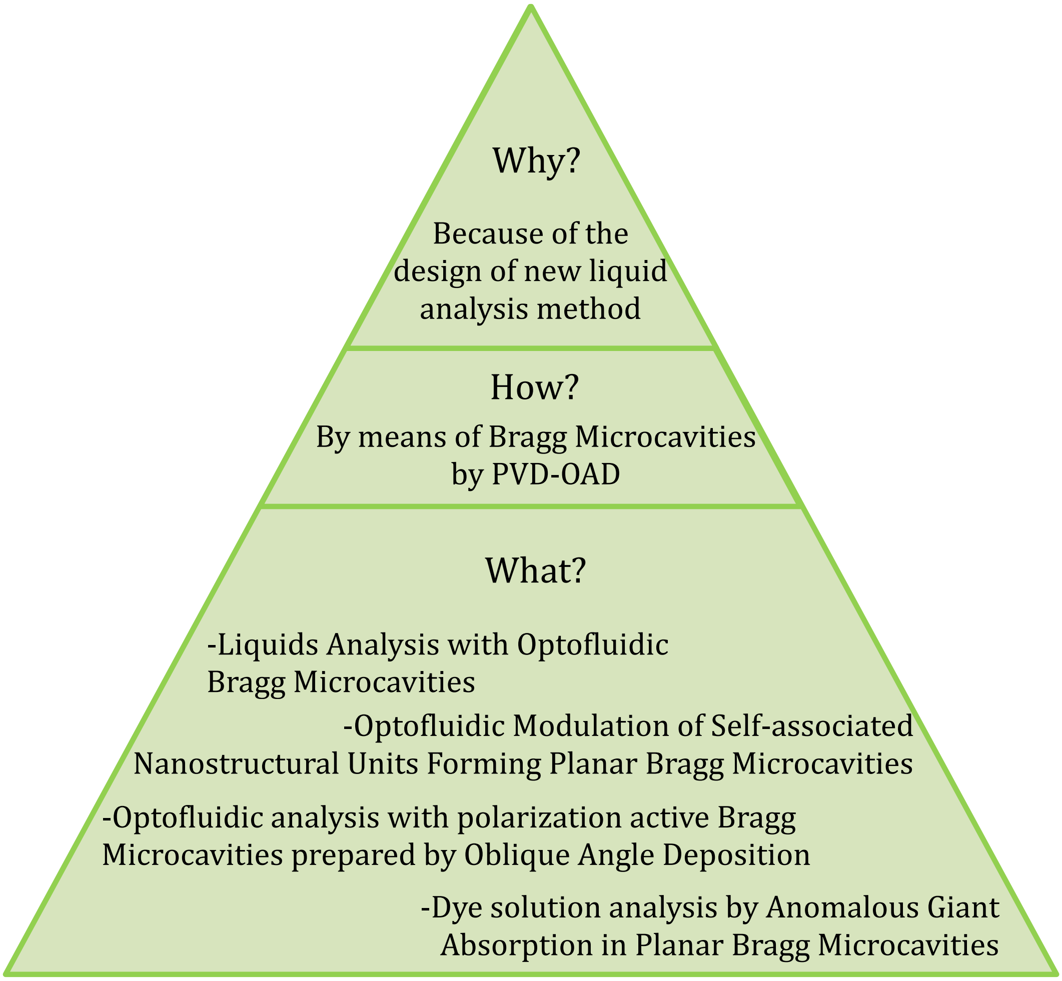

1.6. References

1. Smith, D. O., Cohen, M. S. & Weiss, G. P. Oblique-Incidence Anisotropy in Evaporated Permalloy Films. *J. Appl. Phys.* **31,** 1755–1762 (1960).
2. Dirks, A. G. & Leamy, H. J. Columnar microstructure in vapor-deposited thin films. *Thin Solid Films* **47,** 219–233 (1977).
3. Young, N. O. & Kowal, J. Optically Active Fluorite Films. *Nature* **183,** 104–105 (1959).
4. J.M. Nieuwenh & H.B. Haanstra. Microfractography of thin films. *Philips Tech Rev* **27,** 87–91 (1966).
5. Lewis, B. & Campbell, D. S. Nucleation and Initial-Growth Behavior of Thin-Film Deposits. *J. Vac. Sci. Technol.* **4,** 209–218 (1967).
6. Nakhodkin, N. G. & Shaldervan, A. I. Effect of vapour incidence angles on profile and properties of condensed films. *Thin Solid Films* **10,** 109–122 (1972).
7. Poxson, D. J., Mont, F. W., Schubert, M. F., Kim, J. K. & Schubert, E. F. Quantification of porosity and deposition rate of nanoporous films grown by oblique-angle deposition. *Appl. Phys. Lett.* **93,** 101914 (2008).
8. Hawkeye, M. M., Taschuk, M. T. & Brett, M. J. in *Glancing Angle Deposition of Thin Films* 173–225 (John Wiley & Sons, Ltd, 2014). at <http://onlinelibrary.wiley.com/doi/10.1002/9781118847510.ch5/summary>
9. Kaempf, K. Grösse und ursache der doppelbrechung in kundtschenspiegeln und erzeugung von doppelbrechung in metallspiegelndurch zug. *Ann Phys* **321,** 308–333 (1905).
10. Bergholm, C. Über Doppelbrechung in kathodenzerstäubten Metallschichten. *Ann. Phys.* **348,** 1–23 (1913).
11. H. König & G. Helwig. Über die struktur schrägaufgedampfter schichten und ihr einfluß auf die entwicklung submikroskopischer oberflächen rauhigkeiten. *Optik* **6,** 111–124 (1950).
12. van Kranenburg, H. & Lodder, C. Tailoring growth and local composition by oblique-incidence deposition: a review and new experimental data. *Mater. Sci. Eng. R Rep.* **11,** 295–354 (1994).
13. Abelmann, L. & Lodder, C. Oblique evaporation and surface diffusion. *Thin Solid Films* **305,** 1–21 (1997).
14. Robbie, K. & Brett, M. J. Sculptured thin films and glancing angle deposition: Growth mechanics and applications. *J. Vac. Sci. Technol. A* **15,** 1460–1465 (1997).
15. Messier, R., Venugopal, V. C. & Sunal, P. D. Origin and evolution of sculptured thin films. *J. Vac. Sci. Technol. A* **18,** 1538–1545 (2000).
16. Wadley, H. N. G., Zhou, X., Johnson, R. A. & Neurock, M. Mechanisms, models and methods of vapor deposition. *Prog. Mater. Sci.* **46,** 329–377 (2001).
17. Zhao, Y., Ye, D., Wang, G.-C. & Lu, T.-M. Designing nanostructures by glancing angle deposition. in **5219,** 59–73 (2003).

18. Hawkeye, M. M. & Brett, M. J. Glancing angle deposition: Fabrication, properties, and applications of micro- and nanostructured thin films. *J. Vac. Sci. Technol. A* **25,** 1317–1335 (2007).
19. M.T. Taschuk, M.M. Hawkeye & M.J. Brett. *Glancing angle deposition P.M. Martin (Ed.), Handbook of deposition technologies for films and coatings (3rd ed.),*. (Elsevier, 2010).
20. Tawfick, S. *et al.* Engineering of Micro- and Nanostructured Surfaces with Anisotropic Geometries and Properties. *Adv. Mater.* **24,** 1628–1674 (2012).
21. He, Y. & Zhao, Y. Advanced multi-component nanostructures designed by dynamic shadowing growth. *Nanoscale* **3,** 2361–2375 (2011).
22. Sculptured Thin Films: Nanoengineered Morphology and Optics | (2005) | Lakhtakia | Publications | Spie. at <http://spie.org/Publications/Book/585322>
23. Tait, R. N., Smy, T. & Brett, M. J. Modelling and characterization of columnar growth in evaporated films. *Thin Solid Films* **226,** 196–201 (1993).
24. Alvarez, R. *et al.* Nanocolumnar growth of thin films deposited at oblique angles: Beyond the tangent rule. *J. Vac. Sci. Technol. B* **32,** 041802 (2014).
25. Álvarez, R. *et al.* Theoretical and experimental characterization of TiO 2 thin films deposited at oblique angles. *J. Phys. Appl. Phys.* **44,** 385302 (2011).
26. Lola González-García, J. P.-B. Correlation lengths, porosity and water adsorption in TiO_2 thin films prepared by glancing angle deposition. *Nanotechnology* **23,** 205701 (2012).
27. González-García, L., González-Valls, I., Lira-Cantu, M., Barranco, A. & González-Elipe, A. R. Aligned TiO2 nanocolumnar layers prepared by PVD-GLAD for transparent dye sensitized solar cells. *Energy Environ. Sci.* **4,** 3426–3435 (2011).
28. Suzuki, M. Practical applications of thin films nanostructured by shadowing growth. *J. Nanophotonics* **7,** 073598–073598 (2013).
29. Gaillard, Y., Rico, V. J., Jimenez-Pique, E. & González-Elipe, A. R. Nanoindentation of TiO 2 thin films with different microstructures. *J. Phys. Appl. Phys.* **42,** 145305 (2009).
30. González-García, L., Lozano, G., Barranco, A., Míguez, H. & González-Elipe, A. R. TiO2–SiO2 one-dimensional photonic crystals of controlled porosity by glancing angle physical vapour deposition. *J. Mater. Chem.* **20,** 6408–6412 (2010).
31. Wong, M.-S., Lee, M.-F., Chen, C.-L. & Huang, C.-H. Vapor deposited sculptured nano-porous titania films by glancing angle deposition for efficiency enhancement in dye-sensitized solar cells. *Thin Solid Films* **519,** 1717–1722 (2010).
32. Popta, A. C. van, Cheng, J., Sit, J. C. & Brett, M. J. Birefringence enhancement in annealed TiO2 thin films. *J. Appl. Phys.* **102,** 013517 (2007).

33. Lintymer, J., Martin, N., Chappé, J.-M., Delobelle, P. & Takadoum, J. Influence of zigzag microstructure on mechanical and electrical properties of chromium multilayered thin films. *Surf. Coat. Technol.* **180-181,** 26–32 (2004).
34. Lintymer, J., Martin, N., Chappé, J.-M., Delobelle, P. & Takadoum, J. Nanoindentation of chromium zigzag thin films sputter deposited. *Surf. Coat. Technol.* **200,** 269–272 (2005).
35. Lintymer, J., Martin, N., Chappé, J.-M., Takadoum, J. & Delobelle, P. Modeling of Young's modulus, hardness and stiffness of chromium zigzag multilayers sputter deposited. *Thin Solid Films* **503,** 177–189 (2006).
36. Lintymer, J., Martin, N., Chappe, J.-M. & Takadoum, J. Glancing angle deposition to control microstructure and roughness of chromium thin films. *Wear* **264,** 444–449 (2008).
37. Hrudey, P. C. P., Westra, K. L. & Brett, M. J. Highly Ordered Organic Alq3 Chiral Luminescent Thin Films Fabricated by Glancing-Angle Deposition. *Adv. Mater.* **18,** 224–228 (2006).
38. Broughton, J. N. & Brett, M. J. Electrochemical Capacitance in Manganese Thin Films with Chevron Microstructure. *Electrochem. Solid-State Lett.* **5,** A279–A282 (2002).
39. Hrudey, P. C. P., Taschuk, M., Tsui, Y. Y., Fedosejevs, R. & Brett, M. J. Optical properties of porous nanostructured Y2O3:Eu thin films. *J. Vac. Sci. Technol. A* **23,** 856–861 (2005).
40. Hrudey, P. C. P., Taschuk, M., Tsui, Y. Y., Fedosejevs, R. & Brett, M. J. Effects of film structure on photoluminescent emission properties of nanostructured Y2O3:Eu thin films. in **5510,** 78–87 (2004).
41. Fan, B., Vithana, H. K. M., Kralik, J. C. & Faris, S. M. Optical circular dichroism of vacuum-deposited film stacks. *Opt. Commun.* **147,** 265–268 (1998).
42. Liu, F. *et al.* The growth of nanoscale structured iron films by glancing angle deposition. *J. Appl. Phys.* **85,** 5486–5488 (1999).
43. Krause, K. M. & Brett, M. J. Spatially Graded Nanostructured Chiral Films as Tunable Circular Polarizers. *Adv. Funct. Mater.* **18,** 3111–3118 (2008).
44. Elias, A. L., Harris, K. D. & Brett, M. J. Fabrication of helically perforated gold, nickel, and polystyrene thin films. *J. Microelectromechanical Syst.* **13,** 808–813 (2004).
45. Popta, A. C. van, Brett, M. J. & Sit, J. C. Double-handed circular Bragg phenomena in polygonal helix thin films. *J. Appl. Phys.* **98,** 083517 (2005).
46. Huang, Z., Harris, K. D. & Brett, M. J. Morphology Control of Nanotube Arrays. *Adv. Mater.* **21,** 2983–2987 (2009).
47. Taschuk, M. T., Harris, K. D., Smetaniuk, D. P. & Brett, M. J. Decoupling sensor morphology and material: Atomic layer deposition onto nanocolumn scaffolds. *Sens. Actuators B Chem.* **162,** 1–6 (2012).
48. Woo, S.-H. & Hwangbo, C. K. Optical anisotropy of TiO2 and MgF2 thin films prepared by glancing angle deposition. *J. Korean Phys. Soc.* **49,** 2136–2142 (2006).

49. Leontyev, V. *et al.* Selective transmittance of linearly polarized light in thin films rationally designed by FDTD and FDFD theories and fabricated by glancing angle deposition. *J. Appl. Phys.* **104,** 104302 (2008).
50. Hawkeye, M. M. & Brett, M. J. Narrow bandpass optical filters fabricated with one-dimensionally periodic inhomogeneous thin films. *J. Appl. Phys.* **100,** 044322 (2006).
51. Leontyev, V., Hawkeye, M., Kovalenko, A. & Brett, M. J. Omnidirectional reflection from nanocolumnar TiO2 films. *J. Appl. Phys.* **112,** 084317 (2012).
52. Robbie, K., Cui, Y., Elliott, C. & Kaminska, K. Oxidation of evaporated porous silicon rugate filters. *Appl. Opt.* **45,** 8298 (2006).
53. Yan, X. *et al.* Electrically conductive thin-film color filters made of single-material indium-tin-oxide. *J. Appl. Phys.* **109,** 103113 (2011).
54. Schulz, U., Terry, S. G. & Levi, C. G. Microstructure and texture of EB-PVD TBCs grown under different rotation modes. *Mater. Sci. Eng. A* **360,** 319–329 (2003).
55. Wada, K., Yamaguchi, N. & Matsubara, H. Effect of substrate rotation on texture evolution in ZrO2-4 mol.% Y2O3 layers fabricated by EB-PVD. *Surf. Coat. Technol.* **191,** 367–374 (2005).
56. Wada, K., Yoshiya, M., Yamaguchi, N. & Matsubara, H. Texture and microstructure of ZrO2-4mol% Y2 O3 layers obliquely deposited by EB-PVD. *Surf. Coat. Technol.* **200,** 2725–2730 (2006).
57. Chen, L., Lu, T.-M. & Wang, G.-C. Biaxially textured Mo films with diverse morphologies by substrate-flipping rotation. *Nanotechnology* **22,** 505701 (2011).
58. Stagon, S. P., Huang, H., Baldwin, J. K. & Misra, A. Anomaly of film porosity dependence on deposition rate. *Appl. Phys. Lett.* **100,** 061601 (2012).
59. Hodgkinson, I., Wu, Q. hong & Hazel, J. Empirical Equations for the Principal Refractive Indices and Column Angle of Obliquely Deposited Films of Tantalum Oxide, Titanium Oxide, and Zirconium Oxide. *Appl. Opt.* **37,** 2653 (1998).
60. Wang, S. *et al.* Structural and optical properties of nanostructured TiO2 thin films fabricated by glancing angle deposition. *J. Alloys Compd.* **431,** 287–291 (2007).
61. Borra, E. F. The case for a liquid mirror in a lunar-based telescope. *Astrophys. J.* **373,** 317–321 (1991).
62. F. J. Duarte & L. W. Hillman. *Dye Laser Principles*. (Academic, 1990). at <http://www.tunablelasers.com/dlp.htm>
63. Studer, V. *et al.* Scaling properties of a low-actuation pressure microfluidic valve. *J. Appl. Phys.* **95,** 393–398 (2004).
64. Unger, M. A., Chou, H.-P., Thorsen, T., Scherer, A. & Quake, S. R. Monolithic Microfabricated Valves and Pumps by Multilayer Soft Lithography. *Science* **288,** 113–116 (2000).
65. Thorsen, T., Maerkl, S. J. & Quake, S. R. Microfluidic Large-Scale Integration. *Science* **298,** 580–584 (2002).

66. Squires, T. M. & Quake, S. R. Microfluidics: Fluid physics at the nanoliter scale. *Rev. Mod. Phys.* **77,** 977–1026 (2005).
67. Hong, J. W. & Quake, S. R. Integrated nanoliter systems. *Nat. Biotechnol.* **21,** 1179–1183 (2003).
68. Weibel, D. B. *et al.* Torque-actuated valves for microfluidics. *Anal. Chem.* **77,** 4726–4733 (2005).
69. Nguyen, N.-T. & Wu, Z. Micromixers—a review. *J. Micromechanics Microengineering* **15,** R1 (2005).
70. Günther, A., Jhunjhunwala, M., Thalmann, M., Schmidt, M. A. & Jensen, K. F. Micromixing of Miscible Liquids in Segmented Gas−Liquid Flow. *Langmuir* **21,** 1547–1555 (2005).
71. Garstecki, P., Fischbach, M. A. & Whitesides, G. M. Design for mixing using bubbles in branched microfluidic channels. *Appl. Phys. Lett.* **86,** 244108 (2005).
72. Yeshaiahu Fainman, Demetri Psaltis & Changhuei Yang. *Optofluidics: Fundamentals, Devices, and Applications*. (The McGraw-Hill Companies). at <http://accessengineeringlibrary.com/browse/optofluidics-fundamentals-devices-and-applications#fullDetails>
73. Psaltis, D., Quake, S. R. & Yang, C. Developing optofluidic technology through the fusion of microfluidics and optics. *Nature* **442,** 381–386 (2006).
74. Manz, A., Graber, N. & Widmer, H. M. Miniaturized total chemical analysis systems: A novel concept for chemical sensing. *Sens. Actuators B Chem.* **1,** 244–248 (1990).
75. Harrison, D. J. *et al.* Micromachining a miniaturized capillary electrophoresis-based chemical analysis system on a chip. *Science* **261,** 895–897 (1993).
76. Pawlak, M. *et al.* Zeptosens' protein microarrays: A novel high performance microarray platform for low abundance protein analysis. *PROTEOMICS* **2,** 383–393 (2002).
77. Jin-Lee, H., Goodrich, T. T. & Corn, R. M. SPR imaging measurements of 1-D and 2-D DNA microarrays created from microfluidic channels on gold thin films. *Anal. Chem.* **73,** 5525–5531 (2001).
78. Uebbing, J. J., Hengstler, S., Schroeder, D., Venkatesh, S. & Haven, R. Heat and Fluid Flow in an Optical Switch Bubble. *J. Mems* **15,** 1528–1539 (2006).
79. Wang, X., Wilson, D., Muller, R., Maker, P. & Psaltis, D. Liquid-Crystal Blazed-Grating Beam Deflector. *Appl. Opt.* **39,** 6545 (2000).
80. Mach, P. *et al.* Tunable microfluidic optical fiber. *Appl. Phys. Lett.* **80,** 4294–4296 (2002).
81. Schmidt, H. & Hawkins, A. R. The photonic integration of non-solid media using optofluidics. *Nat. Photonics* **5,** 598–604 (2011).
82. Erickson, D., Rockwood, T., Emery, T., Scherer, A. & Psaltis, D. Nanofluidic tuning of photonic crystal circuits. *Opt. Lett.* **31,** 59 (2006).

83. Karnutsch, C. *et al.* Temperature stabilization of optofluidic photonic crystal cavities. *Appl. Phys. Lett.* **94,** 231114 (2009).
84. Grillet, C. *et al.* Reconfigurable photonic crystal circuits. *Laser Photonics Rev.* **4,** 192–204 (2010).
85. Dong, L., Agarwal, A. K., Beebe, D. J. & Jiang, H. Adaptive liquid microlenses activated by stimuli-responsive hydrogels. *Nature* **442,** 551–554 (2006).
86. Groisman, A. *et al.* Optofluidic 1x4 Switch. *Opt. Express* **16,** 13499 (2008).
87. Erickson, D., Sinton, D. & Psaltis, D. Optofluidics for energy applications. *Nat. Photonics* **5,** 583–590 (2011).
88. Fan, X. & White, I. M. Optofluidic microsystems for chemical and biological analysis. *Nat. Photonics* **5,** 591–597 (2011).
89. Eftekhari, F. *et al.* Nanoholes As Nanochannels: Flow-through Plasmonic Sensing. *Anal. Chem.* **81,** 4308–4311 (2009).
90. Pang, L., Hwang, G. M., Slutsky, B. & Fainman, Y. Spectral sensitivity of two-dimensional nanohole array surface plasmon polariton resonance sensor. *Appl. Phys. Lett.* **91,** 123112 (2007).
91. Yang, J.-C., Ji, J., Hogle, J. M. & Larson, D. N. Metallic Nanohole Arrays on Fluoropolymer Substrates as Small Label-Free Real-Time Bioprobes. *Nano Lett.* **8,** 2718–2724 (2008).
92. Im, H., Lesuffleur, A., Lindquist, N. C. & Oh, S.-H. Plasmonic Nanoholes in a Multichannel Microarray Format for Parallel Kinetic Assays and Differential Sensing. *Anal. Chem.* **81,** 2854–2859 (2009).
93. Yanik, A. A., Huang, M., Artar, A., Chang, T.-Y. & Altug, H. Integrated nanoplasmonic-nanofluidic biosensors with targeted delivery of analytes. *Appl. Phys. Lett.* **96,** 021101 (2010).
94. Escobedo, C., Brolo, A. G., Gordon, R. & Sinton, D. Flow-Through vs Flow-Over: Analysis of Transport and Binding in Nanohole Array Plasmonic Biosensors. *Anal. Chem.* **82,** 10015–10020 (2010).
95. Huang, M., Yanik, A. A., Chang, T.-Y. & Altug, H. Sub-wavelength nanofluidics in photonic crystal sensors. *Opt. Express* **17,** 24224 (2009).
96. Chow, E., Grot, A., Mirkarimi, L. W., Sigalas, M. & Girolami, G. Ultracompact biochemical sensor built with two-dimensional photonic crystal microcavity. *Opt. Lett.* **29,** 1093 (2004).
97. Lee, M. R. & Fauchet, P. M. Nanoscale microcavity sensor for single particle detection. *Opt. Lett.* **32,** 3284 (2007).
98. Lee, M. R. & Fauchet, P. M. Two-dimensional silicon photonic crystal based biosensing platform for protein detection. *Opt. Express* **15,** 4530 (2007).
99. Nunes, P. S., Mortensen, N. A., Kutter, J. P. & Mogensen, K. B. Photonic crystal resonator integrated in a microfluidic system. *Opt. Lett.* **33,** 1623 (2008).
100. Mandal, S., Goddard, J. M. & Erickson, D. A multiplexed optofluidic biomolecular sensor for low mass detection. *Lab. Chip* **9,** 2924–2932 (2009).

101. Rindorf, L. *et al.* Photonic crystal fiber long-period gratings for biochemical sensing. *Opt. Express* **14,** 8224 (2006).
102. Phan Huy, M. C. *et al.* Three-hole microstructured optical fiber for efficient fiber Bragg grating refractometer. *Opt. Lett.* **32,** 2390 (2007).
103. Rindorf, L. & Bang, O. Highly sensitive refractometer with a photonic-crystal-fiber long-period grating. *Opt. Lett.* **33,** 563 (2008).
104. He, Z., Zhu, Y. & Du, H. Long-period gratings inscribed in air- and water-filled photonic crystal fiber for refractometric sensing of aqueous solution. *Appl. Phys. Lett.* **92,** 044105 (2008).
105. Wu, D. K. C., Kuhlmey, B. T. & Eggleton, B. J. Ultrasensitive photonic crystal fiber refractive index sensor. *Opt. Lett.* **34,** 322 (2009).
106. White, I. M., Oveys, H. & Fan, X. Liquid-core optical ring-resonator sensors. *Opt. Lett.* **31,** 1319 (2006).
107. Barrios, C. A. *et al.* Label-free optical biosensing with slot-waveguides. *Opt. Lett.* **33,** 708 (2008).
108. Bernardi, A. *et al.* On-chip Si/SiOx microtube refractometer. *Appl. Phys. Lett.* **93,** 094106 (2008).
109. Li, H. & Fan, X. Characterization of sensing capability of optofluidic ring resonator biosensors. *Appl. Phys. Lett.* **97,** 011105 (2010).
110. Sumetsky, M., Dulashko, Y. & Windeler, R. S. Optical microbubble resonator. *Opt. Lett.* **35,** 898 (2010).
111. Testa, G., Huang, Y., Sarro, P. M., Zeni, L. & Bernini, R. Integrated silicon optofluidic ring resonator. *Appl. Phys. Lett.* **97,** 131110 (2010).
112. Grillet, C. *et al.* Compact tunable microfluidic interferometer. *Opt. Express* **12,** 5440 (2004).
113. Song, W. Z. *et al.* Determination of single living cell's dry/water mass using optofluidic chip. *Appl. Phys. Lett.* **91,** 223902 (2007).
114. Guo, Y. *et al.* Optofluidic Fabry–Pérot cavity biosensor with integrated flow-through micro-/nanochannels. *Appl. Phys. Lett.* **98,** 041104 (2011).
115. Song, W. Z. *et al.* Refractive index measurement of single living cells using on-chip Fabry-Pérot cavity. *Appl. Phys. Lett.* **89,** 203901 (2006).
116. Shao, H., Wang, W., Lana, S. E. & Lear, K. L. Optofluidic Intracavity Spectroscopy of Canine Lymphoma and Lymphocytes. *IEEE Photonics Technol. Lett.* **20,** 493–495 (2008).
117. St-Gelais, R., Masson, J. & Peter, Y.-A. All-silicon integrated Fabry–Pérot cavity for volume refractive index measurement in microfluidic systems. *Appl. Phys. Lett.* **94,** 243905 (2009).
118. Ouyang, H., Striemer, C. C. & Fauchet, P. M. Quantitative analysis of the sensitivity of porous silicon optical biosensors. *Appl. Phys. Lett.* **88,** 163108 (2006).
119. Orosco, M. M., Pacholski, C. & Sailor, M. J. Real-time monitoring of enzyme activity in a mesoporous silicon double layer. *Nat. Nanotechnol.* **4,** 255–258 (2009).

120. Steele, J. J., van Popta, A. C., Hawkeye, M. M., Sit, J. C. & Brett, M. J. Nanostructured gradient index optical filter for high-speed humidity sensing. *Sens. Actuators B Chem.* **120,** 213–219 (2006).
121. Schubert, M. F., Xi, J.-Q., Kim, J. K. & Schubert, E. F. Distributed Bragg reflector consisting of high- and low-refractive-index thin film layers made of the same material. *Appl. Phys. Lett.* **90,** 141115 (2007).
122. Steele, J. J. & Brett, M. J. Nanostructure engineering in porous columnar thin films: recent advances. *J. Mater. Sci. Mater. Electron.* **18,** 367–379 (2006).

Chapter 2

Liquids Analysis with Optofluidic Bragg Microcavities

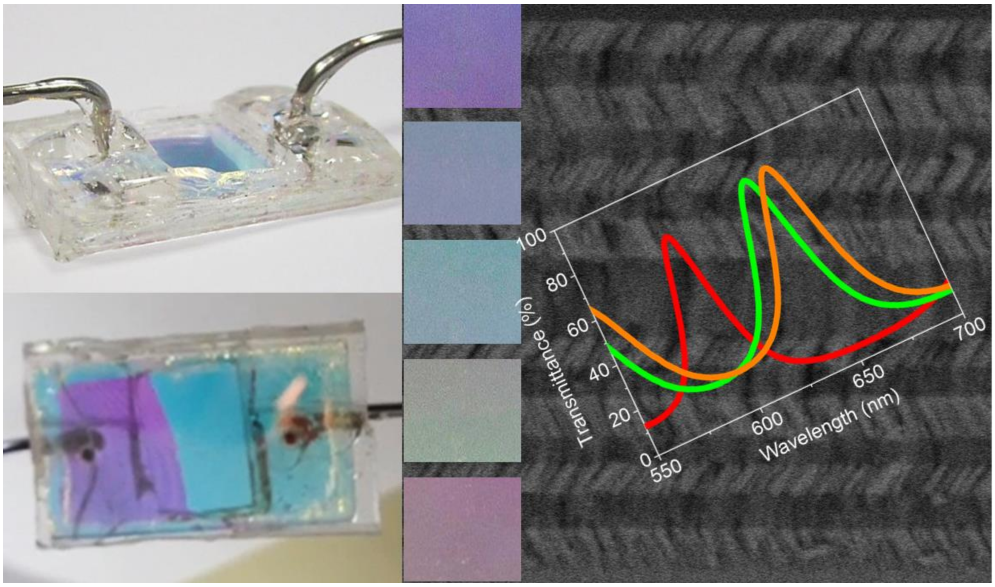

2. 1. Introduction

Responsive systems are devices or materials capable of responding automatically in a predictable and reversible way to an external physical or chemical stimulus from the environment.[1] For chemical analysis, such systems may substitute complex analytical instruments and provide simple and reliable procedures for the detection or even the determination of the concentration of a given analyte in a mixture with other components.[2–4] The physical parameters that can be modified by interaction with the environment can be of different nature and affect the optical, electrical or even magnetic properties of the material or device. A simple example based on changes in optical parameters refers to the variations produced in the refractive index of porous thin films or multilayer structures when they are exposed to vapors of water or other condensable compounds.[5] Similar changes in the optical response are the basis of the emerging field of Optofluidic,[6] where changes in the optical properties of many devices (e.g., wave guides, stacked multilayer or other photonic structures) are reversibly controlled by the incorporation of liquids. Optical lattices with controlled and accessible porosity has been utilized for chemical responsive applications with systems made by the stacking of metal oxide nanoparticles,[7,8] mesostructured thin films,[9,10] clays,[11] macroporous alumina[12] or porous silicon layers.[5,13,14] In this line, our research group have recently shown that multilayer structures prepared by physical vapor deposition in the form of one-dimensional photonic crystals (1DPC) may experience a large change in the position of their wide transmission gap when they are infiltrated with liquids.[15] A similar effect has been recently proposed for the identification of solvents by using 1DPC formed by the stacking of polymer layers and titania nanoparticles.[16] A 1DPC, also known as Bragg stack or Bragg reflecting mirror, is a simple photonic structure made by the stacking of successive and alternating layers of two transparent materials with different refractive index.

Due to optical interference processes, these photonic structures produce a reflection of light that extends over a certain range (Bragg gap) of wavelengths producing the impression of a colored mirror. The position and width of the reflecting gap can be tuned by controlling the number of stacking layers, their thickness and the difference in the refractive index of the two materials.

Planar Bragg microcavities, a modification of 1DPCs, integrate in the center of a Bragg reflector a layer with a different thickness. The incorporation of this layer, considered as an optical defect, gives rise to the appearance of a resonance narrow peak in the Bragg gap. Planar Bragg microcavities made of porous silicon prepared by electrochemical methods have been proposed for sensing vapours[5,13,14] or for the development of advanced biosensing tests.[17–19] The integration of a non-planar Bragg microcavity fabricated by electron-beam lithography and reactive ion etching techniques into a microfluidic device for optofluidic applications has been reported recently.[20]

In the present chapter we report the fabrication of planar Bragg microcavities by stacking successive layers of two transparent and porous oxides prepared by e-beam evaporation in a glancing angle configuration (GLAD).[15] This geometrical configuration renders films formed by tilted nanocolumns with a considerable amount of void space in the form of meso- and micro-pores (i.e., pores larger or smaller than 2nm according to the IUPAC,[21]). A full account of the pores and other characteristics of this type of thin films can be found in recent publications.[22–24] GLAD thin films have been also deposited to modify the channel walls of microfluidic devices to facilitate the circulation of liquids[25] or to provide high surface area substrates to increase the anchoring capacity of active molecules used for molecular recognition.[26] However, no essays have been reported about the direct use of GLAD thin film structures as microfluidic components, a fact that is likely related to the difficulty of accurately controlling the porosity and optical properties of both the individual GLAD thin films and the collective response of the final microcavities. A first objective of the present work is to prove that the optical properties of porous GLAD microcavities can be accurately controlled without incurring in light dispersion effects very common when dealing with other type of porous materials. Subsequently, we show that these porous structures can be integrated in the form of planar microfluidic components through which liquids can circulate easily. Using this configuration we show that planar Bragg microcavities, made by stacking several porous TiO_2 and SiO_2 GLAD thin films, can be used as efficient optofluidic responsive systems for measuring the solute concentrations of liquid solutions or for the analysis of liquid mixtures. Case examples of the response of these devices and the modeling of their optical response by using a conventional interference optical model[27] complete the present chapter.

2. 2. Experimental and Methods

Uniform, mechanically stable and highly porous Bragg microcavity structures made of alternated layers of TiO_2 and SiO_2 with a thicker SiO_2 central layer have been prepared by glancing angle physical vapour deposition (GLAD). Porous layers were successively e-beam evaporated on glass plates of 1.2 x 2.5 cm^2 at glancing zenithal angles of 70^0 and 80^0 (α). SiO_2 and TiO_2 were used as target materials while an oxygen pressure of approximately 10^{-4} torr was kept in the chamber during the evaporation to ensure the complete oxidation of the evaporated oxides (i.e. to get TiO_2 and SiO_2 stoichiometries) and hence their full transparency (TiO_x or SiO_x with $x<2$ are colored). The GLAD geometry produces films with a characteristic tilted columnar morphology which is controlled by shadowing effects.[22] The results reported here refer to structures consisting of 2x7 individual layers of approximately 85 nm thickness, plus one SiO_2 middle layer of approximately 180 nm thickness. The thickness of each individual layer was controlled by means of a quartz crystal monitor calibrated with the actual thickness of layers determined by cross section SEM.

Preparations were carried out by azimuthally turning the substrate 90^0 when changing the evaporation from one oxide to the other. Turning azimuthally the substrate between two layers is required to avoid the dispersion of light, an effect that has been previously addressed in a work on porous 1DPC used to prepare dye sensitized solar cells.[28]

The stacked layers deposited on a glass plate were sandwiched with another glass plate provided with two holes where liquid tubes acting as inlet/outlet channels of the fluids were fixed. The perimeter of the ensemble was sealed with PDMS to ensure the tightness of the system. A scheme of the system is presented in **Figure 2.1**, together with a view of a real device fabricated in the course of this work. In this device, the space between the two glass plates is completely filled with the microcavity structure and the fluids flow by passing through the pores of the films by just applying a small pressure difference between the inlet and outlet tubes. It could be also realized that liquids with low viscosity and surface tension can pass spontaneously driven by capillarity forces. This configuration ensures that pores are completely filled with the liquid and that an easy and immediate replacement of one liquid by another is possible by just changing an external reservoir connected to the device. Another important clue, proved by simulating[27] the optical response of the system, was that no empty space is left between the stacked microcavity and the glass cover plate.

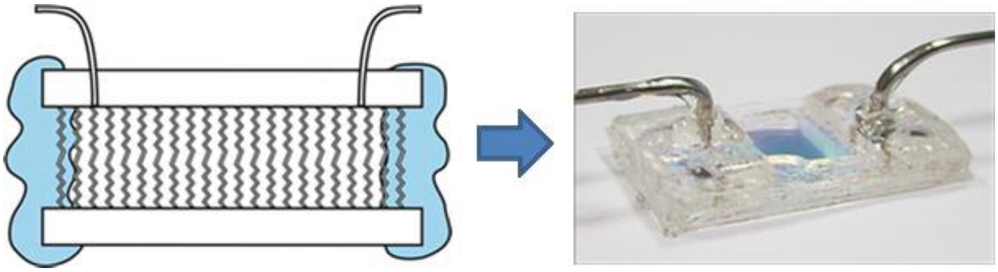

Figure 2.1. (left) Cross section scheme and (right) image of a microfluidic device based on a Bragg microcavity prepared by GLAD. Note that the different parts in the scheme are not plotted at the same scale.

Cross section SEM micrographs were obtained in a Hitachi S4800 field emission microscope for samples deposited on a silicon wafer that were cleaved for cross section analysis.

UV-vis transmission spectra were recorded in normal and off-normal configurations with a Cary 100 instrument. For recording at off-normal angles, the microfluidic device was turned with respect to the light beam by using a goniometer provided with a holding piece.

Simulation of the optical response of the Bragg microcavity was done by optimized fitting of the transmittance spectra using a home-made code based on the transfer-matrix approach. Typical Cauchy dispersion was considered for the refractive index. The refractive index and the thicknesses of the SiO_2 and TiO_2 layers in the two 7-layers Bragg reflectors and the SiO_2 defect layer were obtained through the fitting procedure.

2. 3. Results and Discussion

2. 3. 1. Microstructure and optical properties of Bragg microcavities prepared by GLAD

Figure 2.2 shows cross section SEM micrographs of a GLAD porous Bragg microcavity integrated by two Bragg reflectors made of 7 stacked layers of SiO_2 and TiO_2 sandwiching a thicker SiO_2 layer as indicated by the diagram of the figure. The thickness of the SiO_2 and TiO_2 stacked layers was about 85 nm, while that of the SiO_2 defect was around 180 nm. An accurate control of the optical properties of the microcavity was possible by changing these thickness dimensions. The whole structure was prepared by GLAD at a fixed zenithal angles of $\alpha=70^0$ and $\alpha=80^0$ by turning the substrate 90^0 from one layer to the next. This azimuthal rotation was essential to decrease the dispersion of light at low wavelengths, a common phenomenon found for relatively thick GLAD oxide films.

It is worth stressing that compared with conventional silicon porous Bragg microcavities prepared by controlled electrochemical oxidation followed by annealing at high temperature,[5,13,14,17–19] the GLAD methodology is advantageous because it is compatible with any sensitive substrate (e.g. polymers) and does not require any oxidation step at high temperatures to make the stacked layers transparent. Moreover, the large contrast between the refractive index of the individual SiO_2 and TiO_2 layers of the GLAD microcavities (SiO_2 and TiO_2 GLAD layers have refractive indices of 1.22/1.20 and 1.70/1.55 when prepared at 70^0 and 80^0, respectively[22,23]) and their high pore volume (i.e., approximately 49% and 60% for these two evaporation angles[22,23]) make these optical devices suitable for a wide range of optofluidic applications.

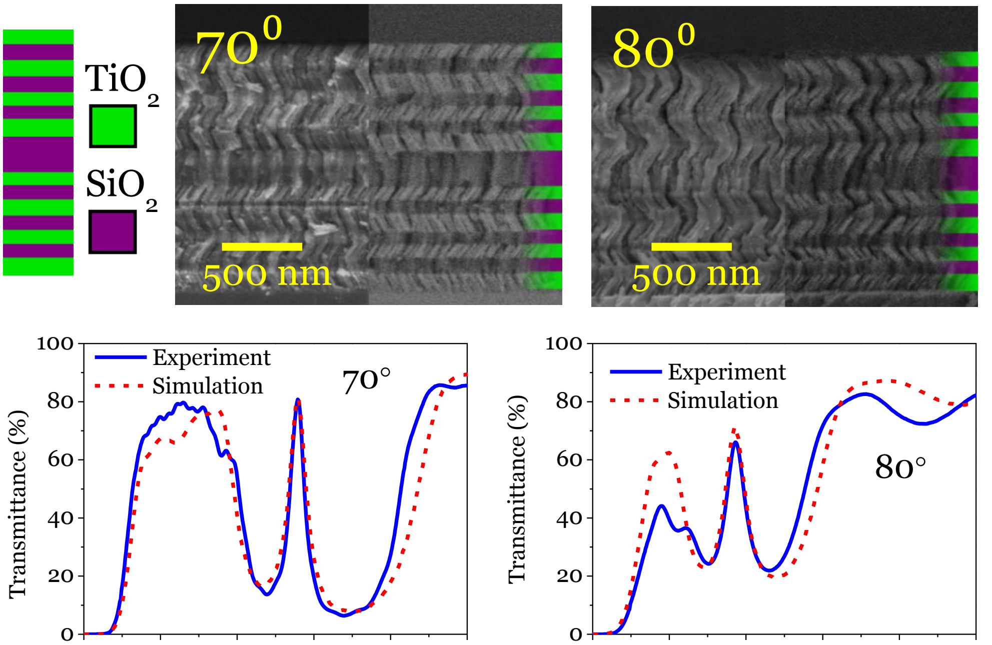

Figure 2.2. (Top) cross section SEM micrograph (bright and dark fields) of a cleaved microcavity prepared by evaporation at 70^0 and 80^0 of zenithal angle. The scheme shows the stacking order of the individual layers forming the microcavity. (Bottom) UV-vis transmission spectra of microcavities prepared at 70^0 (left) and 80^0 (right) zenithal angles. Simulated spectra are plotted for comparison.

The optical behavior of the microcavity structure was checked by UV-vis transmission spectroscopy. **Figure 2.2** (bottom) shows the measured and simulated transmission spectra obtained for microcavities prepared at 70^0 and 80^0 of zenithal angle of evaporation. These spectra depict the typical behavior of planar optical microcavities which, for the 70^0 case, consists of a wide reflecting region extending from approximately 500 to 700 nm, and a narrow and sharp resonant peak located at 579 nm and a width at half height of 18.5 nm (i.e. a Q factor, defined as the ratio of the resonance cavity frequency to the line width of the cavity mode, of 31). For the 80^0 microcavity, these spectral parameters are 486, and 23.7 nm (Q factor 20), respectively. In this latter case the position and other spectral features of the transmission spectra are well reproduced for λ>450 nm, but deviations are observed below this wavelength value. We attribute the decrease in the transmitted light in this spectral region, enhanced at high zenithal angles, to light dispersion effects at the void and oxide material nanostructures formed in these films.[5,28]

For the individual layers, Table 2.1 summarizes the thickness values determined experimentally by SEM and those estimated by the simulation of the spectral features. The refractive index values of SiO_2 and TiO_2 required to get a good fitting are also included in this table. Within a variation of 10%, limit of accuracy estimated for the simulations, the calculated refractive indices are similar to the experimental values of **n** previously determined for GLAD thin films of these materials.[22,23] In comparison with the **n** values of compact films of these two oxides (i.e., around 1.45 and 2.40 for SiO_2 and TiO_2, respectively[29]), the low value of this parameter obtained for the GLAD thin films confirms their high porosity and, hence, the possibility of modifying **n** if the pores are filled with liquids. The porosity values of the individual layers of the Bragg microcavity determined by simulation are reported in Table 1.

Table 2.1. Characteristic layer parameters of Bragg microcavities prepared at α=70° and 80°.

Zenithal angle/layer	**Thickness** *(exp)* **(nm)**	**Thickness** *(sim)* **(nm)**	**n** *(sim)*	**n with water** *(sim)*	**Porosity (%)** *(sim)*
70° TiO_2	94	88	1.69	1.83	49
70° SiO_2	88	81	1.23	1.39	49
70° SiO_2 defect	224	178	1.21	1.39	52
80° TiO_2	82	88	1.55	1.72	60
80° SiO_2	80	86	1.20	1.38	55
80° SiO_2 defect	168	180	1.20	1.38	55

Thickness and refractive index values are derived from the SEM measurements (exp) and by simulation of the transmission spectra (sim). Data are provided for the "as prepared" microcavities and for the microcavities integrated in a microfluidic device with water circulating through them.

2. 3. 2. Optofluidic response of microcavities

To check whether the optical response of the GLAD microcavities changes when their pores are filled with a fluid, we flowed a series of liquids of different refractive indices through a microfluidic device integrating the Bragg porous structure. **Figure 2.3** shows the experimental and simulated UV-vis transmission spectra obtained for an empty 70° microcavity and after circulating through it liquids of different refractive indices (i.e., water (**n**=1.330), ethanol (**n**=1.361), toluene (**n**=1.496) and chlorobenzene (**n**=1.525)). An observed effect is a shift to longer wavelengths of both the transmission gap and of the resonant peak. The magnitude of the shifts depends on the refractive index of the liquid and can be simulated by varying the effective refractive indices of each individual layer attached in the microcavity. The values obtained for the case of water are gathered in **Table 2.1**, while the values deduced for the other liquids are reported in the **Table 2.2**. The calculated refractive indices are higher than those of the empty (actually air-filled) layers as expected for a medium consisting of a liquid filling the pores and voids of the individual films microstructure.

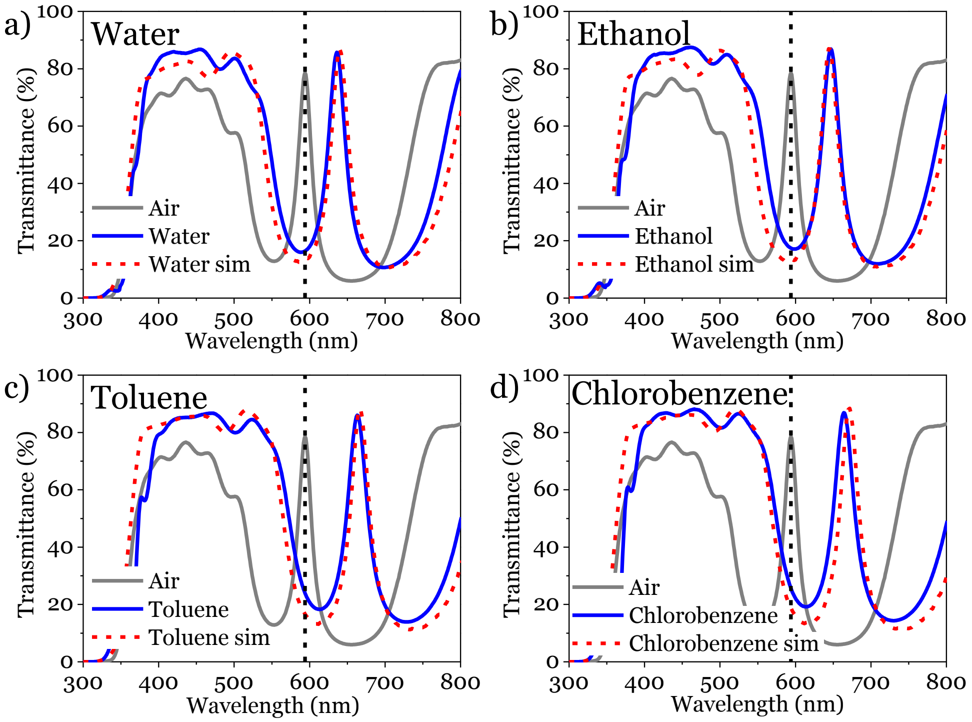

Figure 2.3. Experimental (full lines) and simulated (dashed lines) UV-vis transmission spectra of a microcavity device prepared at 70^0 before (black line) and after (gray lines) circulating different liquids through it: a), water; b), ethanol; c), toluene; d) Chlorobenzene. The vertical lines indicate the position of the resonant peak in the microcavity without any liquid (i.e., with the pores filled with air).

Table 2.2. Simulated layer refractive indices of Bragg microcavities prepared at α=70^o and 80^o.

Zenithal angle/layer	**n *(sim)* with water**	**n *(sim)* with ethanol**	**n *(sim)* with toluene**	**n *(sim)* with cl-benzene**
70^o TiO_2	1.830	1.843	1.906	1.920
70^o SiO_2	1.392	1.406	1.472	1.487
70^o SiO_2 defect	1.389	1.404	1.474	1.489
80^o TiO_2	1.724	1.741	1.818	1.835

80^o SiO$_2$	1.384	1.401	1.475	1.491
80^o SiO$_2$ defect	1.384	1.401	1.475	1.491

Refractive index values of the individual layers estimated by simulation of the spectra obtained when 70^0 and 80^0 microcavities were infiltrated with liquids of different refractive indices.

Figure 2.4 displays a similar behavior for the microcavities prepared at 80^0, with the additional effect that the transmission at low wavelengths recovered the level predicted by the theoretical simulation. This effect is attributed to the removal of light scattering effects by the liquids infiltrated through the otherwise empty micro- and meso-pores.

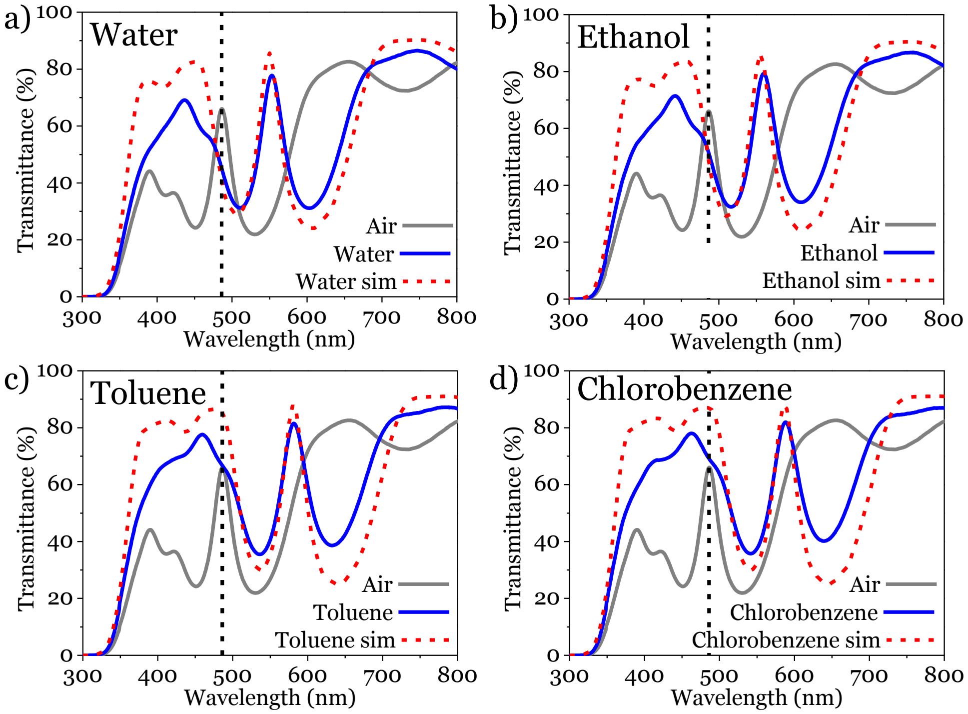

Figure 2.4. Experimental (full lines) and simulated (dashed lines) UV-vis transmission spectra of a microcavity device prepared at 80º before (black line) and after (gray lines) being circulated with different liquids. The vertical lines indicate the position of the resonant peak in the microcavity without any liquid (i.e., with the pores filled with air).

The overall optical changes induced by circulating liquids through the microcavity devices were so apparent that they could be observed with the bare eyes (c.f. **Figure 2.5** (left), thus opening the possibility of using them as visual tags.

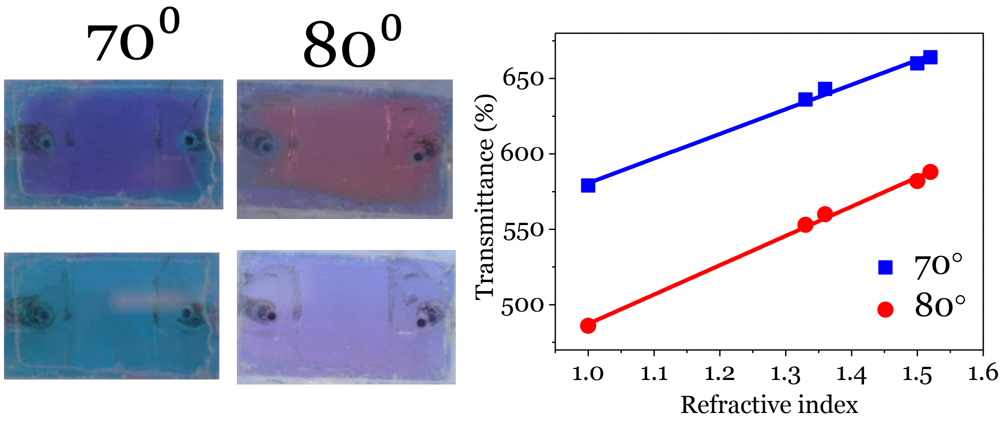

Figure 2.5. (left) Images of 70^0 and 80^0 microfluidic devices empty (top) and filled with toluene (bottom). (right) Plot of the position of the resonant peak in the UV-vis spectra of the 70^0 and 80^0 microcavity devices as a function of the refractive index of the infiltrated liquid.

From an analytical point of view it is quite significant that the shift in the position of the resonant peak observed in **Figures 2.3** and **2.4** can be directly related to the refractive index of the infiltrated liquid as reported in **Figure 2.5** (right). This plot shows that the position of the maximum of the resonant peak varies almost linearly with the refractive index of the infiltrated liquid and supports that this kind of microfluidic device can be used to identify liquids of different refractive indices. A similar approach has been used to detect vapors of organic solvents by means of Bragg microcavities made of porous silicon layers of different porosities.[5,15,16]

A well-known behavior of compact Bragg microcavities is an angular dispersion in the position of the resonance peak when varying the incident angle of light.[27] As reported in **Figure 2.6**, porous microcavities behave in the same way either empty or filled with a liquid. This figure clearly shows that the resonant peak position shifts to shorter wavelengths when tilting the device with respect to the direction of light. Within the angular variation monitored in this experiment, the resonance peak of the 70^0 microcavity kept a similar height and width irrespective of the incident angle of light.

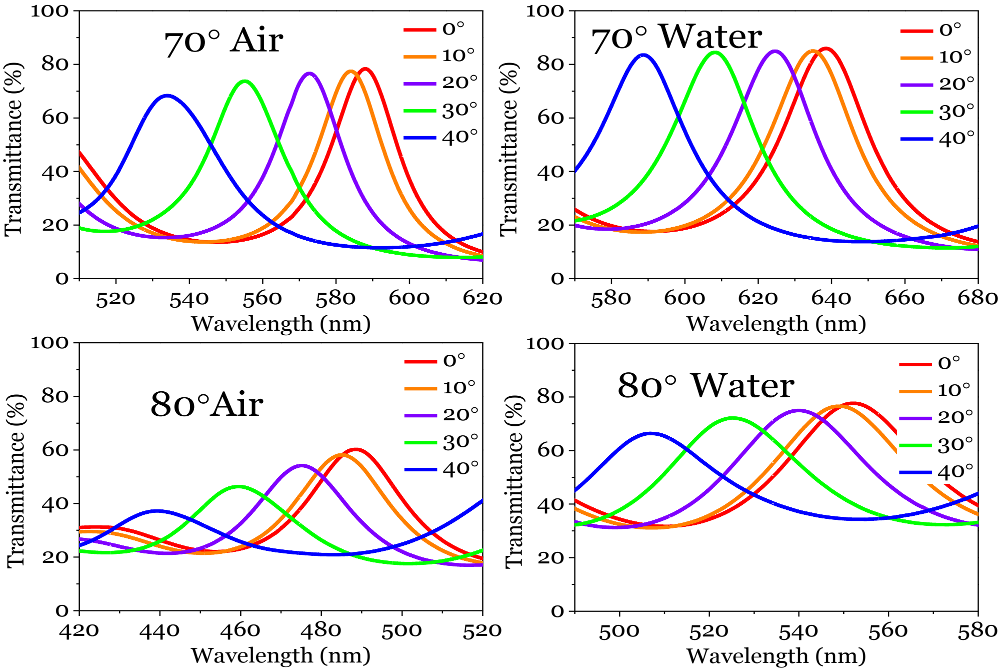

Figure 2.6. UV-vis transmission spectra for the indicated incident angles of light for empty (left) and water infiltrated (right) 70^0 (top) and 80^0 (bottom) microcavity structures.

Similar angular variations were found for the porous microcavities filled with liquids (c.f., **Figure 2.6** (right)), although the magnitude of the shift depended on the refraction index of the liquid. For example, turning by 40^0 the 70^0 microcavity, resulted in a shift of 53 nm for the empty device and 48 and 54nm for the system filled with water or chlorobenzene, respectively. Similar effects could be appreciated for the microcavities prepared at 80^0.

2. 3. 3. Optofluidic analysis of liquid solutions by means of GLAD microcavities

The previous sections have dealt with the change in the optical response of porous microcavities when they are infiltrated with pure liquids. Due to the large difference in the refractive index of the porous TiO_2 and SiO_2 constituent layers, the microcavity device structures were very sensitive to small differences in the refractive index of the infiltrated liquids. Taking advantage of this enhanced sensitivity we propose to use these microcavities to determine the concentration of liquid solutions or the proportion of two liquids in a mixture. Some proofs of concept will be reported here to ascertain the feasibility of this analytical approach.

Figure 2.7 shows a series of UV-vis spectra in the region of the resonance peak for a 70^0 microcavity circulated with NaCl and glucose solutions with concentrations ranging from 0.5 to 4 mol/L and 0.5 to 3 mol/L, respectively. The spectra show that the peak position steadily varies with the solution concentration, a dependence that must be attributed to the different refractive index of the solutions.[30] Moreover, a representation of the peak position versus the solution concentrations yields in the two cases a practically linear dependence. These lines can be taken as calibration curves of glucose and NaCl concentrations for this particular device.

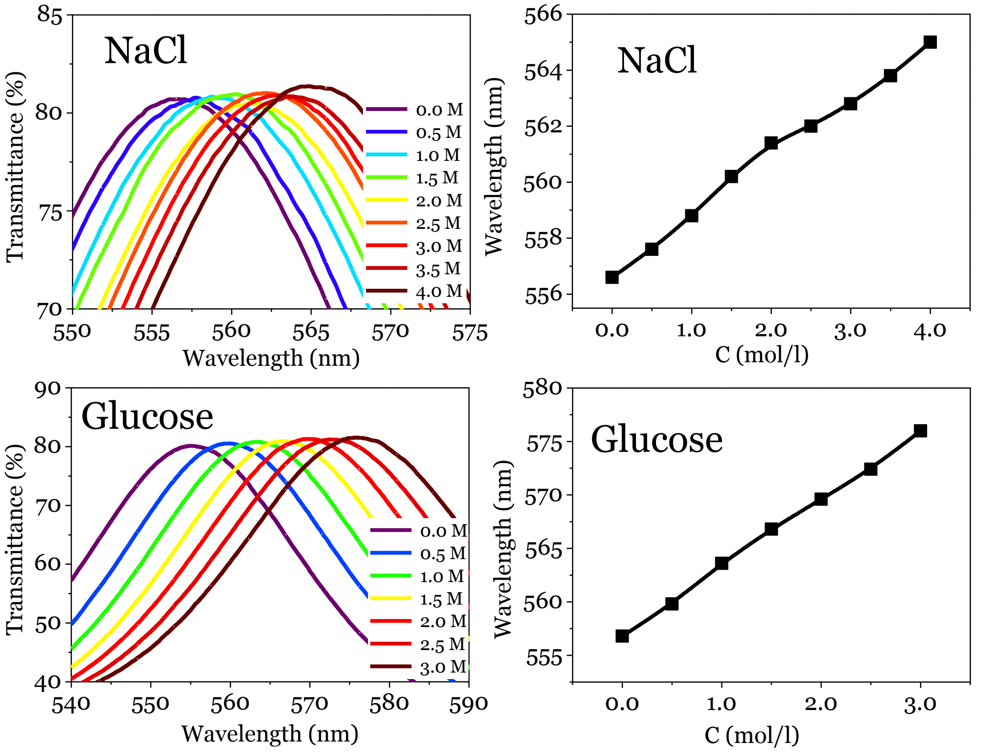

Figure 2.7. (left) UV-vis transmission spectra for a 70^0 microcavity infiltrated with water and a series NaCl (a) and glucose (c) solutions of the indicated concentrations. Right) Plots of the shift in the position of the resonance peak as a function of NaCl (b) and glucose (d) concentrations. Note the different scales used for each plot.

Monitoring the peak position requires a wavelength sensitive detector. Since intensity detectors are simpler, cheaper and easier to operate, we explored an alternative way of measuring the solute concentration by looking to the angular variation of the peak position (cf. **Figures 2.7** and **2.10**) as a function of the solute concentration. The principle of the measuring procedure is reported in **Figure 2.8**, illustrated for the case of 70^0 Bragg microcavity, empty and filled with water. For a 0^0 incident angle of light, the resonance peak shifts to longer wavelengths when the device is infiltrated with water. This shift can be counterbalanced by turning the microfluidic device by an angle of 49^0 with respect to the light beam direction. For practical purposes, measurements of solution concentrations would be possible by using a single wavelength source (e.g. a LED) tuned to the resonance maximum of the microcavity, either empty or filled with water, an intensity detector and a goniometer to measure the angular shift required to recover the maximum intensity of the transmitted light.

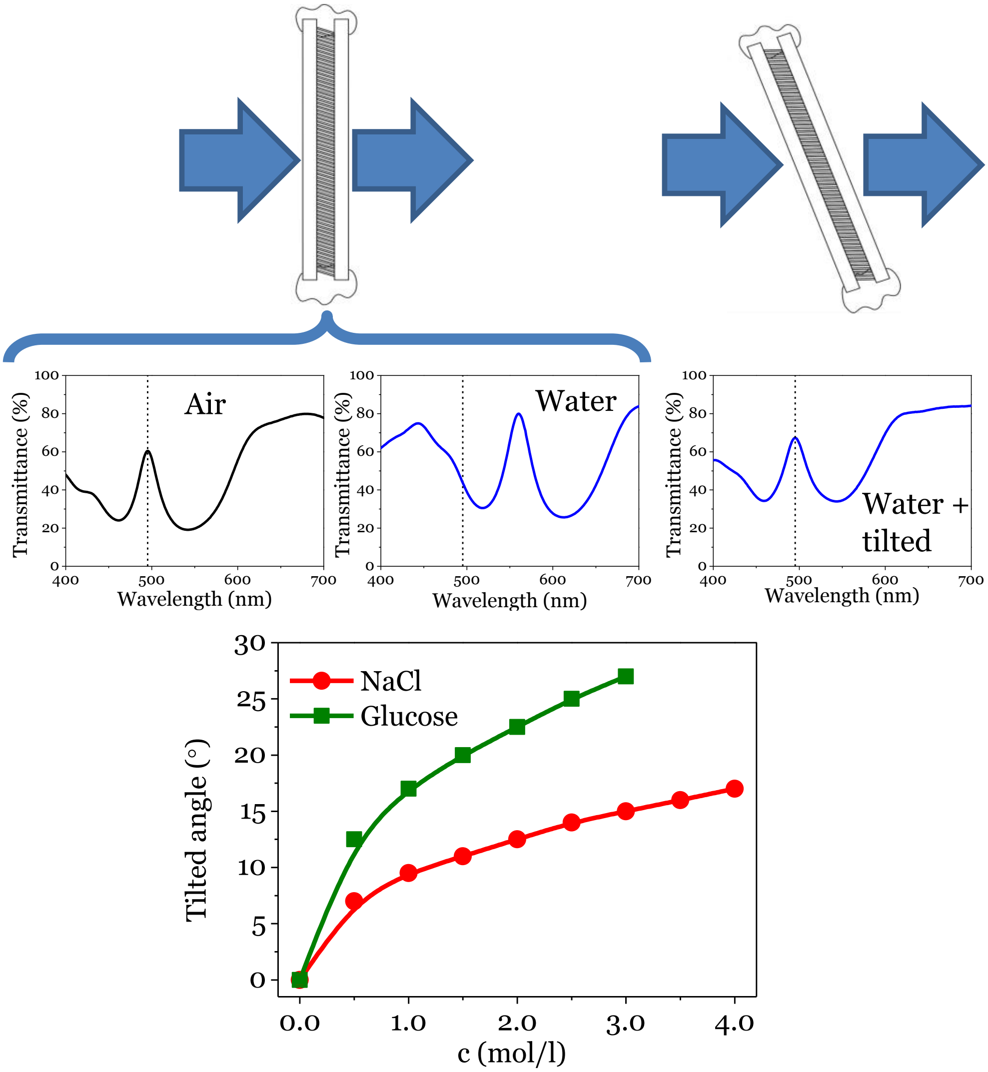

Figure 2.8. (Top) Scheme showing the variation of the position of the resonant peak when a microcavity is filled with water and the recovery of the initial wavelength position when the device is turned by a given angle. (Bottom) Correlation between the tilted angles of the microcavity and the concentration of the NaCl and glucose solutions according to the procedure described in the scheme.

For the investigated NaCl and glucose solutions, **Figure 2.8** shows the angular variations obtained as a function of the solution concentrations. Although the dependence is not linear, the depicted profiles follow well-defined calibration curves that can be used to determine the concentration of unknown solutions of these two substances.

Mixtures of liquids with different refractive indices can be also monitored by using GLAD microcavity devices, provided that they present sufficiently large differences of refractive indices. **Figure 2.9** shows the results obtained for mixtures of glycerol (**n**=1.473) and water (**n** =1.330). The spectra and the plot in this figure are referred to the volume percentage of glycerol. It is apparent in this figure that the resonant peak shifts with the percentage of glycerol and that this shift follows well defined dependences, both when representing the wavelength of the maximum of the resonant peak or the angle turned to recover its maximum intensity. These results clearly prove that a microfluidic device consisting of a porous microcavity prepared by GLAD can be used to determine the proportion of two liquids in a mixture, provided that their refractive indices differ sufficiently.

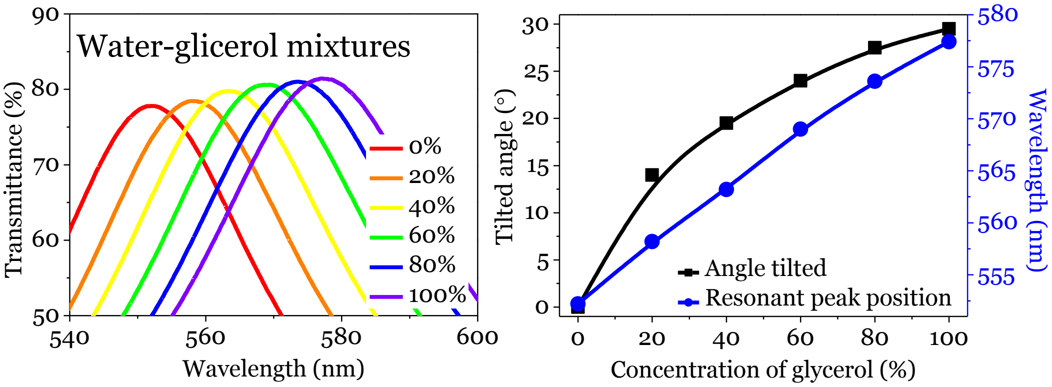

Figure 2.9. (left) UV-vis transmission spectra for a 70^0 microcavity infiltrated with mixtures of glycerol and water with different proportions of the two liquids. (Right) Plot of the shift in the position of the resonance peak and angle turned to restore its maximum intensity as a function of percentage of glycerol in the mixture.

Besides these simple applications, we anticipate that this type of devices will be useful for the continuous monitoring of liquids in microfluidic[31] or other analytical applications involving minutes amounts of liquids (the pore volume of a microcavity device can be estimated in ~$7.5x10^{-3}$ mm^3) or as cheap disposable systems for food control. As practical cases of this latter application field, **Figure 2.10** of the supporting information report two examples showing how the developed microcavities can identify common beverages (different types of colas, isotonic drinks, etc.) or vegetable oils (e.g., olive or sunflower oils). Even if the viscosity of oils is rather high, its management through the microcavity structures is quite straightforward, what opens the way to the practical implementation of these devices for the analysis of a large variety of liquids.

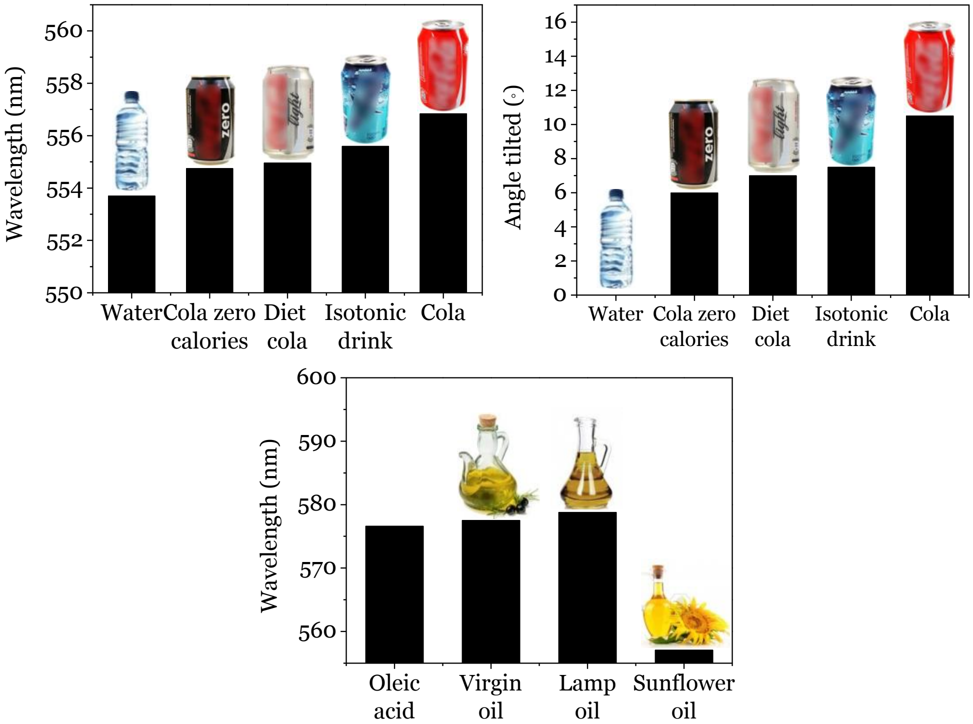

Figure 2.10. Analysis with a 70^0 GLAD microcavity device. (Top) results of the analysis of a series of everyday drinks: (left) position of the resonant peak; (right) angle turned to restore the position of the resonant peak. (Bottom) Position of the resonant peak for a series of food oils.

2. 4. Conclusions

In this work we have shown the electron-beam fabrication of GLAD planar porous microcavities consisting of successive layers of two oxides (SiO_2 and TiO_2) of different refractive indices. A strategy consisting of azimuthally turning the substrate from one layer to the next has been developed to minimize the light scattering effects usually observed for thick porous layers made by GLAD or other techniques. These microcavities have resulted very useful to determine the refractive index of liquids and solutions. The high transparency of the individual constituent layers and their high porosity has enabled their integration in the form of a microfluidic device where liquids fill and circulate through the void space of these structures. The simulation analysis of the changes observed in the transmission spectra of the microcavities after infiltration has proved that the position of the resonance peak depends on the refractive index of the liquid. This feature has been used systematically to determine the characteristics of the liquids by both measuring the position of the maximum or by turning the photonic structure by a certain angle to restore the maximum intensity of the resonance peak at its initial wavelength. These two methods of detection have been successfully applied to determine the concentration of different solutions and mixtures of liquids.

The low volume of liquid required to induce these changes makes easy the implementation of the developed technology into complex microfluidic systems where it could provide a simple and reliable method of analysis. In addition, it could be also employed to develop switchable optofluidic components for switchable photonic applications.

2. 5. References

1. Ge, J. & Yin, Y. Responsive Photonic Crystals. *Angew. Chem. Int. Ed.* **50,** 1492–1522 (2011).
2. Holtz, J. H. & Asher, S. A. Polymerized colloidal crystal hydrogel films as intelligent chemical sensing materials. *Nature* **389,** 829–832 (1997).
3. Lee, Y.-J. & Braun, P. v. Tunable Inverse Opal Hydrogel pH Sensors. *Adv. Mater.* **15,** 563–566 (2003).
4. Sharma, A. C. *et al.* A General Photonic Crystal Sensing Motif: Creatinine in Bodily Fluids. *J. Am. Chem. Soc.* **126,** 2971–2977 (2004).
5. Stefano, L. D., Rendina, I., Moretti, L. & Rossi, A. M. Optical sensing of flammable substances using porous silicon microcavities. *Mater. Sci. Eng. B* **100,** 271–274 (2003).
6. Fan, X. & White, I. M. Optofluidic microsystems for chemical and biological analysis. *Nat. Photonics* **5,** 591–597 (2011).
7. Wu, Z., Lee, D., Rubner, M. F. & Cohen, R. E. Structural Color in Porous, Superhydrophilic, and Self-Cleaning SiO2/TiO2 Bragg Stacks. *Small* **3,** 1445–1451 (2007).
8. Colodrero, S., Ocaña, M., González-Elipe, A. R. & Míguez, H. Response of Nanoparticle-Based One-Dimensional Photonic Crystals to Ambient Vapor Pressure. *Langmuir* **24,** 9135–9139 (2008).
9. Choi, S. Y., Mamak, M., von Freymann, G., Chopra, N. & Ozin, G. A. Mesoporous Bragg Stack Color Tunable Sensors. *Nano Lett.* **6,** 2456–2461 (2006).

10. Fuertes, M. C. *et al.* Photonic Crystals from Ordered Mesoporous Thin-Film Functional Building Blocks. *Adv. Funct. Mater.* **17,** 1247–1254 (2007).
11. Lotsch, B. V. & Ozin, G. A. Photonic Clays: A New Family of Functional 1D Photonic Crystals. *ACS Nano* **2,** 2065–2074 (2008).
12. Guo, D.-L., Fan, L.-X., Wang, F.-H., Huang, S.-Y. & Zou, X.-W. Porous Anodic Aluminum Oxide Bragg Stacks as Chemical Sensors. *J. Phys. Chem. C* **112,** 17952–17956 (2008).
13. Huanca, D. R., Ramirez-Fernandez, F. J. & Salcedo, W. J. Porous silicon optical cavity structure applied to high sensitivity organic solvent sensor. *Microelectron. J.* **39,** 499–506 (2008).
14. Torres-Costa, V., Agulló-Rueda, F., Martín-Palma, R. J. & Martínez-Duart, J. M. Porous silicon optical devices for sensing applications. *Opt. Mater.* **27,** 1084–1087 (2005).
15. González-García, L., Lozano, G., Barranco, A., Míguez, H. & González-Elipe, A. R. TiO2–SiO2 one-dimensional photonic crystals of controlled porosity by glancing angle physical vapour deposition. *J. Mater. Chem.* **20,** 6408–6412 (2010).
16. Wang, Z. *et al.* Colorful detection of organic solvents based on responsive organic/inorganic hybrid one-dimensional photonic crystals. *J. Mater. Chem.* **21,** 1264–1270 (2011).
17. Chan, S., Li, Y., Rothberg, L. J., Miller, B. L. & Fauchet, P. M. Nanoscale silicon microcavities for biosensing. *Mater. Sci. Eng. C* **15,** 277–282 (2001).
18. Palestino, G., Legros, R., Agarwal, V., Pérez, E. & Gergely, C. Functionalization of nanostructured porous silicon microcavities for glucose oxidase detection. *Sens. Actuators B Chem.* **135,** 27–34 (2008).
19. Lv, X. *et al.* Novel multilayered porous silicon-based immunosensor for determining Hydroxysafflor yellow A. *Appl. Surf. Sci.* **257,** 1906–1910 (2011).
20. Jugessur, A. S., Dou, J. & Aitchison, J. S. Tunable optofluidic nano-Bragg microcavity filter. *J. Vac. Sci. Technol. B* **28,** C6O8–C6O10 (2010).
21. Haul, R. S. J. Gregg, K. S. W. Sing: Adsorption, Surface Area and Porosity. 2. Auflage, Academic Press, London 1982. 303 Seiten, Preis: $ 49.50. *Berichte Bunsenges. Für Phys. Chem.* **86,** 957–957 (1982).
22. Lola González-García, J. P.-B. Correlation lengths, porosity and water adsorption in TiO_2 thin films prepared by glancing angle deposition. *Nanotechnology* **23,** 205701 (2012).

23. Gonzalez-García, L. *et al.* Tuning Dichroic Plasmon Resonance Modes of Gold Nanoparticles in Optical Thin Films. *Adv. Funct. Mater.* **23,** 1655–1663 (2013).
24. Brett, M. J. & Hawkeye, M. M. New Materials at a Glance. *Science* **319,** 1192–1193 (2008).
25. Harris, K. D., Brett, M. J., Smy, T. J. & Backhouse, C. Microchannel Surface Area Enhancement Using Porous Thin Films. *J. Electrochem. Soc.* **147,** 2002–2006 (2000).
26. Bezuidenhout, L. W., Nazemifard, N., Jemere, A. B., Harrison, D. J. & Brett, M. J. Microchannels filled with diverse micro- and nanostructures fabricated by glancing angle deposition. *Lab. Chip* **11,** 1671–1678 (2011).
27. Handbook of Optics, Volume I - Fundamentals, Techniques, and Design - Handbook of optics second edition Vol 1 - - Bass M.pdf. at <http://iate.oac.uncor.edu/~manuel/libros/Optics/Handbook%20of%20optics%20second%20edition%20Vol%201%20-%20%20-%20Bass%20M.pdf>
28. González-García, L., González-Valls, I., Lira-Cantu, M., Barranco, A. & González-Elipe, A. R. Aligned TiO2 nanocolumnar layers prepared by PVD-GLAD for transparent dye sensitized solar cells. *Energy Environ. Sci.* **4,** 3426–3435 (2011).
29. CRC handbook of chemistry and physics 90th edition. (21:30:13 UTC). at <http://www.slideshare.net/CarlosM131195/crc-handbook-of-chemistry-and-physics-90th-edition-32892073>
30. Yunus, W. M. bin M. & Rahman, A. bin A. Refractive index of solutions at high concentrations. *Appl. Opt.* **27,** 3341 (1988).
31. Kuswandi, B., Nuriman, Huskens, J. & Verboom, W. Optical sensing systems for microfluidic devices: A review. *Anal. Chim. Acta* **601,** 141–155 (2007).

Chapter 3

Optofluidic Modulation of Self-associated Nanostructural Units Forming Planar Bragg Microcavities

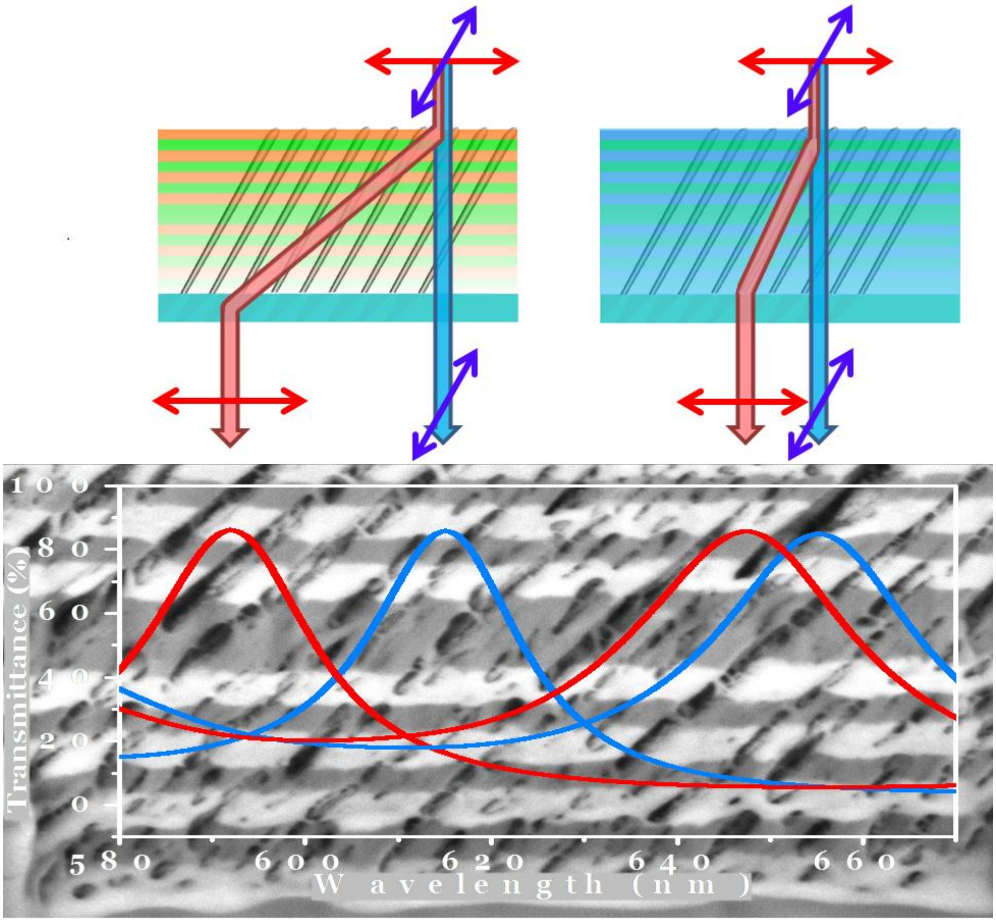

3.1. Introduction

The last innovations in the field of optofluidics have led to the development of highly versatile optical systems with a wide range of applications both at the micro and macroscales and a high impact in fields such as energy[1], photonics[2], microfluidics[3] or sensors and biosensors[4]. Outstanding examples relying on the light control by means of liquids flowing through devices include adaptive and tuneable microlenses[5,6], optofluidic dye laser[7] or advanced optofluidic microscopes[8]. Light polarization by liquids containing chiral molecules or by anisotropic solids is a classical optical principle widely used in advanced technologies for chemical analysis, communications, displays and photonics that, except for very recent works using complex polymer particles[9], has not been addressed within optofluidic schemes aiming at merging optics and microfluidics in a device[3]. In the present work we report that light polarization can be effectively controlled by liquid circulation through a new type of polarization active planar Bragg microcavities (BM) devices prepared by physical vapour oblique angle deposition (PV-OAD). This liquid-mediated control of the activity of planar BMs constitutes a first case of polarizer thin films optofluidics with high impact prospects for the fabrication of polarization active systems, wavelength retarders, photonic sensors or liquid monitoring devices.

Thin films fabrication by PV-OAD, also known as Glancing Angle Deposition (GLAD)[10,11], is a straightforward procedure to tailor film porosities while achieving a strict control over optical properties such as refraction index[12,13] or optical anisotropy and birefringence[14,15]. In the called “sculptured thin films”[16,17], a class of nanostructured GLAD materials, their singular topography, geometry and in-depth architecture permits an effective control of their refractive index and birefringence and the development of optically active photonic structures[18–23] or helicoidally bi-anisotropic media acting for example as narrow band pass optical filters[24], selective circularly polarized light transmitters[25] or selective linearly polarized transmitters[26]. On the other hand, although polarization inactive SiO_2-TiO_2 one dimensional photonic crystals (1DPC)[27,28] and Bragg microcavities (BM)[29] have been also prepared by PVD-OAD, no polarization activity is known for such two-oxide layered systems.

Herein, we demonstrate for the first time that two-oxide BMs prepared by PVD-OAD can be manufactured as polarization active systems behaving as wavelength dependent retarders. We also show that this polarization activity can be systematically and continuously controlled adjusting the refractive index of the liquids circulating through these porous layer structures. To complete the study, other important parts of this research aim at unravelling the nanostructural features responsible for the polarization activity of these porous BM and at simulating their striking polarization behaviour. For this purpose, we have developed a simple optical model where each particular layer in the stack is taken as birefringent in a degree that varies with the refractive index of the liquid filling the pores.

3.2. Experimental and Methods

3.2.1. Fabrication of BMs and optofluidic devices.

Uniform, mechanically stable, and highly porous BMs made of alternated layers of TiO_2 and SiO_2 have been prepared by oblique angle deposition (OAD) according to the procedure reported for single layer deposition[30]. The investigated porous BMs were e-beam evaporated on glass plates of 1.2 × 2.5 cm^2 at a zenithal angle of 70° (α). For electron microscopy characterization, samples were simultaneously deposited on a silicon wafer. Other experimental details can be found in the previous chapter. The BMs consisted of 2×7 individual layers with a thickness of approximately 85 nm, plus one SiO_2 middle layer of approximately 200 nm thickness. As **Figure 3.1** exhibits, four different types of BMs have been prepared depicting *slanted* (i), *zig-zag* (ii), *chiral* (iii) or *vertical* (iv) microstructures. These different morphologies were obtained by keeping fix the substrate for the *slanted* BM or by azimuthally turning the substrate from one layer to the next in the *zig-zag* (180°) and *chiral* (90°) and continuously (40 rpm) in the *vertical* configuration.

For the optofluidic essays the BMs deposited on a glass plate were sandwiched with another glass plate as explained in **Chapter 2**. This simple microfluidic arrangement enabled handling the device as a plate substrate in front of the light beam of a spectrometer and to record spectra while replacing the circulating liquid by simple injection.

3.2.2. Characterization of BMs

Cross section and normal scanning electron microscopy (SEM) images were obtained in a Hitachi S4800 field emission microscope for samples deposited on a silicon wafer that were cleaved for cross-section analysis.

FIB-SEM analysis was performed using a FEI Helios Nanolab 660 tool. First, SEM images were acquired normal to the surface at 2keV primary beam energy using both Secondary Electrons (SE) for topographic and Back Scatter Electrons (BSE) for compositional information. Thereafter, an optional strip of

Pt was deposited using electron beam and ion beam induced deposition in order to prevent ion damage to the surface. Subsequently 2 trenches were milled at 30keV Ga^+ ion energy at 90° angle with one another and oriented parallel and orthogonal to the preference direction seen in the SEM images from the surface. After coarse milling, the side surfaces were polished using a 30keV, 80pA Ga+ ion beam. The cuts were then observed with the electron beam under 52° incidence in the same modes (SE and BSE) as mentioned before. In **Figure 3.2** (**b)**, **c)**, **d)**) the BSE images show a periodic contrast that we attribute to the different atomic numbers of the stacked TiO_2 (bright) and SiO_2 (dark) layers and other possible morphological effects.

UV–vis transmission spectra were recorded in normal incidence with a Cary 100 instrument. In order to analyse the optical activity with polarized light, a linear polarizer was placed before the sample. A second polarizer crossed or aligned with respect the first one was placed after the sample to assess the retarder behaviour of the BMs and optofluidic devices upon azimuthal rotation.

3.2.3. Simulation of the optical response and polarization dependence

Simulation of the optical response of the optofluidic device was done using WVASE32 software [J. A. Woollan Co.] applied to a Bragg microcavity consisting of two Bragg reflectors separated by a “defect layer”. Each Bragg reflector has 7 layers, with a HLHLHLH structure, where H denotes high index material (i.e., TiO_2) and L low index material (i.e., SiO_2). The defect layer was an L material. The optical model relies on the assumption of a birefringent behaviour of the stacked SiO_2 or TiO_2 individual layers in the *slanted*, *zig-zag* and, partially, *chiral* microstructures. The negative uniaxial anisotropic medium in each layer of the *slanted* and *zig-zag BMs* has been characterized by a fast optical axis (low refractive index, n_p) in the direction perpendicular to the *fence-bundling* association and a slow axis (high refractive index, n_b) in the *fence-bundling* plane. For the *chiral* BM, each layer was taken as a positive uniaxial material, with an optical axis normal to the layer, along the nanocolumn direction.

The model interpreted the birefringence $\Delta n = n_p - n_b$ as resulting from the difference in porosity along the-bundling direction and the perpendicular to it on the surface plane. The effect of porosity on the optical behaviour was simulated according to Maxwell–Garnett effective medium approximation to describe a composite material formed by a compact media (i.e., either compact TiO_2 or SiO_2) mixed with voids filled with either air or liquids with different refraction indices. For these calculations, it is assumed that both materials H and L have the same percentage of pore volume and the refractive index of the individual layers was described by a typical Cauchy wavelength dispersion.

3. 3. Results and Discussion

3.3.1. Morphology and bundling association

To determine the nanostructural factors responsible for the polarization activity of the PV-OAD BMs, we have prepared and characterized four types of TiO_2-SiO_2 microcavities depicting different nanocolumn arrangements: i) *slanted*, prepared at constant azimuthal orientation of the substrate during deposition of successive layers; ii) *zig-zag* and iii) *chiral* obtained turning the substrate, respectively, by 180^0 and 90^0 for each layer of the stack; iv) *vertical*, deposited while continuously rotating the substrate around its azimuth. Surprisingly, the two first BMs present a strong polarization activity when interrogated with linearly polarized light, while the two latter are practically insensitive to the polarization. Thanks to a thorough analysis by scanning electron microscopy (SEM) and a field ion beam (FIB) set-up we have been able to show that association of nanocolumns, a rather general phenomenon in OAD films known with the term *bundling*[31,32], is the critical morphological feature responsible for the singular behaviour of the *slanted* and *zig-zag* BMs.

Figure 3.1 displays a series of cross section and normal micrographs taken for the TiO_2/SiO_2 BMs deposited on a silicon wafer. The cross section images and schemes in this figure show the characteristic nanocolumnar microstructure of the *slanted* **(i)**, *zig-zag* **(ii)**, *vertical* **(iii)** and *chiral* **(iv)** multilayer systems. The normal images of the *slanted* and *zig-zag* and, to a minor extent, the *chiral* BMs also reveal a preferential arrangement of material along the direction perpendicular to the vapour flux, an anisotropy which is further supported by the 2-fold symmetry of their Fourier transforms (FT) reported in the figure. Meanwhile, the highly symmetric FT shape of the *vertical* BMs clearly reflects an uncorrelated distribution of column terminations at the surface of this sample.

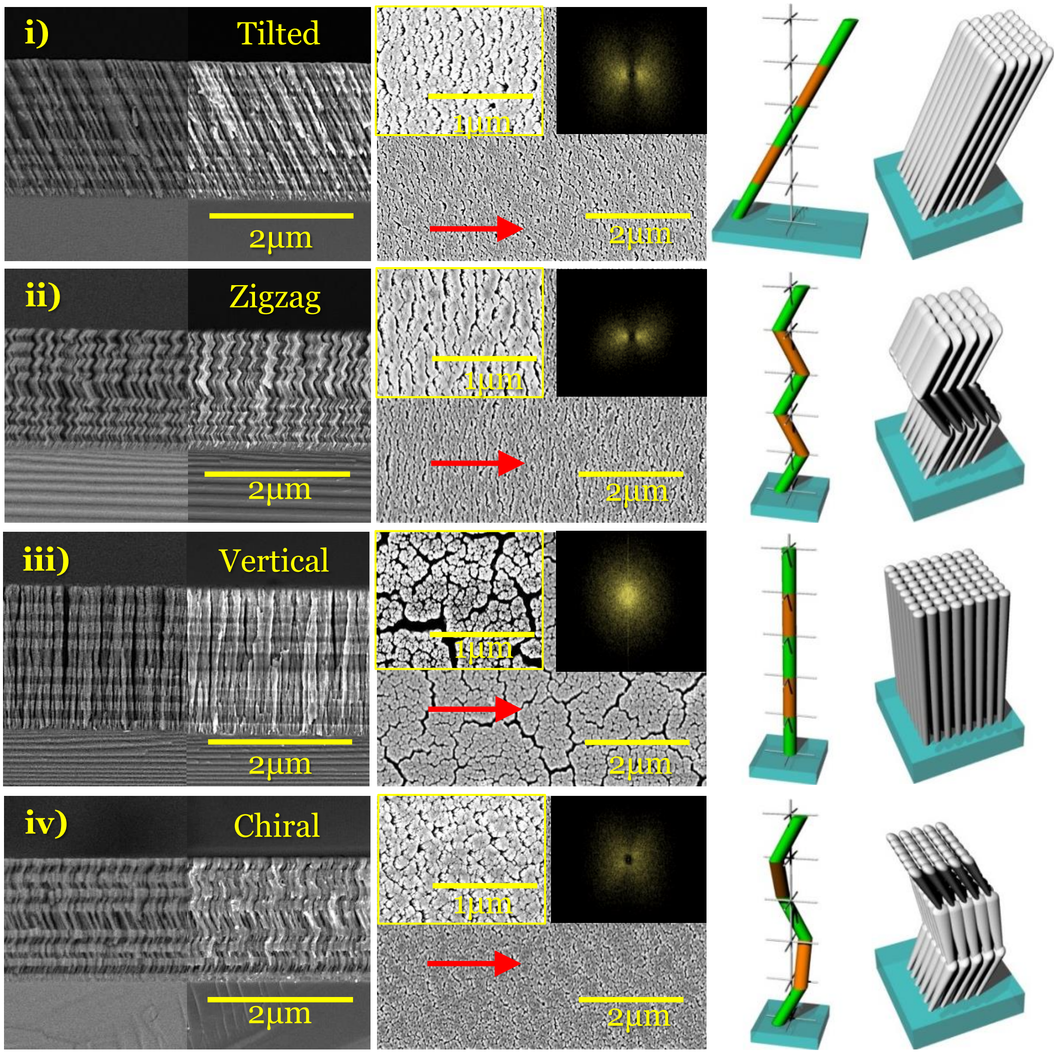

Figure 3.1. i-iv) Cross section SE and BSE micrographs (left), and two scale normal SE micrographs (right) of the *slanted*, *zig-zag*, *vertical* and *chiral* BMs. The inserted diagrams in the normal micrographs show the FTs calculated from these images. The red arrows indicate the vapour flux direction of arrival. The schemes at the right represent the ideal geometric arrangement of the nanocolumns in the successive stacked layers of the BM structures.

Bundling association of nanocolumns is believed to extend along the whole thickness of single oxide OAD thin films[31–34], a feature that we confirmed by FIB-SEM analysis of the BMs. **Figure 3.2** shows a series of cross section micrographs along the π (perpendicular to the film surface in a direction parallel to the *bundling*), Δ (perpendicular to the film surface in a direction perpendicular to the *bundling*), and Ω planes (close to the perpendicular to the nanocolums direction) defined in the scheme of the *slanted* microstructure included in this figure. The layered distribution of brightness observed in the Back Scatter Electron (BSE) micrographs reflects the different atomic numbers of the SiO_2 and TiO_2 layers. In addition, the π-plane micrographs (i.e., panels **a)** and **b)**) of the *slanted* BM show that nanocolumns associate along the whole film thickness, i.e., association is not restricted to a single layer of the stack. We will call this nanocolumn association extending from one material layer to the next as *fence-bundling,* a specific microstructural feature that has not been previously reported in the literature. In the Δ-plane image (i.e., panel **c)**), it is also apparent that large mesopores extends through the whole material and that no disruption of nanocolumns morphology occurs when passing from one layer (e.g., TiO_2) to the next (e.g., SiO_2). Finally, the image taken along the Ω-plane (i.e., panel **d)**) confirms that both mesopores and nanocolumns arrange linearly along the surface bundling direction. Similarly, images taken along the π and Δ planes for the *zig-zag* microstructure (panels **e)** and **f)**) show the development of equivalent *fence-bundling* association extending through the whole BM. Lack of *fence-bundling* association in the *vertical* BM and only a negligible association in the individual layers in the *chiral* BM (i.e., panels **g)** and **f)** and are clear differences with respect to the two other photonic structures.

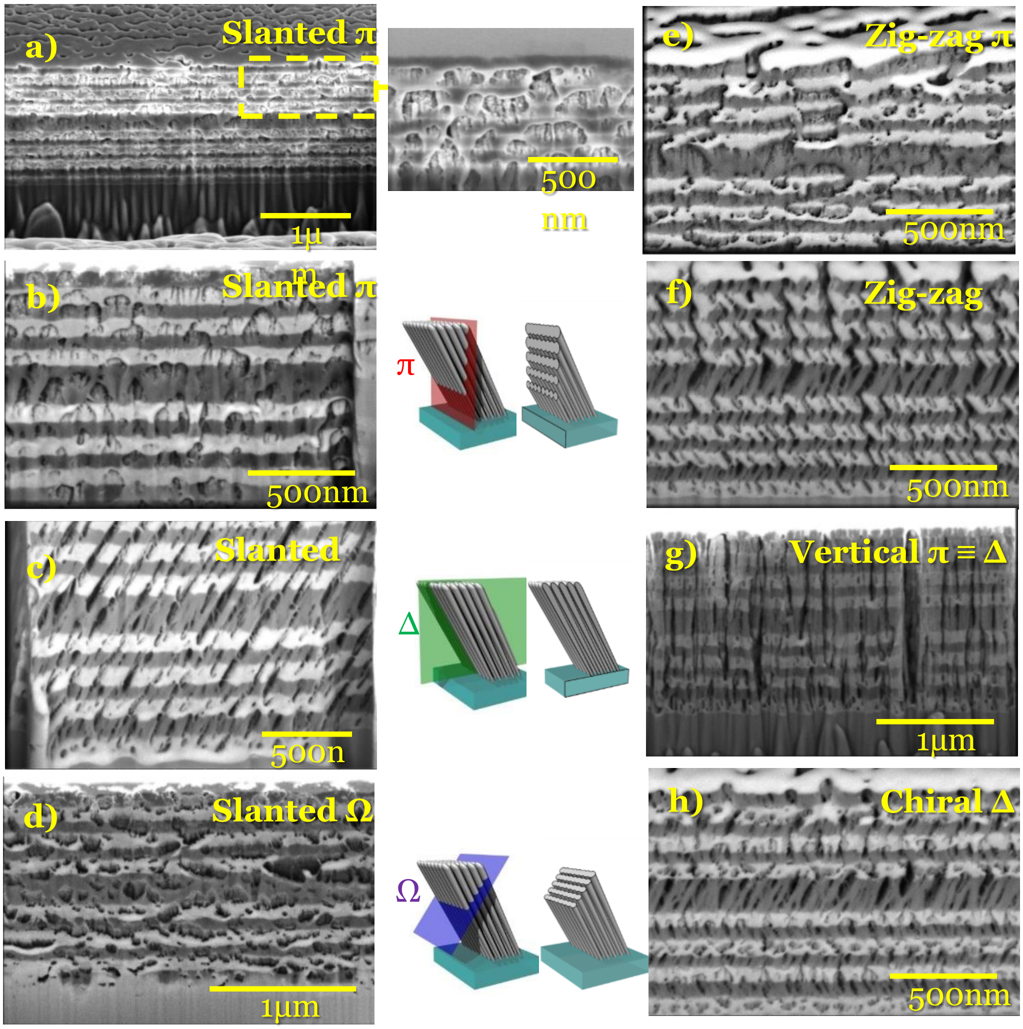

Figure 3.2. FIB-SEM cross section images of the BMs and scheme for a *slanted* structure showing the cross section planes used for the analysis and the resulting lateral surfaces in each case. a) to d) BSE images for the *slanted* BMs along the different analysis planes: a) micrograph taken for a cross section along plane π; b) the same as A in an enlarged scale; c) micrograph taken for a cross section along plane Δ; d) micrograph taken for a cross section along plane Ω. The enlarged image at the right of micrographs a) is taken in SE mode to better visualize the lateral surface generated by the ion erosion. e) and f) BSE cross section micrographs taken for the *zig-zag* microstructure along planes π and Δ respectively. g) BSE cross section micrograph taken for the *vertical* BM along plane Δ. h) Ditto for a *chiral* BM.

3.3.2. Polarization activity of planar BMs

The *fence-bundling* arrangement of nanocolumns in the *slanted* and *zig-zag* BMs has direct effects on the optical properties of these structures when examined with linearly polarized light. **Figure 3.3** shows a series of optical transmittance spectra recorded around the resonant peak for the four studied BMs using linearly polarized light oriented with its polarization plane parallel (i.e. φ=0^0) or perpendicular (i.e. φ=90^0) to the surface *bundling* direction. Unlike the spectra of the *vertical* and *chiral* BMs which are almost unaffected by the orientation of polarized light, the *slanted* and *zig-zag* BMs develop two different resonant peaks for φ equal to 0^0 and 90^0, a double peak structure for other orientations and an almost equivalent intensity of the two peaks when φ=45^0. The separation between the two resonant peaks is 18 nm (*slanted*) and 23 nm (*zig-zag*). The positions and Q factors of the resonant peaks summarized in **Table 3.1** are practically identical for the two polarizations in the *vertical* BMs, but strongly differ for the *titled* and *zig-zag* structures and present slight changes for the *chiral* BM.

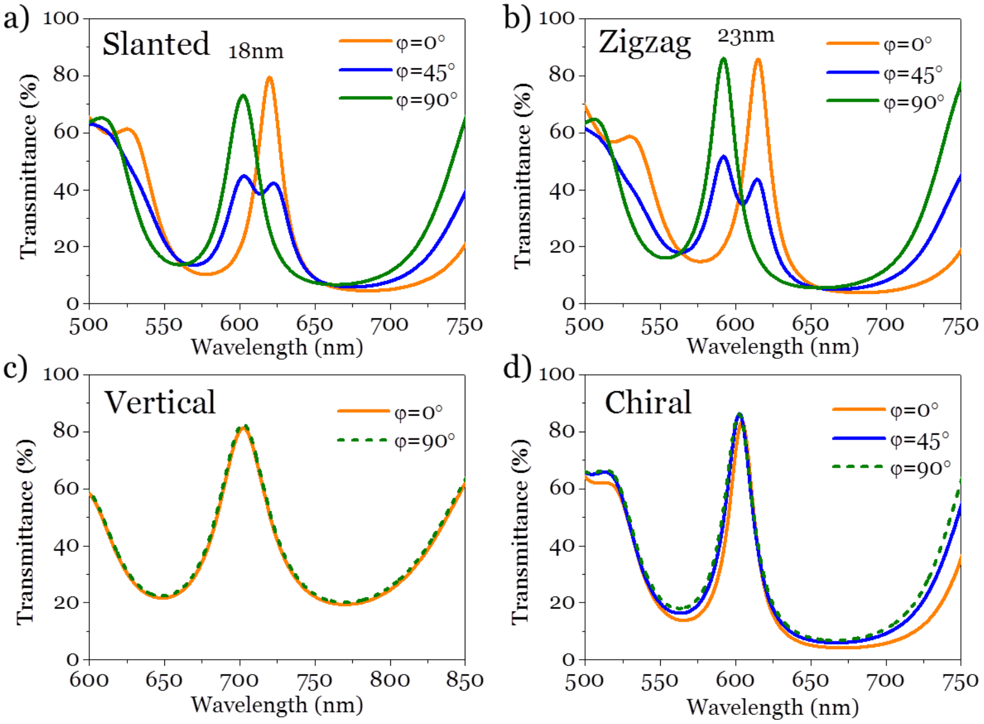

Figure 3.3. Transmission spectra recorded around the resonant peak for the indicated BMs with linearly polarized light oriented at 0^0, 45^0 and 90^0 with respect to the perpendicular to the arrival flux direction.

Table 3.1. Resonant peaks positions and Q factors of the different Bragg Microcavities.

	φ(°)	*Slanted*	*Zig-zag*	*Vertical*	*Chiral*
Position (nm)	0	619.8	614.6	702.5	603.9
	90	601.9	591.6	702.7	602.2
Q factor	0	31.9	31.9	19.9	30.5
	90	26.5	28.4	19.7	26.8

The optical behaviour depicted in **Figure 3.3** can be simulated with an optical interference model where the SiO_2 or TiO_2 stacked layers of the BM are birefringent. For the *slanted*, *zig-zag* and *chiral* structures, the negative uniaxial anisotropy associated to each individual layer can be described by a fast optical axis (low refractive index) along a surface direction perpendicular to the *fence-bundling* (n_p) and a slow axis (high refractive index) along the *fence-bundling* direction at the surface plane (n_b). **Figure 3.4 a)** and **b)** demonstrates that this simple model properly reproduces the transmittance spectra of the *zig-zag* BMs upon continuous φ rotation. This angular dependence supports the use of this BM to determine the orientation of the polarization plane of light. The birefringence (i.e. $\Delta n=n_p-n_b$) of the individual layers introduced in the model to properly reproduce the optical behaviour of the *zig-zag* BM amounts to $\Delta n=-0.150$ and -0.043 for TiO_2 and SiO_2 layers, respectively. From a structural point of view, this optical anisotropy stands for a difference in void fraction of ~20% between the more compact *fence-bundling* direction and the perpendicular to it. A similar analysis for the *slanted* structure, **Figure 3.4 c)** and **d)**, confirms the validity of this optical model to simulate the polarization response of the polarization active BMs.

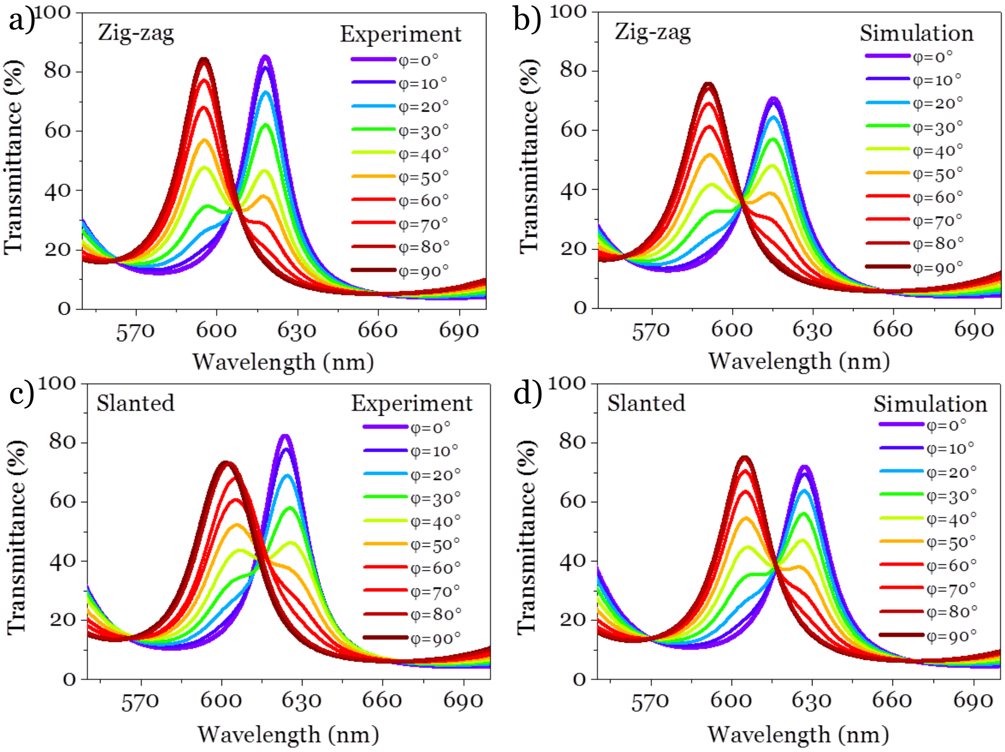

Figure 3.4. Polarization angle dependence. Experimental a) and simulated b) spectra around the resonant peak of a *zig-zag* BM when recorded with linearly polarized light at the indicated angles formed between the polarization plane and the *bundling* direction (i.e., azimuthally rotating the sample by the indicated angles). c) & d) Ditto for a *slanted* BM.

3.3.3. BM thin films as wave retarders

Zig-zag and *slanted* BMs behave as optical retarders or wave-plates[35] and are characterized by resolving a linearly polarised beam into two orthogonal components separated by a wavelength dependent phase shift. **Figure 3.5** shows a scheme of the polarization state of light (**Figure 3.5 a)**) and the transmittance spectra recorded through the *zig-zag* BM placed between two polarizers either in crossed (**Figure 3.5 b)**) or aligned (**Figure 3.5 d)**) configurations. The function of the first polarizer is to generate linearly polarized light, while the transmitted spectra in the figure are recorded as a function of the angles φ_1, φ_2 formed by the bundling direction of sample and the first and second polarizer planes, respectively.

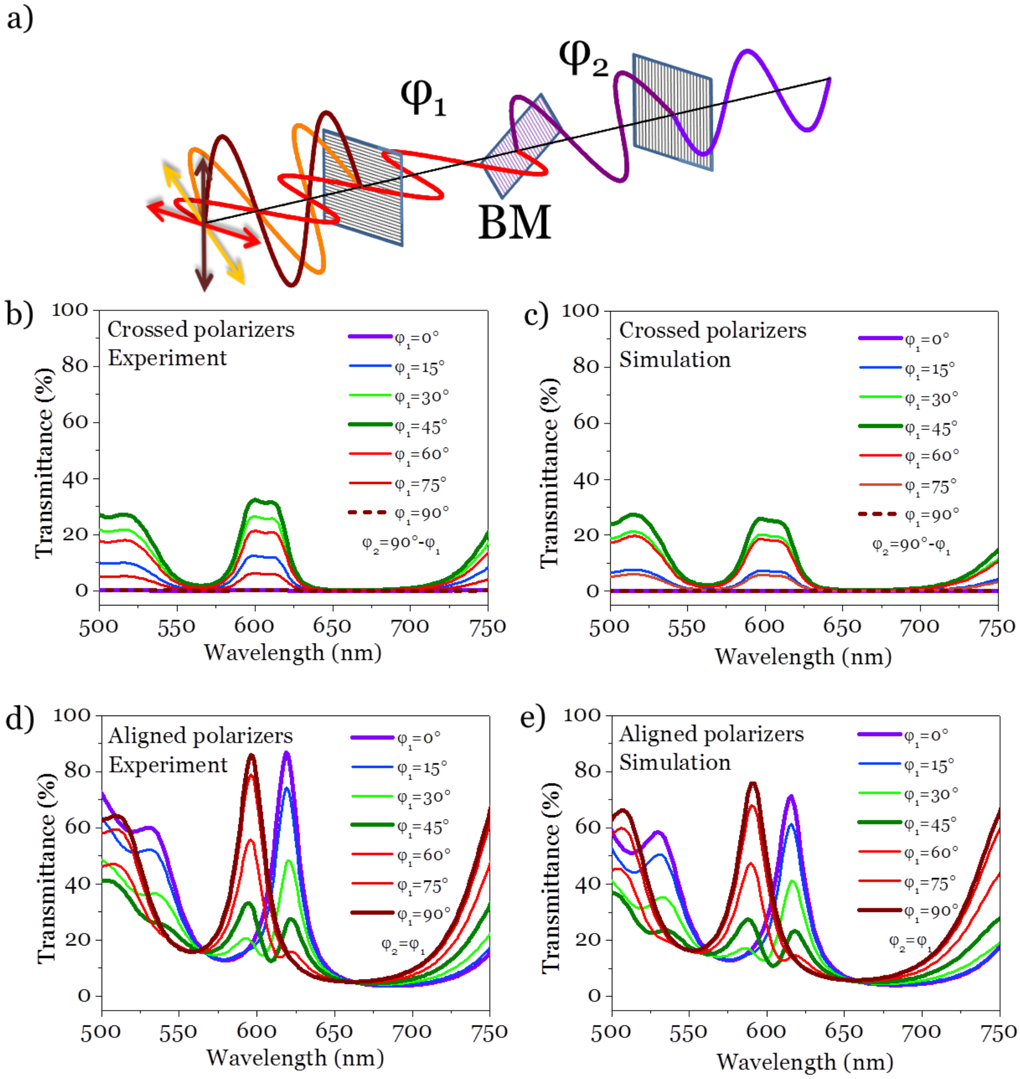

Figure 3.5. Polarization angle dependence through a second polarizer. a) Scheme of the two polarizers set up and light polarization behaviour with the polarization active BM placed in-between and perpendicular to the direction of light. This particular representation corresponds to the cross polarizer configuration. b, c) Evolution of experimental b) and simulated c) spectra around the resonant peak of a *zig-zag* BM when recorded through two cross polarizers by azimuthally rotating the BM as indicated. e) Evolution of experimental d) and simulated e) spectra of the resonant peak of a *zig-zag* BM when recorded through two parallel polarizers by azimuthally rotating the BM as indicated.

Figure 3.6 Exhibits selected results of similar experiments conducted with the **a)** *slanted*, **b)** *vertical* and **c)** *chiral* BMs showing that, as expected, only the former presents similar retarder behaviour.

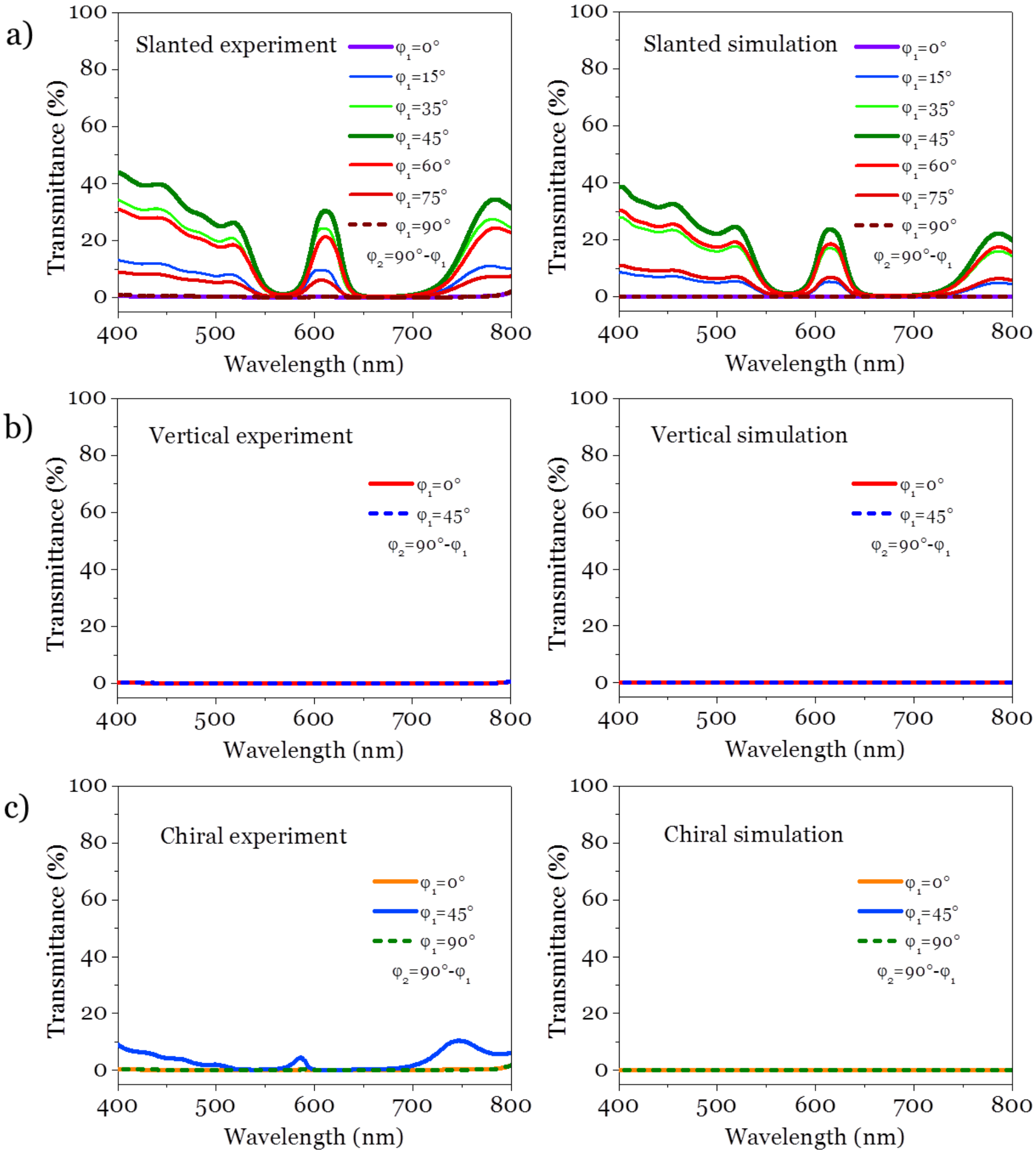

Figure 3.6. Experimental (left) and simulated (right) evolution of spectra and spectra for *slanted* a), *vertical* b) and *chiral* c) BMs when recorded with two cross polarizers and the indicated azimuthal orientation of the sample according to the scheme of Figure 3.5.

It is apparent in **Figure 3.5** that for the cross-polarizer configuration and the BM bundling direction aligned along the polarization plane of light (i.e. $\varphi_1=90^0$ and $\varphi_2=0^0$) (**Figure 3.5 b)**), no light passes through the system. Meanwhile, progressively more intense spectra are recorded when azimuthally rotating the BM (i.e., $\varphi_1<90^0$ and $\varphi_2=90^0-\varphi_1$) up to reach a maximum intensity for $\varphi_1=\varphi_2=45^0$, an optical behaviour that could be successfully reproduced by simulation (c.f. **Figure 3.5c)**). When the BM is placed between two aligned polarizers at $\varphi_1=\varphi_2=0^0$ (see **Figure 3.5 d)**) and simulated spectra in **Figure 3.5 e)**), the transmittance spectrum results identical to that recorded in the absence of the second polarizer (i.e., identical to that reported in **Figure 3.4** for $\varphi=0^0$). The transmittance spectra drastically changes for other azimuthal orientations of the sample with respect to the aligned polarizers (i.e., for $\varphi_1=\varphi_2\neq 0^0$), indicating that the BM modifies the polarization state of light. Thus, for $\varphi_1=\varphi_2>0^0$, there is a progressive transfer of intensity from the high to the short wavelength resonant peak. Then, these two peaks depict a similar intensity for $\varphi_1=\varphi_2=45^0$, experience a reversal in intensity ratio for $\varphi_1=\varphi_2>45^0$ and finally reach a maximum intensity/complete neglect at $\varphi_1=\varphi_2=90^0$.

The pure retarder behaviour of the BM is confirmed verifying that the sum of the crossed and parallel polarizers spectra in **Figure 3.5** and **Figure 3.6** matches the spectra in **Figure 3.4** obtained with linear polarized light. Further insights in this polarization behaviour, in particular into the light ellipticity as a function of wavelength and azimuthal orientation of sample, could be retrieved calculating the intensity ratio between signals measured with cross and parallel polarizers. Selected wavelength dependences of this ellipticity are reported in **Figure 3.7**, being worth noting that when equivalent transmitted intensities are measured for the cross and parallel configurations, the BM acts as a perfect quarter-wave plate[35].

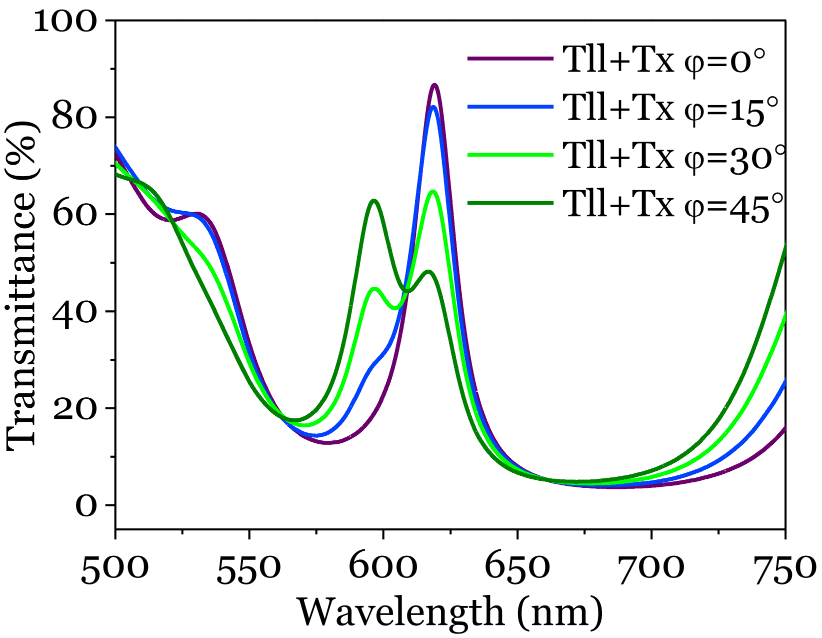

Figure 3.7. Representation of the sum of the transmission spectra recorded with the parallel (II) and crossed (x) configurations and the indicated azimuthal orientations of the *zig-zag* BM.

The singular wavelength retarder behaviour of the optically active BMs evidenced in **Figures 3.5** and **3.6** stems from interferences within the multilayer structure, whereby each layer behaves as an individual retarder inducing a retardance $\delta = \Delta n * t/\lambda$, where t is the thickness of the birefringent medium (i.e., layer thickness), λ the wavelength of light and Δn the difference between extraordinary and the ordinary refractive indices of the layer, $\Delta n = n_p - n_b$.

Despite the quite different arrangement of nanocolumns in the *zig-zag* and *slanted* BMs, their equivalent retarder behaviour (see **Figure 3.5 a)** and **Figure 3.6**) points to that the *fence-bundling* association of nanocolumns is the common microstructural feature inducing the single layer birefringence responsible for the wave retarder response of the whole device. The lack of *fence-bundling* association in the *vertical* BMs discards such a single-layer birefringence and consequently prevents any wave retarder function for the whole structure (see **Figure 3.5 a)** and **Figure 3.6 b)** and **c)**). For the *chiral* BM, besides the limited *fence-bundling* association observed in its microstructure (c.f., **Figure 3.2 f)**), the 90^0 change in the tilting orientation of nanocolumns in successive layers precludes a common reference orientation for the slow and fast optical axis in different layers and, therefore, any significant polarization activity for the whole device.

3.3.4. Optofluidic behaviour of polarization active BMs

An outstanding characteristic of PV-OAD single or stacked multilayer photonic crystals or BMs, is their high porosity and the possibility that their optical response can be altered by liquid infiltration[28,29]. In previous studies on the liquid infiltration of 1DPC and *chiral* BMs (i.e., polarization inactive) we found a pore fraction of ca. 50% that were filled with liquids in its practical totality. A similar value is expected for the BMs studied here. **Figure 3.8** shows a series of transmittance spectra recorded for the polarization active *zig-zag* BM successively infiltrated with water (n: 1.333), ethanol (n: 1.362) and toluene (n: 1.496).

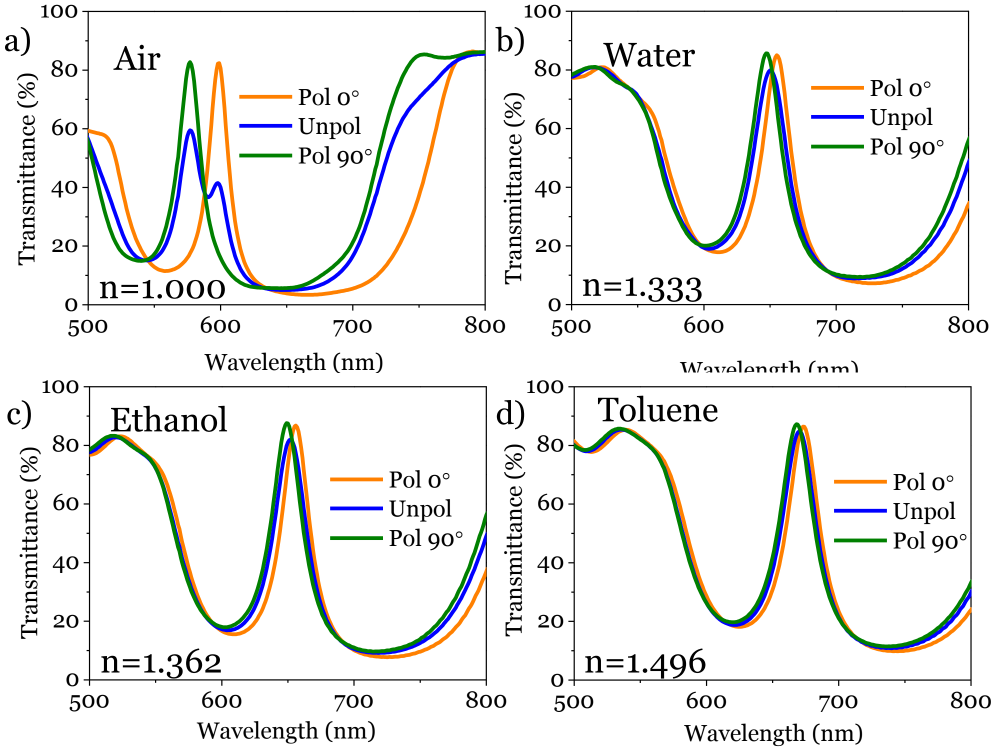

Figure 3.8. Optofluidic modulation of polarization behaviour. Experimental spectra for a *zig-zag* BM recorded with unpolarised and 0^0 and 90^0 linearly polarized light for the as-prepared (i.e. air filled) a) and water b), ethanol c) and toluene d) infiltrated structure.

It is apparent that, besides a shift in the resonant peak positions, the magnitude of wavelength splitting between the resonant peaks recorded with unpolarized light decreases from 23 nm in the originally empty *zig-zag* device to 8, 7 and 5 nm, when infiltrated with these liquids. The well-matched simulated spectra in **Figure 3.9** sustains that filling the pores of the structure with these liquids produces a decrease in the birefringence of the individual layers from $\Delta n_{TiO_2} = -0.150$ and $\Delta n_{SiO_2} = -0.043$ when the BM is empty (i.e., filled with air) to $\Delta n_{TiO_2} = -0.112$ and $\Delta n_{SiO_2} = -0.011$ (water); $\Delta n_{TiO_2} = -0.109$ and $\Delta n_{SiO_2} = -0.009$ (ethanol); or $\Delta n_{TiO_2} = -0.094$ and $\Delta n_{SiO_2} = 0.004$ (toluene).

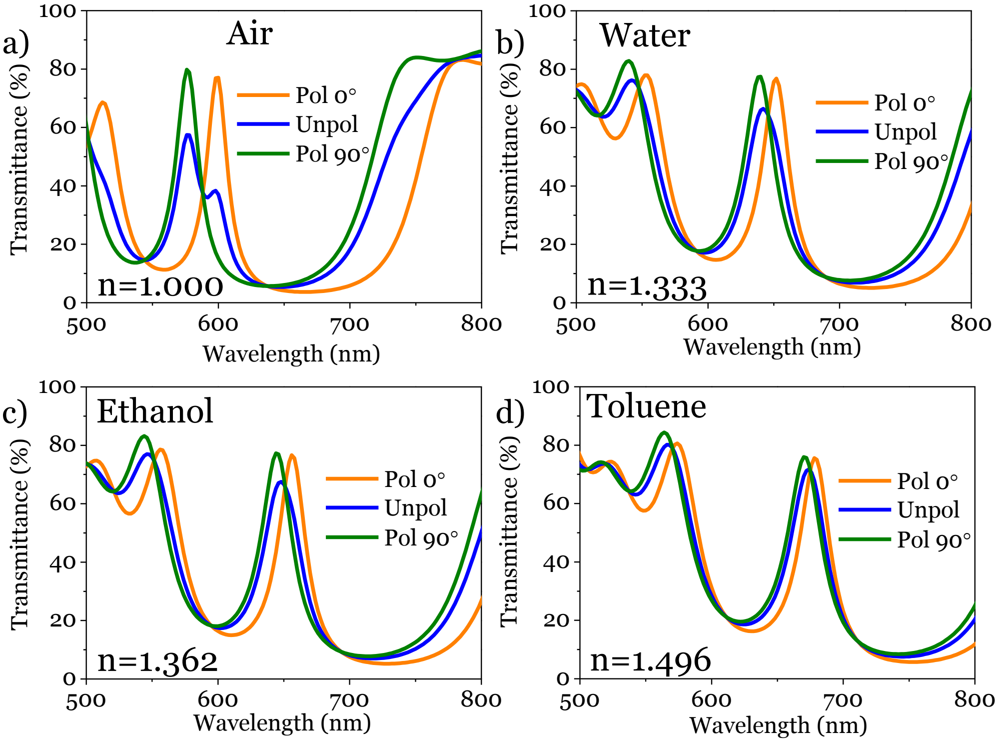

Figure 3.9. Simulated spectra for a *zig-zag* BM recorded with unpolarised and 0^0 and 90^0 linearly polarized light for the as-prepared (i.e. air filled) a) and water b), ethanol c) and toluene d) infiltrated structure.

Furthermore, it is possible to verify that the *retarder* function of the active BMs can be modulated by liquid infiltration. Thus, although liquid infiltration attenuates the optical activity of the BMs, this is accompanied by changes in shape and intensity of the resonant peaks which constitute the basis of the outstanding optofluidic effects of these devices. **Figure 3.10** shows the spectra recorded with the cross and parallel polarizers configurations and a

$\varphi_1=\varphi_2=45^0$ azimuthal orientation of the *zig-zag* BM filled with air (taken as a reference), water, ethanol and toluene.

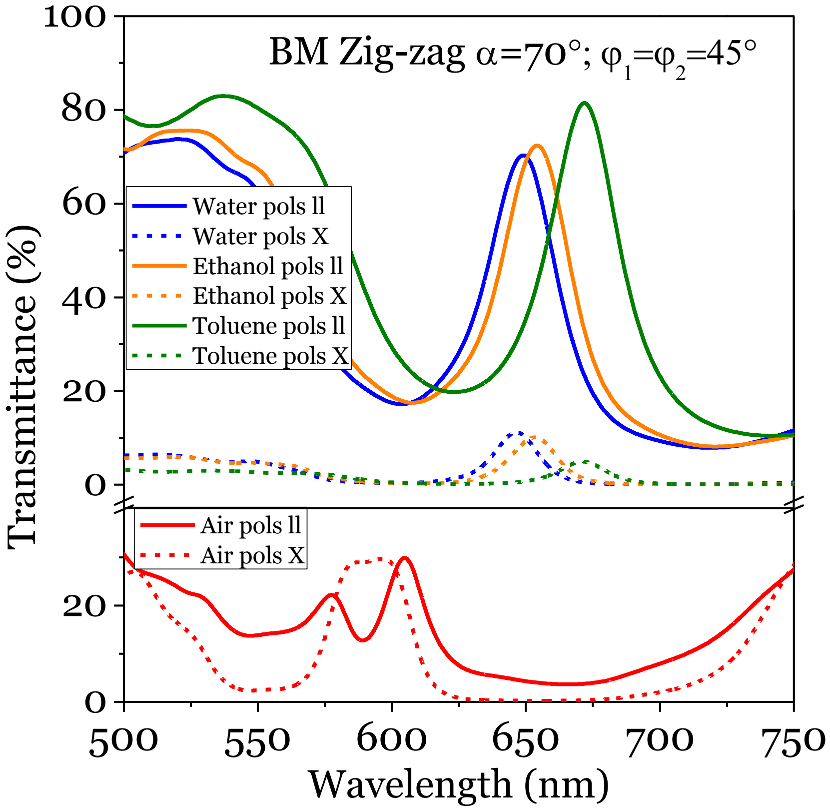

Figure 3.10. Optofluidic modulation of polarization behaviour. Transmittance spectra recorded through the *zig-zag* BM azimuthally oriented 45^0 with respect to the two polarisers either in cross (x) or parallel (II) configurations. Bottom) Spectra recorded for the BM pores filled with air. Top) Spectra recorded for the BM pores filled with liquids of different refraction indices as indicated.

As expected, increasing the refractive index of the liquid produces a shift to longer wavelengths in the position of the resonant peaks. In addition, their intensities increase/decrease for the cross and parallel configurations as the refraction index of the infiltration liquid increases. An outstanding result of this experiment is that, after calibration, the intensity ratio between the two resonant peaks is a direct measurement of the refraction index of the infiltration liquid. The potential of this behaviour for analytical applications with solutions (the refraction index directly correlates with solute concentrations) is quite obvious particularly because, even if the actual two resonant peak intensities would be proportional to the excitation beam flux, their ratio would be independent of malfunctions or time instabilities of the light source.

3.3.5. Polarization activity and fence-bundling association

From a microstructural point of view, the reported optofluidic response of the polarization active *zig-zag* and *slanted* BMs depends on the development of a *fence-bundling* association between nanocolumns. Bundling association in PV-OAD thin films has been known since the earliest investigations with this deposition procedure[31,32], although this microstructural feature has been scarcely used for the development of optical devices[33,34].

3.4. Conclusions

The present study constitutes a first example of the interplay between microstructure, light polarization and liquid-controlled properties of OAD layered materials that should serve to develop new applications in fields like sensing, optical device manufacturing and optofluidics. We have demonstrated that the *fence-bundling* association of nanocolumns in multilayer thin films deposited by evaporation at oblique angles can be engineered to develop polarization active BMs acting as wavelength retarders. Filling the highly porous structure of these multilayers with liquids attenuates the optical activity and gives rise to quite striking optofluidic responses easily monitored by the position, shape and intensity of the resonant peak(s). In particular, we have shown that the liquid modulation of the retarder function of the BM can be used to detect the orientation of polarization plane of light or for the analysis of liquids when integrated in microfluidic devices. Taking into account the easy manufacturing procedure of these multilayer structures, its compatibility with any kind of substrates and the possibility of using masks, we anticipate a wide range of optofluidic applications for this type of planar BM systems.

3.5. References

1. Erickson, D., Sinton, D. & Psaltis, D. Optofluidics for energy applications. *Nat. Photonics* **5,** 583–590 (2011).
2. Monat, C., Domachuk, P. & Eggleton, B. J. Integrated optofluidics: A new river of light. *Nat. Photonics* **1,** 106–114 (2007).
3. Schmidt, H. & Hawkins, A. R. The photonic integration of non-solid media using optofluidics. *Nat. Photonics* **5,** 598–604 (2011).
4. Fan, X. & White, I. M. Optofluidic microsystems for chemical and biological analysis. *Nat. Photonics* **5,** 591–597 (2011).
5. Dong, L., Agarwal, A. K., Beebe, D. J. & Jiang, H. Adaptive liquid microlenses activated by stimuli-responsive hydrogels. *Nature* **442,** 551–554 (2006).
6. Fei, P. *et al.* Discretely tunable optofluidic compound microlenses. *Lab. Chip* **11,** 2835–2841 (2011).
7. Song, W. & Psaltis, D. Pneumatically tunable optofluidic dye laser. *Appl. Phys. Lett.* **96,** 081101 (2010).
8. Heng, X. *et al.* Optofluidic microscopy—a method for implementing a high resolution optical microscope on a chip. *Lab. Chip* **6,** 1274–1276 (2006).
9. Fujiki, M. *et al.* Chiral optofluidics: gigantic circularly polarized light enhancement of all-trans-poly(9,9-di-n-octylfluorene-2,7-vinylene) during mirror-symmetry-breaking aggregation by optically tuning fluidic media. *RSC Adv.* **2,** 6663–6671 (2012).
10. Hawkeye, M. M., Taschuk, M. T. & Brett, M. J. in *Glancing Angle Deposition of Thin Films: engineering the nanoscale*. Wiley Series in Materials for electronic & optoelectronic applications, September 29, 2014
11. Barranco, A., Borras, A., Gonzalez-Elipe, A. R. & Palmero, A. Perspectives on oblique angle deposition of thin films: From fundamentals to devices. *Prog. Mater. Sci.* **76,** 59–153 (2016).
12. Xi, J.-Q. *et al.* Optical thin-film materials with low refractive index for broadband elimination of Fresnel reflection. *Nat. Photonics* **1,** 176–179 (2007).
13. Poxson, D. J. *et al.* High-performance antireflection coatings utilizing nanoporous layers. *MRS Bull.* **36,** 434–438 (2011).
14. Popta, A. C. van, Cheng, J., Sit, J. C. & Brett, M. J. Birefringence enhancement in annealed TiO2 thin films. *J. Appl. Phys.* **102,** 013517 (2007).
15. Hodgkinson, I., Wu, Q. hong & Hazel, J. Empirical Equations for the Principal Refractive Indices and Column Angle of Obliquely Deposited Films of Tantalum Oxide, Titanium Oxide, and Zirconium Oxide. *Appl. Opt.* **37,** 2653 (1998).

16. Messier, R., Venugopal, V. C. & Sunal, P. D. Origin and evolution of sculptured thin films. *J. Vac. Sci. Technol. A* **18,** 1538–1545 (2000).
17. H. Lakhtakia, R. Messier, *Sculptured Thin films, Nanoengineered Morphology and Optics*, Spie Press, Washington, USA **2005**.
18. Hodgkinson, I. & Wu, Q. h. Inorganic Chiral Optical Materials. *Adv. Mater.* **13,** 889–897 (2001).
19. Hodgkinson, I., Wu, Q. hong, Knight, B., Lakhtakia, A. & Robbie, K. Vacuum Deposition of Chiral Sculptured Thin Films with High Optical Activity. *Appl. Opt.* **39,** 642 (2000).
20. Lakhtakia, A., McCall, M. W., Sherwin, J. A., Wu, Q. H. & Hodgkinson, I. J. Sculptured-thin-film spectral holes for optical sensing of fluids. *Opt. Commun.* **194,** 33–46 (2001).
21. Hodgkinson, I. J., Wu, Q. H., Thorn, K. E., Lakhtakia, A. & McCall, M. W. Spacerless circular-polarization spectral-hole filters using chiral sculptured thin films: theory and experiment. *Opt. Commun.* **184,** 57–66 (2000).
22. Popta, A. C. van, Brett, M. J. & Sit, J. C. Double-handed circular Bragg phenomena in polygonal helix thin films. *J. Appl. Phys.* **98,** 083517 (2005).
23. Krause, K. M. & Brett, M. J. Spatially Graded Nanostructured Chiral Films as Tunable Circular Polarizers. *Adv. Funct. Mater.* **18,** 3111–3118 (2008).
24. Hawkeye, M. M. & Brett, M. J. Narrow bandpass optical filters fabricated with one-dimensionally periodic inhomogeneous thin films. *J. Appl. Phys.* **100,** 044322 (2006).
25. Liu, Y. J. *et al.* High-speed optical humidity sensors based on chiral sculptured thin films. *Sens. Actuators B Chem.* **156,** 593–598 (2011).
26. Leontyev, V. *et al.* Selective transmittance of linearly polarized light in thin films rationally designed by FDTD and FDFD theories and fabricated by glancing angle deposition. *J. Appl. Phys.* **104,** 104302 (2008).
27. Gospodyn, J. *et al.* Photoluminescence emission profiles of Y_2O_3:Eu films composed of high-low density stacks produced by glancing angle deposition. *Appl. Opt.* **47,** 2798 (2008).
28. González-García, L., Lozano, G., Barranco, A., Míguez, H. & González-Elipe, A. R. TiO2–SiO2 one-dimensional photonic crystals of controlled porosity by glancing angle physical vapour deposition. *J. Mater. Chem.* **20,** 6408–6412 (2010).
29. Oliva-Ramirez, M. *et al.* Liquids Analysis with Optofluidic Bragg Microcavities. *ACS Appl. Mater. Interfaces* **5,** 6743–6750 (2013).

30. Lola González-García, J. P.-B. Correlation lengths, porosity and water adsorption in TiO_2 thin films prepared by glancing angle deposition. *Nanotechnology* **23,** 205701 (2012).
31. Van Kranenburg, H. & Lodder, C. Tailoring growth and local composition by oblique-incidence deposition: a review and new experimental data. *Mater. Sci. Eng. R Rep.* **11,** 295–354 (1994).
32. Stagon, S. P., Huang, H., Baldwin, J. K. & Misra, A. Anomaly of film porosity dependence on deposition rate. *Appl. Phys. Lett.* **100,** 061601 (2012).
33. Gonzalez-García, L. *et al.* Tuning Dichroic Plasmon Resonance Modes of Gold Nanoparticles in Optical Thin Films. *Adv. Funct. Mater.* **23,** 1655–1663 (2013).
34. Sanchez-Valencia, J. R. *et al.* Selective Dichroic Patterning by Nanosecond Laser Treatment of Ag Nanostripes. *Adv. Mater.* **23,** 848–853 (2011).
35. M. Bass. *Handbook of Optics, Fundamentals, Techniques and Design*. McGraw-Hill, Inc. New York, USA **1995**.

Chapter 4

Optofluidic analysis with polarization active Bragg Microcavities prepared by Oblique Angle Deposition

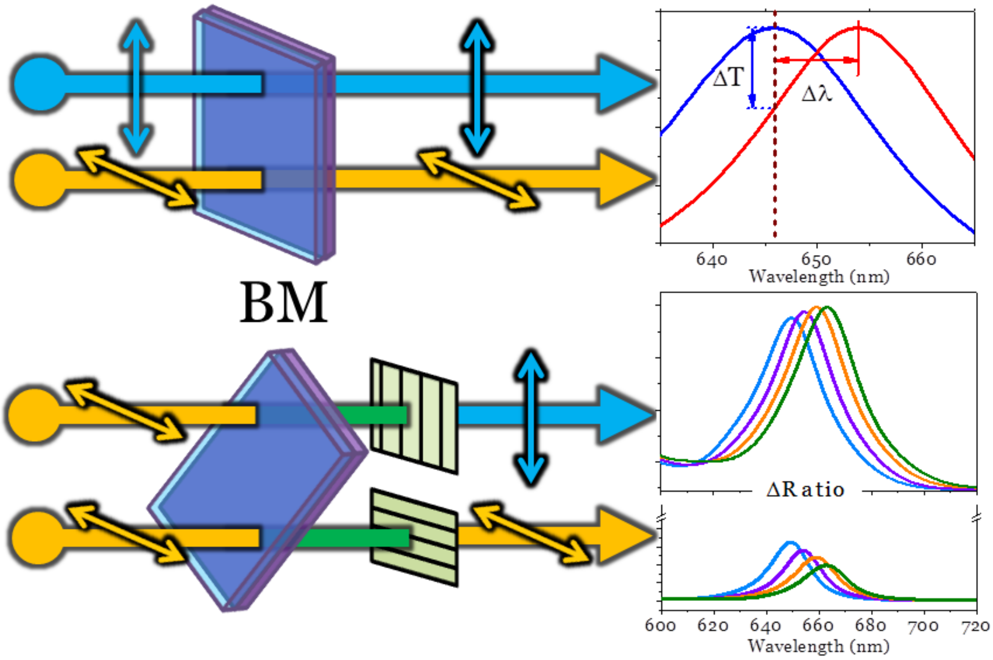

4.1. Introduction

Photonic crystal sensors are of great interest for liquid analysis and represent a straightforward approach for the development of label-free integrated sensors.[1] In general, photonic structures offer a higher sensitivity than single layer structures[2,3] because their use involves optical interference processes that enhance the small changes otherwise appearing in the optical detection parameters. Thanks to a strong photon confinement, ultra-small volumes in the femtoliter level can be tested using photonic crystals sensors, making possible the realization of the "Lab on a chip" concept.[4,5] Three-dimensional ordered opal photonic sensors[6], cavities[7,8] and waveguides[9] in two-dimensional photonic crystals, and slotted photonic crystals heterostructures in cavities[10], are some examples of photonic liquid sensors relying on the determination of refractive index changes. In a similar line, optically active Biophotonic Sensing Cells made of an ordered arrangement of nanopillars have been recently reported to characterize liquids through their different response towards *s* and *p* polarizations[11].

Following the redshift of a feature of the spectrum is likely the most common monitoring method of liquids when using photonic sensors[6–10,12], although changes in transmittance has been proposed as well[9]. For example, J. Gao et al. used a single porous silicon layer to determine the concentration of ethanol in an air stream following the changes in transmittance at a single selected wavelength[13]. Certainly, a high sensitivity can be achieved by this method if the resonant peak or other spectral features are sharp and the redshift in the spectrum produces a high decrease in transmittance at a fixed wavelength.

Previously, our research group presented the synthesis and characterization of a porous one-dimensional photonic crystal, also known as a Bragg Reflector, showing that it experienced a spectral redshift when infiltrated with liquids[12]. A Bragg Reflector consists of a multilayer of two materials with different refractive indices and controlled thickness that, due to optical interference processes, presents a high reflectivity zone o *band gap* in a certain region of the spectrum. In the Bragg Microcavity (BM) photonic structure discussed in chapters 2 and 3, the multilayer stack incorporates a thicker central layer that breaks the periodicity of the Bragg Reflector and gives rise to a resonant peak in the middle of the band gap region providing a narrow range of wavelengths for maximum transmission. These Bragg reflector and microcavity have been prepared by Physical Vapor Deposition at Oblique Angle (PV-OAD), a suitable technique for tailoring the fabrication of porous planar photonic structures[14]. Its usefulness relies on the possibility to adjust the thicknesses and porosity of layers through the control of its characteristic nanocolumnar growth. Others outstanding features of this kind of growth mode such as the birefringence of the films can be also used to enhance the performance of photonic devices constructed by the stacking of such thin films.[15] The modulation of the porosity and refractive index of the stacked layers during their deposition by PV-OAD has been a common strategy to build planar Bragg Reflectors using a single material such as TiO_2[16,17], ITO[18,19] or silicon.[15] Variations in the composition of the porous multilayer, e.g., using OAD to alternatively deposit TiO_2 and SiO_2 layers, has been used for the first time in our research group [12] and then by others [20,21] to grow this type of planar photonic structures.

Typically, liquid analysis with planar porous photonic crystals relies on changes in the effective refractive index (**n_{eff}**) of the system. When a liquid penetrates in the connected porosity of these planar structures, **n_{eff}** increases and leads to a shift to larger wavelength (redshift) in their optical spectra. The magnitude of this shift is directly related to the refractive index of the infiltrating liquid, so that the magnitude of the shift is directly dependent on the liquid filling its pores. In **Chapter 2** we have shown that using a Bragg Microcavity, this redshift effect can be used to analyze solutions due to the rise of refractive index when the concentration of an analyte increases[22]. In that chapter we have shown that it can be used to analyze mixtures of liquids with different refractive indices.

The usual measurement method in industry of sucrose, glucose or ascorbic acid consists of monitoring the rotation plane of light upon passage through the solution, a parameter that will be a direct function of the rotatory power of the sample, in particular of its concentration and optical path length[23]. In this chapter, we propose the determination of the optical activity of an optically active Bragg microcavity infiltrated with the liquid. To the best of our knowledge, this work constitutes a first example showing that the monitored changes in optical activity of a planar microcavity device can be used to determine the nature and other characteristic of a liquid or solutions. In **Chapter 3**, we have reported the fabrication of polarization active BMs and their optofluidic behavior under polarized light irradiation. Singular characteristics of these BMs of relevance for analytical purposes are the appearance of a different resonant peak for each polarization of light and the fluidic modulation of its optical activity. Relying on this behavior and on the optical interrogation technique proposed in **Chapter 3**, in the present chapter we will carry out a thorough and critical study of the different analytical possibilities of the BMs prepared by OAD, are they optically active or inactive.

4.2. Experimental and Methods

Chiral and *zig-zag* BMs were deposited on quartz plates of 1.25x2.50 cm and on silicon wafers for SEM analysis by electron beam evaporation in an oblique angle configuration. The photonic structures consist of a stack of 15 alternating TiO_2 and SiO_2 layers of approximately 85 nm, and a thicker central layer of SiO_2 of 200nm, acting as optical defect. The first layer was made of TiO_2 and the next of SiO_2 following this alternative stacking of high and low refractive index layer up to completing the whole stack. *Chiral* and *zig-zag* microstructures were prepared azimuthally turning the substrate for each layer, either 90^0 or 180^0, respectively (see **Figure 3.1 and 4.1**)

Optical analysis of the studied BMs upon the controlled infiltration of liquids was carried out in a homemade optofluidic device. As in previous chapters, a general assumption by these analyses is that the infiltrating liquid fills all the pore volume of the photonic structure. **Figure 2.1** shows a photo of one of the optofluidic device used for the analysis. This device permits an easy manipulation and infiltration of the BMs and their measurement in commercial spectrophotometers without further accessories. In these devices, the BMs were sandwiched with quartz plates and their borders sealed with PDMS. The quartz plates presented two holes with hypodermic needles acting as inlet and outlet pass of liquids. The design of the device left a clear surface of 1 cm^2 for the optical analysis and permits an easy control of orientation with respect to the plane polarization of light.

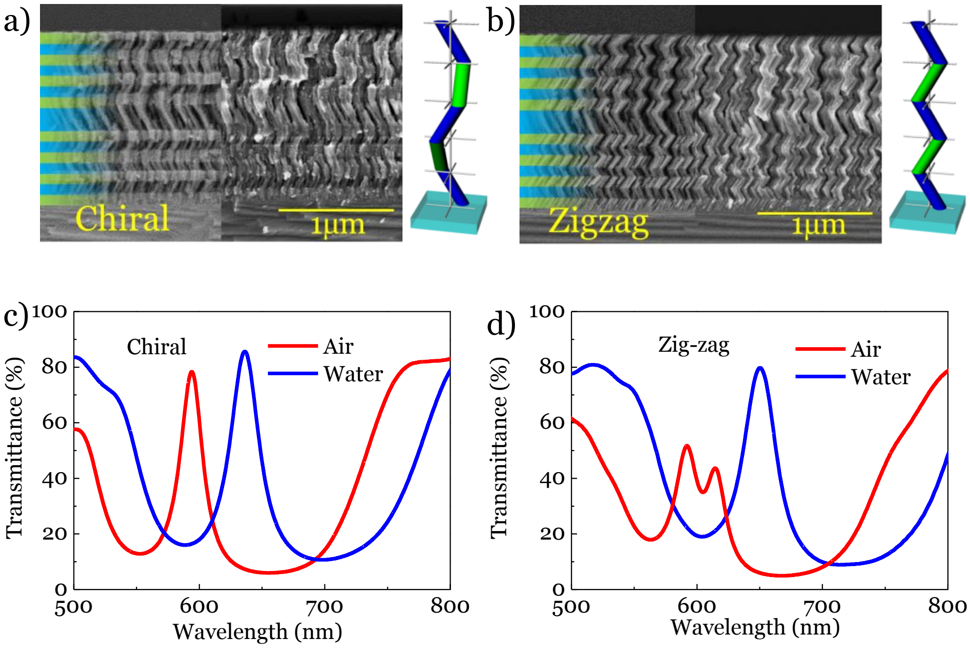

Figure 4.1. a) Cross-sectional SEM micrograph (BSE and SE) of a cleaved *chiral* BM. Overpainted a scheme of the 7 layer- optical defect- 7 layer BM stacking order. The schemes at the sideshow schemes of the ideal geometric arrangement of the nanocolumns in the individual layers. b) *Ditto* for a *zig-zag* BM. c) Optofluidic response of *chiral* BM when infiltrating with water under unpolarized light conditions. d) Ditto for a *zig-zag* BM.

Transmittance UV-Visible measurements were carried out in a Cary 100 spectrometer. Wide range linear polarizers and an azimuthal rotating holder were employed for the different experiments. The optical spectra of the *chiral* BM were obtained with unpolarized light whereas *zig-zag* BM optical spectra were measured by placing a linear polarizer before the sample, either at 0^0 or 90^0 with respect to the direction of the *fence-bundling* association in the film. The redshifted position of the resonant peak was carefully determined by a Gaussian fit. Changes in the optical activity were determined with two linear polarizers placed before and after the sample either in a crossed or an aligned configuration and oriented forming a 45^0 azimuthal angle with respect to them (see **Figure 3.5**). The optical spectra were recorded between 400 and 800 nm, i.e., encompassing the working range of the linear polarizers.

Cross-section analyses by scanning electron microscopy (SEM) of the BMs were carried out by cleaving the deposited silicon wafers. The SEM micrographs were obtained in a Hitachi S4800 field emission microscope working at 2 keV primary beam energy. The Secondary Electron (SE) and the

Back Scattered Electron (BSE) modes were used for topographic and compositional information respectively.

4.3. Results and Discussion

4.3.1. Optofluidic behavior of nanostructured Bragg Microcavities

The utilized BMs are characterized by a stacked pattern of successive layers of two oxides with different refractive indices, one low (L) and one high (H), and a thicker central layer acting as optical defect. The low refractive index layers and the optical defect have been made of SiO_2 and the high refractive index layers of TiO_2. **Figure 4.1** presents the microstructure of the *chiral* and *zig-zag* BMs. The Back Scattered Electron (BSE) SEM micrographs in **Figure 4.1 a)** and **b)** highlights the different composition of each layer through a brighter color to TiO_2 and a darker color to SiO_2 layers. Meanwhile, the secondary Electron (SE) SEM images evidence the characteristic columnar microstructure of OAD thin films, as well as its characteristic arrangement in the *chiral* and *zig-zag* configurations and a negligible *fence-bundling* association in the *chiral* BM and an enhanced association in the case of the *zig-zag* BM. **Figures 4.1 c)** and **d)** display the optofluidic behavior of porous BMs showing a redshift and an increase in transmittance when the BM are infiltrated with water. The transmittance spectrum of the *chiral* BM depicts the typical profile of a BM characterized by a narrow resonant peak in the middle of the band gap (**Figure 4.1 c)**). Unlike the *chiral* BM, the *zig-zag* BM presents two resonant peaks separated by 23 nm. This separation can be modulated by liquid infiltration, in which case the two peaks become closer and appear as a single broader and redshifted peak (**Figure 4.1 d)**). As it was explained in the previous chapter, an optical inspection with polarized light (**Figure 4.2**) reveals that this wide resonant peak recorded with un-polarized light is actually composed of two resonant peaks separated by 8 nm, each one appearing upon a different orientation of the sample with respect to the polarization axis of light (**Figure 4.2 b)**). We will show below that this azimuthal angle dependency can be used to increase the limit of detection of the *zig-zag* BM infiltrated with solutions.

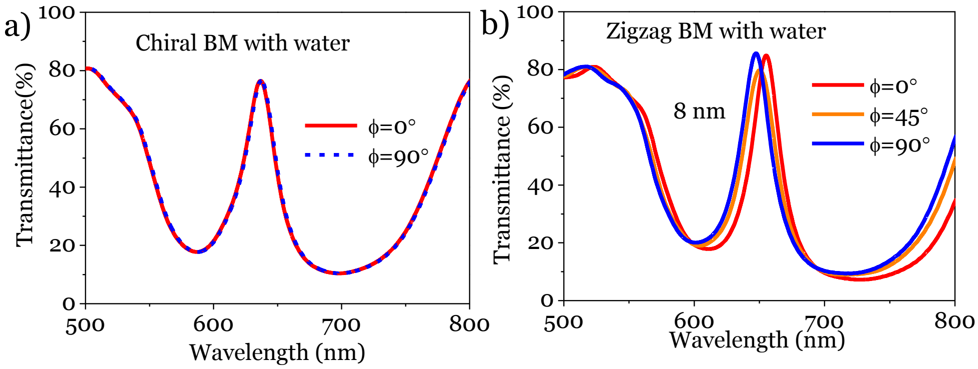

Figure 4.2. Polarization azimuthal dependence of BMs infiltrated with water. *Chiral* a) and *zig-zag* BM b) spectra around the resonant peak when recorded with linearly polarized light at the indicated angles (ϕ) formed between the polarization plane and the *bundling* direction (i.e., azimuthally rotating the sample by the indicated angles).

4.3.2. Liquid analysis by monitoring changes in the optical spectra of BMs.

In this section we will present two different analytical strategies used to determine the concentration of solutions using optically active and inactive BMs. The procedures rely on the determination of the position of the resonant peak and of the transmittance at a given wavelength.

a) Redshifts of BMs' resonant peaks.

The infiltration of the BMs with solutions containing an increasingly higher concentration of glucose produces a progressive redshift in the transmitted spectra which can be quantitatively monitored by following the resonant peak. **Figure 4.3** presents series of spectra recorded around this peak for two polarizations of light when the *zig-zag* BM is infiltrated with different solutions and for unpolarized light in the case of the *chiral* BM. These series of spectra corresponding to glucose concentrations comprised between 0.5 and 4.0mol/L (**Figures 4.3 a)**, **b)** and **c)**) clearly prove a direct correlation between the peak position and the concentration of the infiltrated solution. Lower concentrations from 0.1 to 0.5mol/L were explored as well, and the effects on the peak position are reported in **Figures 4.3 d)**, **e)** and **f)**.

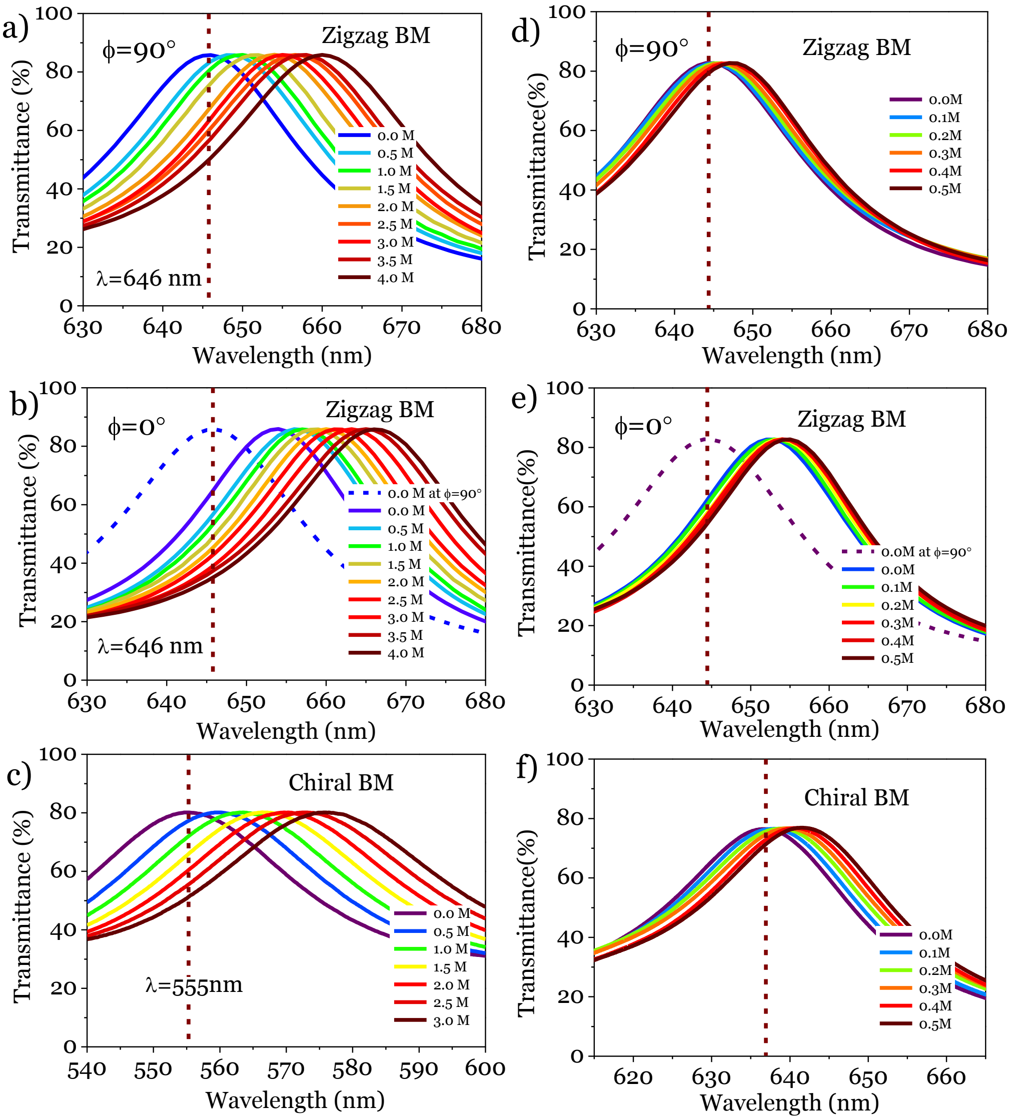

Figure 4.3. UV-vis transmission spectra recorded around the resonant peak for water and a series of glucose solutions infiltrating the *zig-zag* and *chiral* BMs taken, respectively, with polarized light at $\phi=90^0$ a) and $\phi=0^0$ b) and with unpolarized light c). The vertical dashed line in a) and b) indicates the resonant peak position with water at $\phi=90^0$ (λ=646nm). A self-calibration in intensity to prevent the effect of possible fluctuations of the lamp was carried out by taking as reference this peak. d), e) and f) ditto for lower concentrations.

Trying to quantify the dependence between resonant peak position and concentration of glucose solutions, **Figure 4.4** shows a series of plots where the $\Delta\lambda$ values between the positions of the resonant peak infiltrated with solutions and its position when filled with water is represented against the concentration of glucose in the investigated solutions. The two plots correspond to high (**Figure 4.4 a)**) and low (**Figure 4.4 b)**) ranges of concentrations. The two lines reported for the *zig-zag* microstructure correspond to values taken for ϕ= 90^0 and 0^0 but, in this latter case referring the Δλ values to the position of the reference resonant peak (i.e. for the BM infiltrated with water) taken at ϕ= 90^0 (i.e., dashed spectrum in **Figure 4.3 b)**). As expected, the two lines joining the points in **Figures 4.4 a)** and **b)** are rather parallel, although the slope is slightly higher for the ϕ= 90^0 representation. This difference becomes clearer at low concentrations as shown in **Figure 4b)**. We will see bellow that taking references at different polarization of light can be advantageous if data are referred to the percentage of transmittance rather than to the position of the maxima. Meanwhile, the set of data taken for the *chiral* BM also represented in **Figures 4.4 a)** and **4.4 b)** define a line with a slope that is steeper than that obtained for the *zig-zag* BM data points. This result clearly proves that the non-active BM presents the highest *sensitivity* for concentration analysis, at least when referring the concentrations to the position of the resonant peak. In general, these graphs demonstrate the reliability of the *chiral* and *zig-zag* BMs for the determination of concentrations by measuring the resonant peak position.

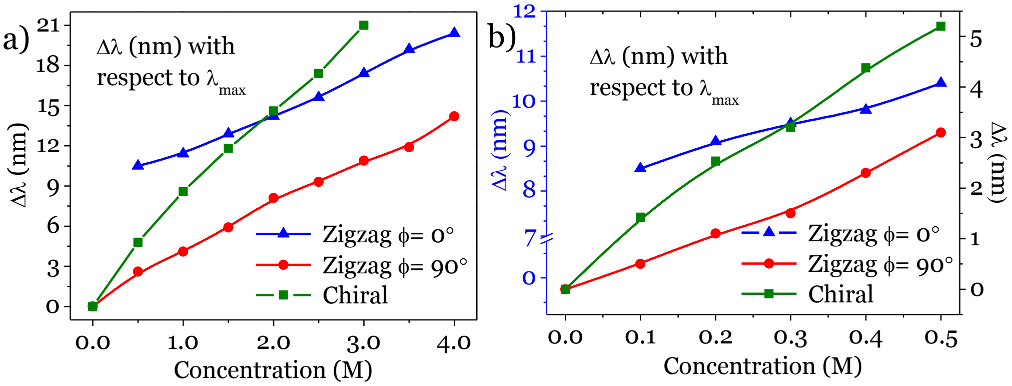

Figure 4.4. a) Plot of the shift in wavelength of the resonant peaks as a function of the glucose concentration for *zig-zag* and *chiral* BMs, including the two polarizations for the latter. Both are referenced to $\lambda_{max\varphi=90^o}$=646nm. b) Ditto for low concentrations of glucose. Blue axis corresponds to *zig-zag* BM ϕ=90^0.

From the known values of the refractive indices of glucose solutions[24], we have calculated the detection sensitivity Δλ/Δn in nm over refractive index units (RIU), a parameter which accounts for the sensitivity of the measurement system. The measurements with the *chiral* BM are characterized by a Δλ/Δn of

275 nm/RIU, while the *zig-zag* BM at pol 0^0 and 90^0 presents values of 119 and 137 nm/RIU, respectively.

b) Changes in transmittance at a selected wavelength.

The previous analysis requires a spectrophotometer to monitor the peak position after infiltration. This requirement could be avoided by following changes in intensity in the BMs at a given wavelength. Intensity detectors as photodiodes are cheaper, easier to handle and represent a simpler method of measurement. Moreover, single wavelength sources (e.g. a LED) tuned to the peak position of the BM resonant peak might be used for excitation, thus avoiding the need of any filter or spectrometer.

The measurement protocol, consisting of correlating changes in transmittance at a selected wavelength with the solution concentrations, uses as a reference the maximum transmittance of the resonance peak of the BM when it is infiltrated with water.

The direct measurement of the changes in transmittance for the *chiral* BM can be taken as a direct monitoring parameter of the concentration of the solutions. The results of a series of experiments using this methodology for different types of BMs are reported in **Figure 4.5**. It is also worth stressing that the optical activity of the *zig-zag* BM offers additional possibilities of analysis as illustrated in **Figure 4.5** where the resonance peak recorded at $\phi_{ref}= 90^0$ with water is used as a reference and the solutions are measured at $\phi= 0^0$. In fact, using the same polarization, i. e., $\phi= 90^0$, for both the reference (i.e. water) and problem solutions at low concentrations, renders little changes in intensity since the measurements are close to the maxima position in all cases (see **Figure 4.3 d)**, **e)** and **f)**). However, if the reference is measured at $\phi_{ref}= 90^0$ and the problem solutions at $\phi= 0^0$ it turns out that the variation degree of intensity vs concentration along the dashed line is quite high, as illustrated in **Figure 4.3** and **4.5 b)**. It is worthy of note that taken the water spectrum recorded at $\phi_{ref}= 90^0$ as a reference is quite straightforward because it only requires to rotate the device by 90^0. A similar argument holds for the back-rotation of the BM by 90^0 to measure the higher concentration solutions (from 1 mol/L on in our case) to recover higher *sensitivity*.

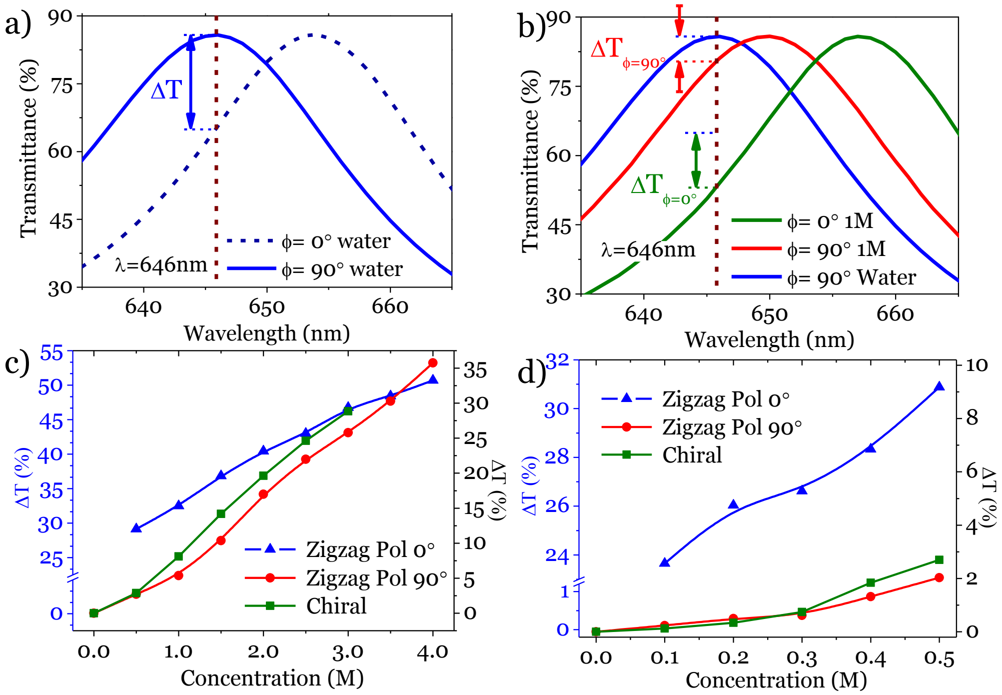

Figure 4.5. Transmittance spectra of *zig-zag* BM around the resonant peak at $\phi=0^0$ and $\phi=90^0$ infiltrated with water a) and with a solution of glucose 1M b). ΔT represents the difference in transmittance at a 646 nm (vertical line) with respect to $\phi=90^0$ infiltrated with water. c) Difference in transmittance as function of the glucose concentration according to the spectra reported in in fig 3 a), b) and c) for *chiral* and *zig-zag* BMs at $\phi=0^0$ and $\phi=90^0$. d) Ditto for lower concentrations (fig 3 d), e) and f)). The blue axis refers to *zig-zag* BM at $\phi=0^0$.

For the low and high concentration ranges, **Figure 4.5 c)** and **d)** show a summary of the obtained results obtained using the *chiral* and *zig-zag* BMs, in this latter case including curves obtained by referring the data to the water reference measured at $\phi_{ref}= 90^0$. Owing to the changes in intensity along the resonant peak profile, this plot clearly illustrates that the sensitivity of the measurement, defined by the slope of the calibration curves in this figure, is different depending on the range of concentrations, the type of BM and, for the *zig-zag* BM, for the polarization dependent position of reference peak utilized for the analysis (i.e., when filled with water and using $\phi_{ref}= 90^0$ or $\phi_{ref}= 0^0$). These *optimum ranges* of concentrations are: *chiral* BM from 0.5 to 2.5mol/L, *zig-zag* BM with $\phi_{ref}=0^0$ from 0 to 1 mol/L, and *zig-zag* BM with $\phi_{ref}=90^0$ from 1.5 to 2.5 and from 3.0mol/L.

Similarly to the Δλ method where we defined Δλ/Δn as sensitivity parameter, here we can define an equivalent ΔT/Δn sensitivity parameter. The obtained values in this case were 395 %/RIU from *chiral* BM and 369 and 272 %/RIU from *zig-zag* BM with $\phi_{ref}=90^0$ and at $\phi_{ref}=0^0$ respectively. Focusing in the aforementioned *optimum ranges* of concentration to maximize the performance, we obtained 440, 432 and 671 %/RIU as sensitivity parameters from *chiral* BM and *zig-zag* BMs at $\phi=90^0$ and at $\phi=0^0$. These results highlight the good performance of the *zig-zag* BM at $\phi=0^0$ for low concentrations using this polarization resolved approach of measurement.

4.3.3. Liquid analysis by monitoring changes in the optical activity of BM.

In **Chapter 3** we showed that incorporating a second polarizer after an optically active *zig-zag* BM provides an additional method for monitoring refractive indices of the liquids filling its pores. Herein, we propose to systematically use this approach to determine the concentration of problem solutions of glucose taken as example. It is obvious that *chiral* BMs must be excluded from this analysis due to their lack of optical activity.

Figure 3.5 showed a scheme of the experimental arrangement used for this experiment and **Figure 4.6** presents a series of spectra recorded for the cross and parallel configurations of the polarizers for three glucose solutions of increasingly higher concentrations. Clearly, besides an equivalent redshift recorded for the two configurations, the intensity of the spectra recorded for the parallel configuration increases with the glucose concentration, while it decreases when the spectra are recorded for the cross configuration. This tendency agrees with the behavior previously reported in **Chapter 3** of this type of BM infiltrated with pure liquids of increasing refractive indices.

We propose that the intensity ratio between the spectra recorded with the cross and parallel configurations can be taken as a measurement of the glucose concentration in the solution. For high concentration solutions, the calibration curve reported in **Figure 4.6 c)** yields a practically linear dependence of this parameter on the glucose concentration. Meanwhile, the results in **Figure 4.6 d)** corresponding to low concentrations glucose solutions suggest a limit of detection using this methodology of 0.1mol/L. On the other hand the sensitivity parameter Δβ/Δn obtained in this case was 147 RIU^{-1}.

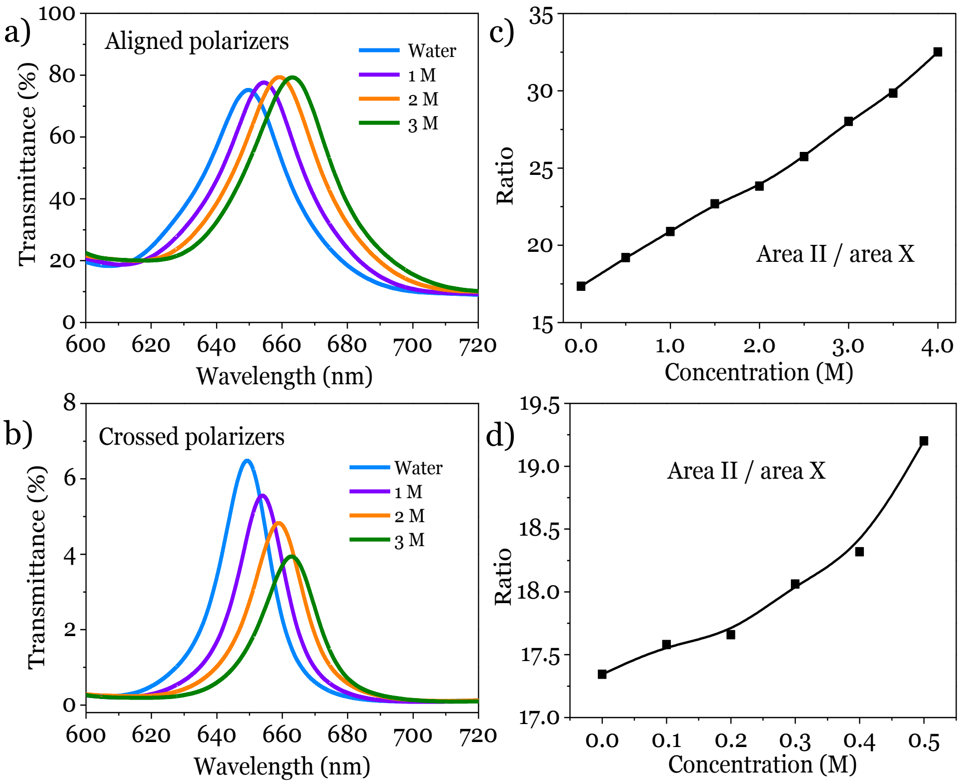

Figure 4.6. a) & b) Transmittance spectra of *zig-zag* BM recorded around the resonant peak infiltrated with water and several solutions of glucose. The sample was rotated at phi=45° and placed in-between two aligned (a)) and crossed (b)) polarizers. c) Ratio between the areas of the resonant peaks recorded in aligned and crossed configuration as a function of glucose concentration. d) Ditto for lower concentrations of glucose.

It is worth noting that-this polarization-ratio procedure avoids experimental problems stemming from malfunctions or time instabilities of the light source or other drifts and instabilities of the measurement system because the ratio between signals is independent of the illumination intensity[25].

4.4. Conclusions

Porous planar BMs have been successfully deposited by OAD using an electron-beam evaporator. By azimuthally rotating the substrate for each layer, BMs with *zig-zag* and *chiral* microstructures have been grown leading to polarization active and non-active BM, respectively. These BM have been successfully implemented in an optofluidic device to allow the infiltration and the posterior optical testing of liquids for analytical purposes . Taking advantage of the optofluidic behavior of BMs and their optical spectra, three measurement methods have been proposed for determining the concentration of glucose solutions. The redshift of the spectra have been analyzed by measuring both, the shift of the resonant peak and the variations in intensity at a selected wavelength. An optimum range of concentrations has been proposed for each configuration. The variation of the optical activity with the refractive index of the infiltrating liquid in the zig-zag BM has been also found to depict a suitable behavior for liquid analysis.

The low volume of liquid required for the infiltration of the porous BMs makes easy their implementation into complex microfluidic systems. The *chiral* and the *zig-zag* BM could provide a simple and reliable analysis offering two possible performances for measuring the former and two the latter.

4.5. References

1. Photonic Crystals: Principles and Applications. *CRC Press* at <https://www.crcpress.com/Photonic-Crystals-Principles-and-Applications/Gong-Hu/9789814267304>
2. Snow, P. A., Squire, E. K., Russell, P. S. J. & Canham, L. T. Vapor sensing using the optical properties of porous silicon Bragg mirrors. *J. Appl. Phys.* **86,** 1781–1784 (1999).
3. Zangooie, S., Jansson, R. & Arwin, H. Reversible and irreversible control of optical properties of porous silicon superlattices by thermal oxidation, vapor adsorption, and liquid penetration. *J. Vac. Sci. Technol. A* **16,** 2901–2912 (1998).
4. Kurt, H. & Citrin, D. S. Photonic crystals for biochemical sensing in the terahertz region. *Appl. Phys. Lett.* **87,** 041108 (2005).
5. Potyrailo, R. A., Hobbs, S. E. & Hieftje, G. M. Optical waveguide sensors in analytical chemistry: today's instrumentation, applications and trends for future development. *Fresenius J. Anal. Chem.* **362,** 349–373 (1998).
6. Nishijima, Y. *et al.* Inverse silica opal photonic crystals for optical sensing applications. *Opt. Express* **15,** 12979–12988 (2007).
7. Dorfner, D. F. *et al.* Silicon photonic crystal nanostructures for refractive index sensing. *Appl. Phys. Lett.* **93,** 181103 (2008).
8. Lončar, M., Scherer, A. & Qiu, Y. Photonic crystal laser sources for chemical detection. *Appl. Phys. Lett.* **82,** 4648–4650 (2003).
9. Hasek, T., Kurt, H., Citrin, D. S. & Koch, M. Photonic crystals for fluid sensing in the subterahertz range. *Appl. Phys. Lett.* **89,** 173508 (2006).

10. Falco, A. D., O'Faolain, L. & Krauss, T. F. Chemical sensing in slotted photonic crystal heterostructure cavities. *Appl. Phys. Lett.* **94,** 063503 (2009).
11. Casquel, R. *et al.* Sub-micrometric reflectometry for localized label-free biosensing. *Opt. Express* **23,** 12544 (2015).
12. González-García, L., Lozano, G., Barranco, A., Míguez, H. & González-Elipe, A. R. TiO2–SiO2 one-dimensional photonic crystals of controlled porosity by glancing angle physical vapour deposition. *J. Mater. Chem.* **20,** 6408–6412 (2010).
13. Gao, J., Gao, T. & Sailor, M. J. Porous-silicon vapor sensor based on laser interferometry. *Appl. Phys. Lett.* **77,** 901–903 (2000).
14. Barranco, A., Borras, A., Gonzalez-Elipe, A. R. & Palmero, A. Perspectives on oblique angle deposition of thin films: From fundamentals to devices. *Prog. Mater. Sci.* **76,** 59–153 (2016).
15. Kaminska, K. & Robbie, K. Birefringent Omnidirectional Reflector. *Appl. Opt.* **43,** 1570 (2004).
16. Steele, J. J., van Popta, A. C., Hawkeye, M. M., Sit, J. C. & Brett, M. J. Nanostructured gradient index optical filter for high-speed humidity sensing. *Sens. Actuators B Chem.* **120,** 213–219 (2006).
17. Hawkeye, M. M. & Brett, M. J. Photonic bandgap properties of nanostructured materials fabricated with glancing angle deposition. in **6832,** 683204–683204–10 (2007).
18. Schubert, M. F., Xi, J.-Q., Kim, J. K. & Schubert, E. F. Distributed Bragg reflector consisting of high- and low-refractive-index thin film layers made of the same material. *Appl. Phys. Lett.* **90,** 141115 (2007).
19. Schubert, M. F., Kim, J. K., Chhajed, S. & Schubert, E. F. Conductive distributed Bragg reflector fabricated by oblique angle deposition from a single material</title> in (ed. Ellison, M. J.) 667403–667403–7 (2007). doi:10.1117/12.731266
20. Oliva-Ramirez, M. *et al.* Liquids Analysis with Optofluidic Bragg Microcavities. *ACS Appl. Mater. Interfaces* **5,** 6743–6750 (2013).
21. Singh, D. P., Lee, S. H., Choi, I. Y. & Kim, J. K. Spatially graded TiO_2-SiO_2 Bragg reflector with rainbow-colored photonic band gap. *Opt. Express* **23,** 17568 (2015).
22. Yunus, W. M. bin M. & Rahman, A. bin A. Refractive index of solutions at high concentrations. *Appl. Opt.* **27,** 3341 (1988).
23. Li, Y., Xiong, G., Yu, G., Jiang, Z. & Wang, F. <title>Investigation of optical fibre sensor for remote measuring optical activity</title> in (eds. Culshaw, B. & Liao, Y.) 382–385 (1991). doi:10.1117/12.50008

24. Lide, D. R. *CRC Handbook of Chemistry and Physics, Internet Version.* **4,** (CRC Press, Boca Raton, FL, 2005).
25. Clerc, D. & Lukosz, W. Direct immunosensing with an integrated-optical output grating coupler. *Sens. Actuators B Chem.* **40,** 53–58 (1997).

Chapter 5

Anomalous Giant Absorption of Dye solutions infiltrated in Planar Bragg Microcavities

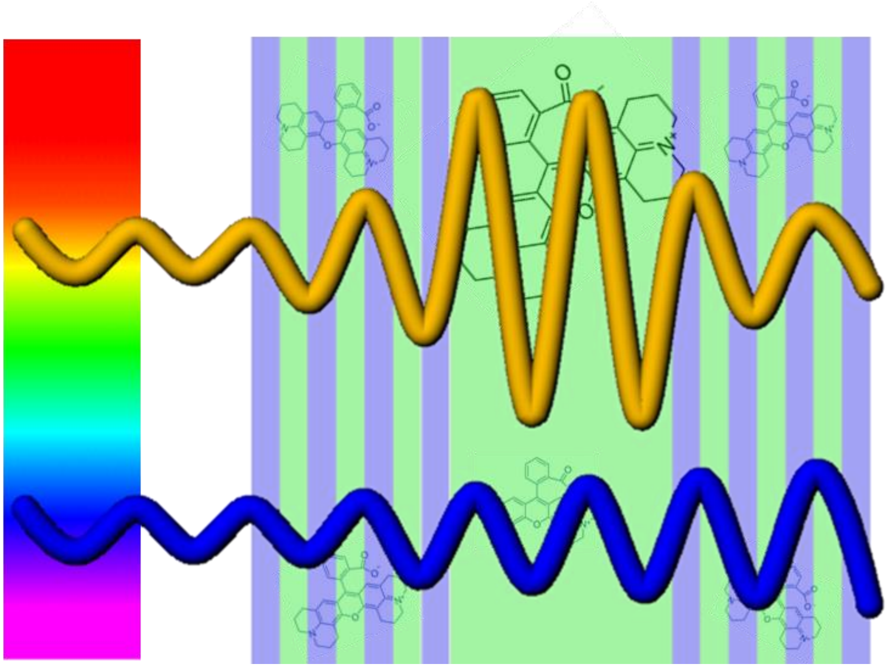

5.1. Introduction

The previous chapters in this thesis have shown that planar Bragg microcavities (BM) formed by the stacking of porous layers of two oxide materials of different refractive indices are useful transducers for liquid monitoring. In all investigated examples presented along this thesis, the liquids were colorless and the basic principle of detection consisted of monitoring the variation in refractive index of the liquid or solution. In this chapter we investigate the effect of infiltrating the BM device with colored liquids characterized by a high absorption band coefficient. This investigation is primarily intended to prove the effect of highly absorbent liquids on the optofluidic behavior of the BMs. However, in the course of the performed experiments with dye solutions we have been able to show the appearance of new resonant effects involving both the photonic structure and the highly absorbent solutions. In concrete, the observed effects have been accounted for by an apparent enhancement of the absorption coefficient of the dye solutions. This enhanced absorption has been monitored following an anomalous redshift in the position of a given resonant peak of a BM incorporating a large defect. A careful simulation analysis using WVASE and FilmStar Optical Thin Film software packages has permitted a straightforward interpretation of the observed effects and, therefore, to pave the way for the application of the detected decoupling principle for different purposes. In particular, we believe that the implications of the experiments presented in this work are of relevance to explain the enhancement in photon yield observed in photovoltaic cells incorporating a Bragg resonator[1–3], for optofluidic sensing applications[4–8] or to explain other photoluminescence mediated processes in BMs[9–13].

5.2. Experimental and Methods

5.2.1. Materials and characterization and analysis procedures.

Uniform, mechanically stable, and highly porous BMs made of alternated layers of TiO_2 and SiO_2 have been prepared by oblique angle deposition (OAD) according to the procedure reported before[14]. A first set of porous BMs with a *zig-zag* microstructure were e-beam evaporated on glass plates of 1.5 × 2.5 cm^2 at a zenithal angle of 60° by rotating the substrate 180^0 from one layer to the next as we showed in **Chapter 3**. During the deposition, the substrates were placed at 70 cm from the evaporation source. For electron microscopy characterization, samples were simultaneously deposited on a silicon wafer. Another set of similar BMs with *slanted* microstructure and a controlled lateral variation of thickness where prepared at a zenithal angle of 60^0. Control over the lateral variation of thickness in a range from 2480nm to 2753nm (~11% of gradient thickness) was achieved by placing a larger substrate (1.5x 3.5 cm^2) at a shorter distance of ca. 30 cm from the evaporation source. For some specific experiments carried out for comparison, SiO_2 and TiO_2 single layers were prepared as described for the *zig-zag* BM but using just a single source of material for evaporation.

Cross section scanning electron microscopy (SEM) images in Secondary Electrons (SE) and Back-Scattered Electrons (BSE) mode were obtained in a Hitachi S4800 field emission microscope for samples deposited on a silicon wafer that were cleaved for cross-section analysis.

UV–vis transmission spectra of the Rh101 and RhB solutions in ethanol were recorded using linearly polarized light in normal incidence and at different impinging angles with a Varian Cary 100 instrument. UV-vis reflectance spectra were also recorded in normal incidence by means of a set-up consisting of optical fibers with a micrometric sliding holder in an Ocean Optics QE65000 Spectrometer. Although the polarization activity depicted by the *zig-zag* and the *slanted* BMs (**Chapter 3**) will not be discussed any further along this chapter, it is worth mentioning that to increase the resolution (see section 3.3.2.) all data acquired either in transmission or reflectance modes were recorded with linearly polarized light along the direction perpendicular to the *fence-bundling* association.

For the optofluidic essays, the BMs deposited on a glass plate were implemented in two different microfluidic devices. According to **Figure 5.1**, a first device type incorporates this covered plate sandwiched with another glass plate as explained in **Chapter 2** (device *type 1*), while in a second one these active plates were incorporated in a homemade micro-cuvette of 125μm of path length (device *type 2*). These simple microfluidic arrangements enabled handling the device as a plate substrate in front of the light beam of a spectrometer and to record spectra while replacing the circulating liquid by simple injection. Measurements were carried out in transmission (devices *type 1* and *type 2*) and reflection (device *type 2*) modes. This latter procedure (light incidence on the backside of the plate where the BM was deposited) ensures that only the volume comprised within the BM thickness is monitored during the analysis.

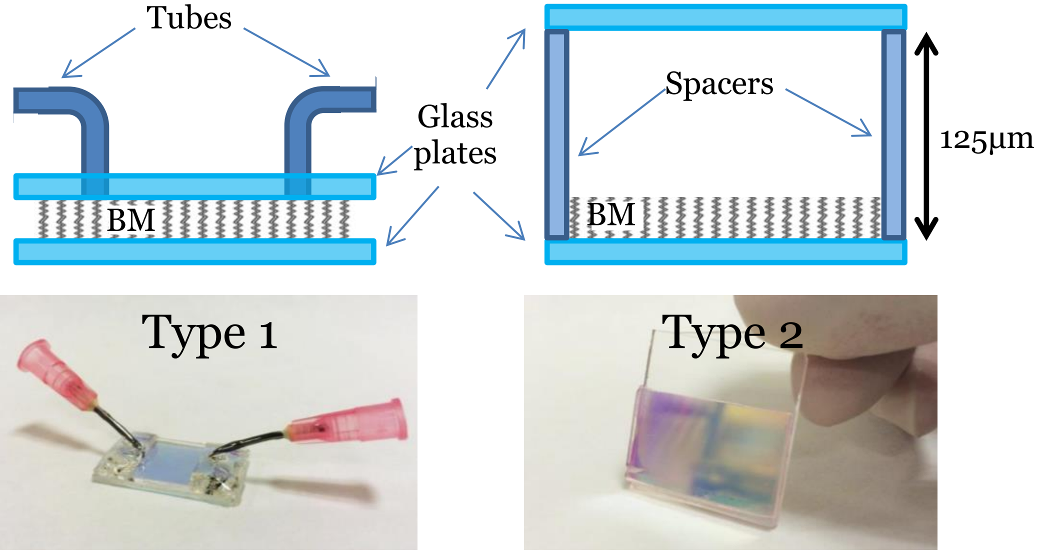

Figure 5.1. Schemes and photographs of the microfluidic devices, type 1 and 2, integrating BMs (dimensions are not at real scales).

5.2.2. Simulation analysis

To simulate the reflectance and transmittance spectra we have used the same optical description of the BM used in **Chapter 3** using WVASE software to account for the multilayer structure and optical anisotropy. The optical description of the absorbing solution was mathematically described with the parameterized GENOSC.MAT type material description that self-consistently couple the corresponding refractive index and extinction coefficient by Kramers-Kronig relations. Thus, ethanol solutions were described with a Cauchy dispersion corresponding to the pure ethanol plus the addition of gaussian-lorential absorption bands, obtained as a result of fitting experimental transmission of reflection measurements.

The evaluation of the electric field strength vs device thickness was done using FilmStar Optical Thin Film software [http://www.ftgsoftware.com/]. The inputs for this calculation were the optical (refractive index and extinction coefficient of the layers in the BM device) and topology (multilayer structure) descriptions obtained after measuring the SEM images and measured the reflectance and transmittance spectra with WVASE.

5.3. Results

5.3.1. Liquid infiltration of Bragg microcavities with two or more resonant peaks.

Bragg microcavities (BMs) similar to those utilized in **Chapters 3** and **4** but with a relatively thicker middle layer acting as optical defect have been utilized in this study. An example of such a microstructure is presented in **Figure 5.2a)** and **b)** showing the cross section of BMs formed by 7 bottom stacked TiO_2 and SiO_2 layers in the form of a 1D photonic crystal, an intermediate thick layer of SiO_2 and a top 1D photonic crystal equivalent to that in the bottom part. In **Figure 5.2a)**, the whole layer structure was prepared in a *zig-zag* configuration whereby the substrate was rotated by 180^0 when changing from one layer to the next during the evaporation sequence. In the case of the SiO_2 intermediate layer, with an approximate total thickness of 1000 nm, the substrate was rotated after 250 nm evaporation to reduce possible scattering effects associated to the nanocolumn width increase commonly observed for *slanted* configurations[15]. **Figure 5.2b)** presents a *slanted* BM with the same thicknesses than the *zig-zag* but grown at a shorter distance from the evaporation source in order to increase the lateral inhomogeneity in thickness in the direction perpendicular to the fence-bundling association[16]. As previously discussed in **Chapter 3**, an additional consequence of either the *zig-zag* or *slanted* configurations is that the photonic structure becomes birefringent, i.e., it presents double resonant peaks each one for a given perpendicular polarization. The transmission spectra of the *zig-zag* BM recorded with 0^0 and 90^0 linearly polarized light with respect to the *fence-bundling* direction in the layer are presented in **Figure 5.2c)**. These two spectra are characterized by two resonant peaks located within the typical transmission gap of these structures. The appearance of these two resonant peaks is due to the large defect thickness in this BM structure, while the polarization dependent shifts by 14 and 19 nm in the position of, respectively, the first and second resonant peak confirm the birefringent character of this BM (i.e., due higher refractive index in the fence-bundling direction than in their normal at the device surface, see **Chapter 3**). In a similar way that for the one-peak BM reported in previous chapters, **Figure 5.2d)** shows that the infiltration of this photonic structure with liquids produces a redshift of the spectrum and a substantial decrease in the difference between the positions of the resonant peaks recorded with 0^0 and 90^0 polarizations which, according to this figure, only shifted by 2.6 and 4.6 nm when the BM was infiltrated with ethanol. It is also worth noting in this figure the appearance after infiltration of a third resonant peak at around 566nm (marked with **P_1** in the spectra) that previously was concealed by the oscillations occurring outside the optical gap zone).

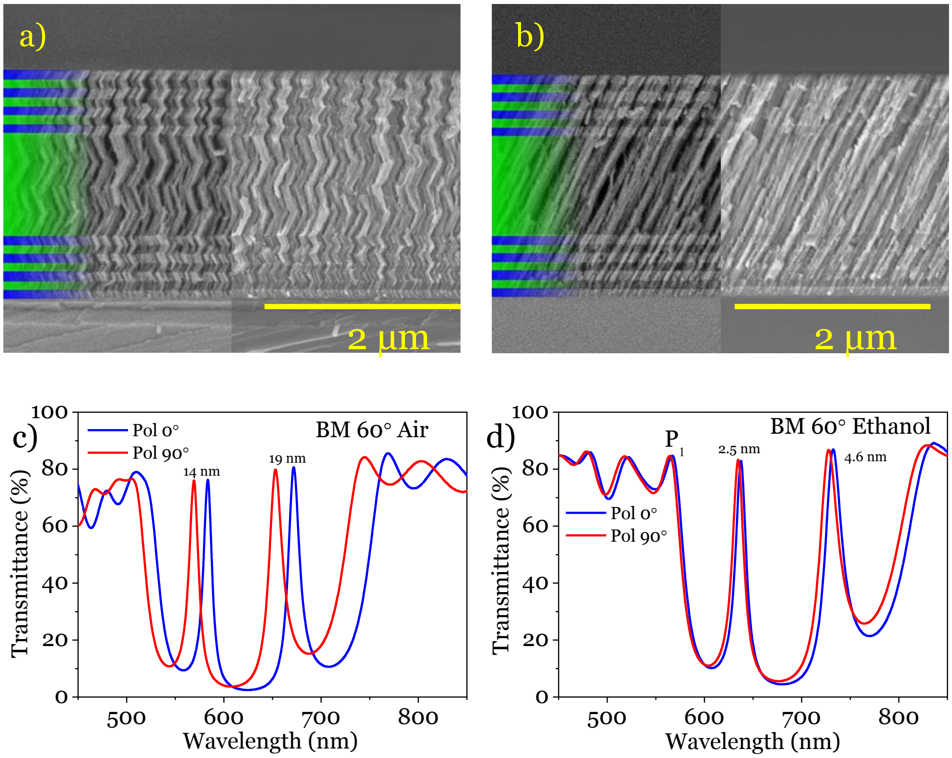

Figure 5.2. a) & b) BSE and SE cross section SEM micrographs of the *zig-zag* and the *slanted* large defect BMs respectively. The coloring at the left hand side of the image highlights the stacked TiO_2 (blue) and SiO_2 (green) layer structure. c) UV-vis transmission spectra of a *zig-zag* BM recorded with 0^0 and 90^0 linearly polarized light. d) Idem after infiltration of this porous BM with ethanol.

The spectra in **Figure 5.3a)** show that after infiltration with liquids of different refractive indices there is a progressive shift in the position of the three resonant peaks as expected from previous chapters. A careful evaluation of the positions of the three resonant peaks (called **P_1**, **P_2** and **P_3** in **Figure 5.3b)**) shows that the differences in their positions (i.e. $\Delta P_i = P_i(\lambda_{liquid}) - P_i(\lambda_{water})$) as a function of the refractive index of the infiltrating liquid follow similar increasing and parallel trends. According to WVASE simulations of the porous BM it is expected a linear shift of the resonant peak position with the refractive index of the infiltrated liquid. This behavior is similar to that reported in **Chapter 2** for one peak BMs.

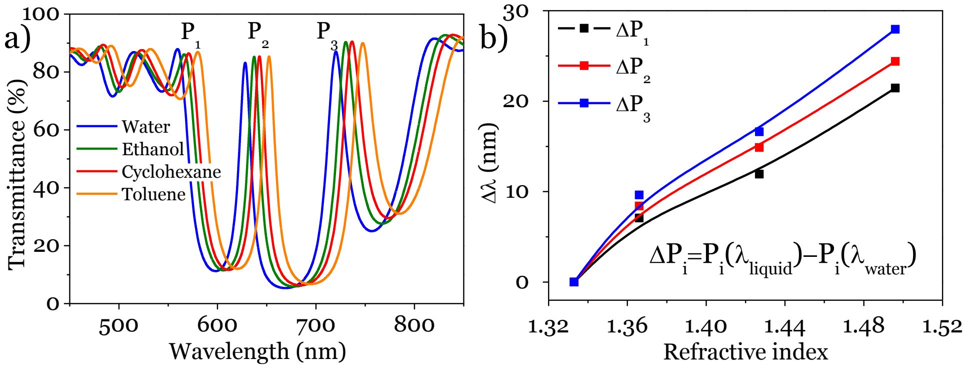

Figure 5.3. a) UV-vis transmission spectra recorded with linearly polarized light of the zig-zag large defect BM infiltrated with liquids of different refractive indices. b) Plot of the resonant peaks shifts as a function of the refractive index of the liquid infiltrating the pores of the structure.

a) BM infiltrated with dye solutions

In **Chapters 2** and **4** we showed that the change in refractive index of liquid solutions when increasing the solute concentration produces a progressive shift in the resonant peak positions that can be used to determine the solute concentration. These experiments were carried out with nonabsorbent liquids characterized by a smooth variation of refractive index with the wavelength (i.e. presenting a slight or no chromatic dispersion). In highly absorbent liquids or solutions, larger changes are expected in the refractive index associated with the presence of intense and narrow absorption bands[17]. **Figure 5.4.a)** shows the absorption coefficient (**$\alpha(\lambda)$**) spectra for increasing concentrations of Rh101 in ethanol solutions (full lines) and the corresponding refractive index (**$n(\lambda)$** in dashed lines). It is apparent that for increasing concentrations of dye there is increasing variation in the refractive index of the solutions around the absorption zone. Thus for 10^{-3}M Rh101 in ethanol (maximum absorption coefficient of ~0.03 μm^{-1}), **$n(\lambda)$** varies around the position of the absorption band ~0.002 units . In **Figure 5.4.b**) we also present the absorption coefficient and refractive index functions (dashed lines) calculated in **Section 5.3.1.b)** for the same dye solutions infiltrated in the BM. Note the difference in scales for both the refractive index variation and the absorption coefficient. These curves will be discussed later in this chapter.

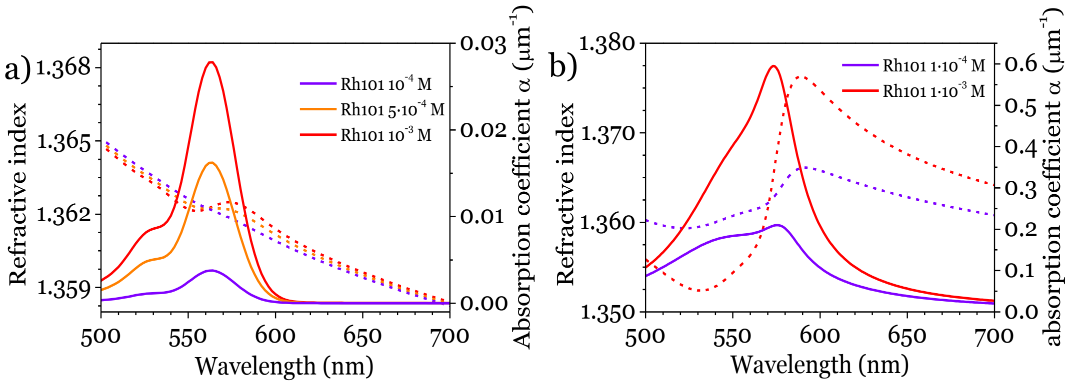

Figure 5.4. a) Refractive index (dashed lines) and absorption coefficient (full lines) spectra of several concentrations of Rh101 in ethanol solutions recorded in a 125 micron path length cuvette shown in Figure 5.8 d). b) Similar than a) but with the solutions infiltrated in the BM. The curves were determined by fitting analysis of the angle dependent transmission spectra of the BM infiltrated with 10^{-4}, $5{\cdot}10^{-4}$ and 10^{-3} M Rh101 solutions shown in Figures 5.8a, 5.8b and 5.9 (see also sections 5.3.1. b) in text).

Henceforth, we describe a set of experiments showing the optical response of the infiltrated BM with dye solutions.

Figure 5.5 presents a series of spectra recorded in reflection mode (device type 2) for increasing concentrations of RhB in ethanol up to 10^{-1} M. The spectra reported in **Figure 5.5 a)** clearly show a progressive variation in the resonant peak positions. This shift is almost the same for **P_2** and **P_3** (**Figure 5.5d)**) but larger for **P_1**, precisely the resonant peak closer to the absorption band of the dye as observed in **Figure 5.5b)** for the spectra recorded with the BM and in **Figure 5.5c)** for the transmission spectra directly recorded for the dye solution. This decoupling of the resonant peak position **P_1** points to a modification of resonant effects in the BM under the influence of the dye absorption band. Simulation of the spectra according to the premises presented in the experimental section (**Figure 5.6**) effectively confirms that this decoupling of the **P_1** position is linked with its proximity to the absorption band of the RhB solutions and to the high variation of the refractive index in this zone, a deviation that has already dumped at **P_2** and **P_3** wavelengths.

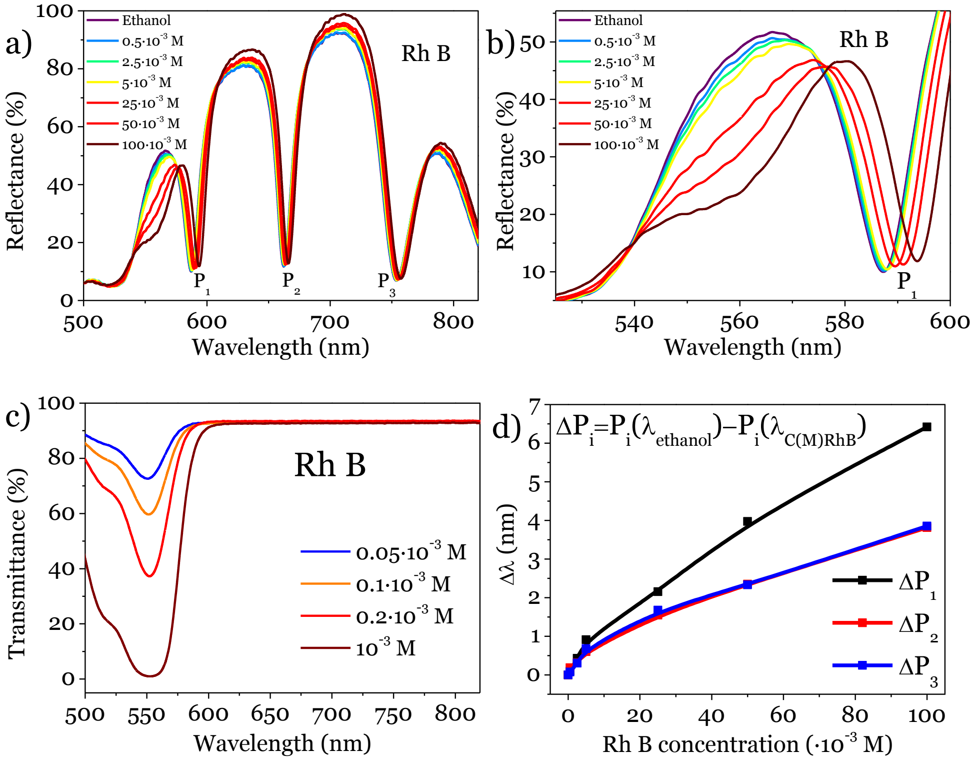

Figure 5.5. a) UV-vis Reflectance spectra of the large BM infiltrated with increasingly higher concentrations of RhB in ethanol. b) Detail of the spectra in an enlarged scale around **P_1**. c) UV-vis transmission spectra of the RhB solutions. d) Variations in the resonant peak positions as a function of the dye concentration in the solutions.

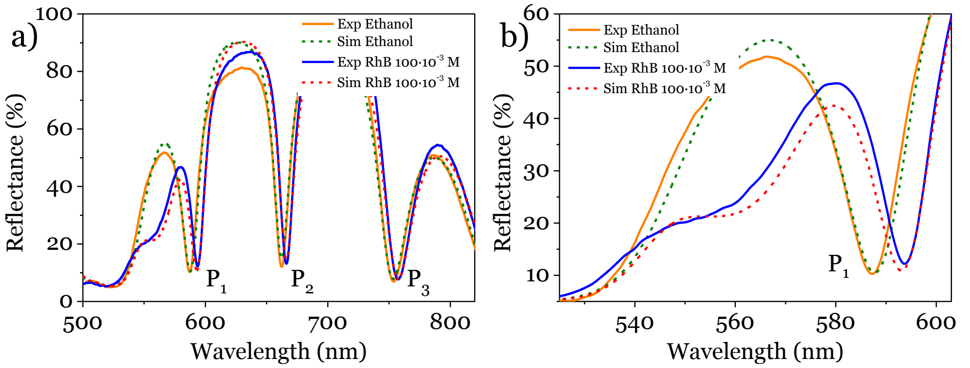

Figure 5.6. Comparison between experimental (full lines) and simulated (dashed lines) reflectance of the BM infiltrated with ethanol and with 10^{-1} M solutions of RhB in this solvent.

To have additional insights of this modulation effect, experiments have been carried out making that the resonant peak position crosses the dye absorption band (and therefore the wavelength zone characterized by a sharp variation of the refractive index (**Figure 5.8)**)).

b) Monitoring anomalous BM resonant peak shifts by polar rotation

These experiments were carried out in transmission mode using the *device 1* and measuring the transmission spectra in an UV-vis spectrometer while turning the device with respect to its polar axis. A well-known behavior of BMs when examined by impinging the light at directions other than normal to the surface is a progressive shift to lower wavelengths (blueshift) in the position of the resonant peaks with the impinging angle (**Figure 2.6**). For the examined BM infiltrated with ethanol, the observed angle dependence of the resonant peaks positions is presented in **Figure 5.7**. This figure also shows that this shift has a different magnitude for **P$_1$** and **P$_2$** vs polar rotation angle and that, therefore, the difference between them experiences a progressive decrease with the analysis angle.

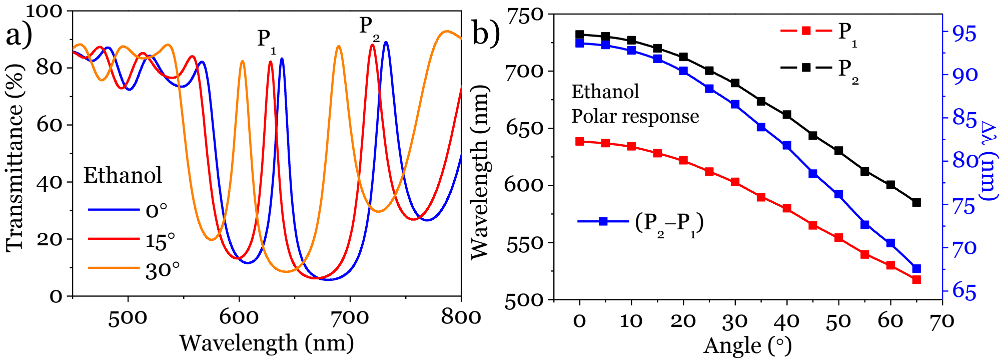

Figure 5.7. a) UV-vis transmission spectra of the large BM infiltrated with ethanol recorded off-normal at increasing polar angles. b) Plot of peak position **P$_1$**, **P$_2$** and the difference (**P$_1$**- **P$_2$**) as a function of polar angle.

This experiment was repeated with Rh101 ethanol solutions and the results reported in **Figure 5.8** for solutions of Rh101 of 10^{-4}, $5{\cdot}10^{-4}$ and 10^{-3} M concentrations. A first effect observed in this series of spectra is a progressive decrease with the dye concentration in the intensity of the first resonant peak (**Figures 5.8a)** and **5.8b)**). In addition, turning the device produces a progressive blueshift in the position of the two resonant peaks that, for **P$_2$**, follows the already described behavior found with pure ethanol. By contrast,

P_1 experiences an anomalous shift that can be easily monitored by representing the value **P_2-P_1**. According to **Figure 5.8c)** the position of this peak is highly dependent on the concentration of the dye molecule and depicts an oscillatory dependence with the tilting angle. Particularly for the most concentrated solution, but also visible for the two others concentrations, the difference **P_2-P_1** oscillates in the wavelength region of the dye absorption band (c.f. **Figure 5.4a)**). It is remarkable that the shape variation of this difference at the absorption band resembles that of the refractive index of the Rh101 solutions reported in **Figure 5.4b)** and that the intensity of the variations depends on the concentration of dye in the ethanol solution. A first application of this anomalous behavior is to determine the concentration of dye solutions by just correlating its value to the magnitude of the maximum change in **ΔP_1**.

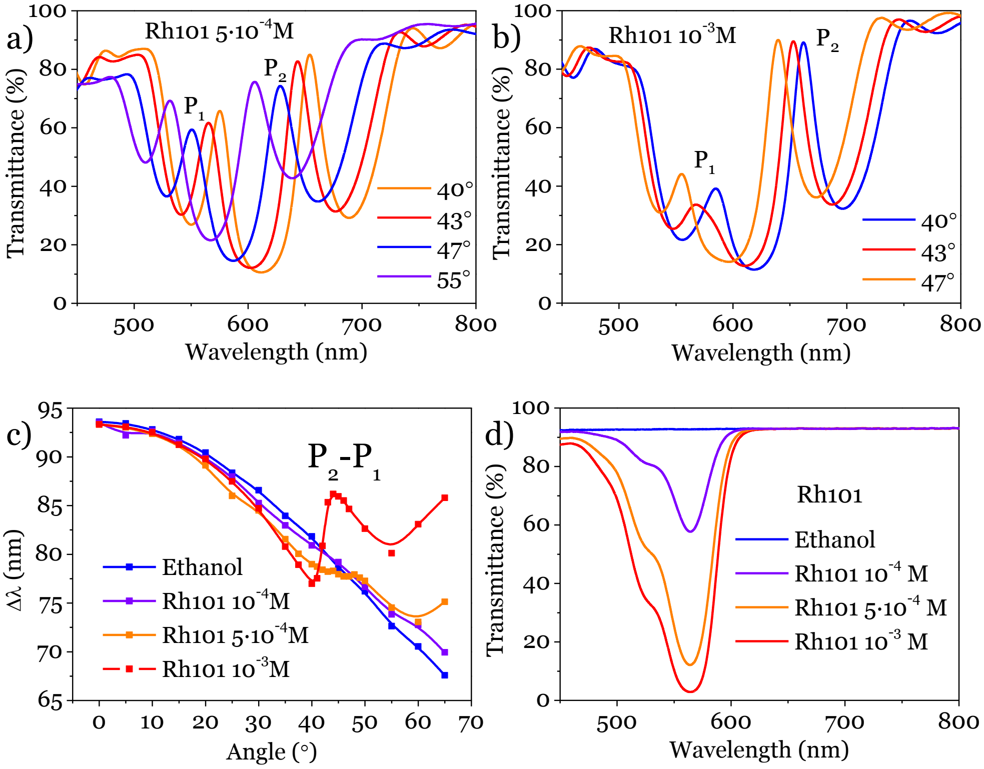

Figure 5.8. a) & b) Series transmission spectra recorded for the large BM infiltrated with increasingly higher concentration Rh101 in ethanol ($5 \cdot 10^{-4}$ and 10^{-3} M) for the indicated impinging angles of the light beam . c) Plot of **P_2-P_1** for the different studied solutions. d) Transmission spectra of the analyzed Rh101 solutions.

Both the intensity evolution of the resonant peak and the position of the maximum as a function of the analysis angle could be reproduced by simulation under the assumptions of a classical interference model that incorporates the effect of the dye absorption (see methods **Section 5.2.2** for clarification). The results of this simulation are represented in **Figure 5.9** showing a pretty good match between experimental and simulated spectra.

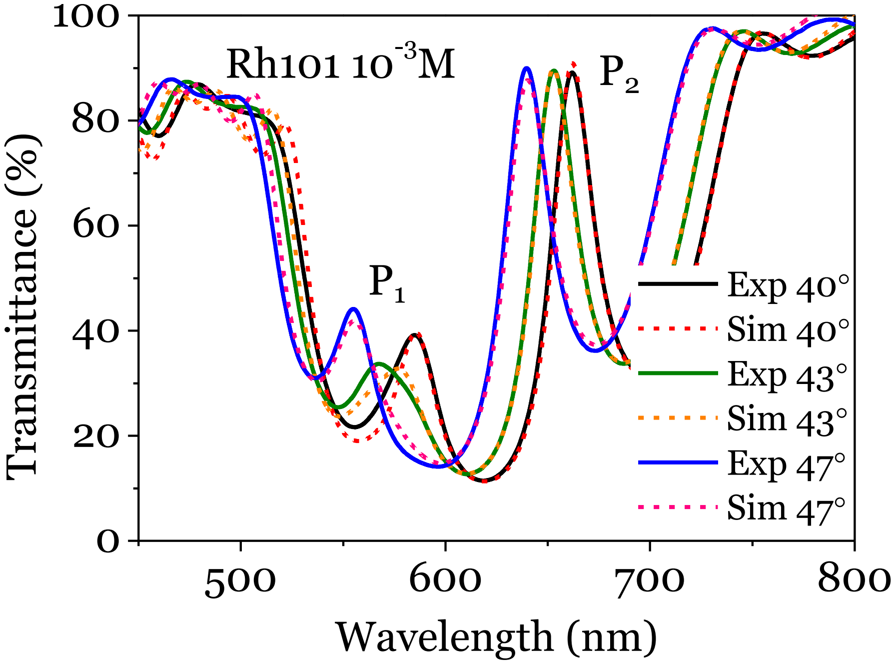

Figure 5.9. Experimental and simulated UV-vis spectra for different impinging angles of light for the large BM infiltrated with 10^{-3} M Rh101 solution in ethanol.

This good fitting requires as inputs the wavelength dependent apparent absorption and refractive index functions of the solutions filling the pores of the BM, these latter plotted in **Figure 5.4.b)**, which are clearly more intense than the absorption and refractive index curves of the solutions directly measured by transmission in the 125 μm path length cuvette. We tentatively attribute this effect to the confinement enhancement of electrical field well-known in Bragg reflectors and BMs[1,3,18] when used to increase the photon yield in photovoltaic cells[2,19] or in other photoluminescence applications[20–22]. In our case, the anomalous shift in **P_1** is due to anomalous wavelength dispersion in the refractive index because of the presence of a localized enhanced absorption in the BM. This effect could be mathematically described as an enhanced absorption coefficient (as shown **Figure 5.4a)**), that stems from the concentration of the electric field in the BM at the wavelengths around the resonant peak. This point will be the subject of a dedicated discussion in **Section 5.4**.

In the case of the absorption curve there is also a certain broadening and a small shift in the position of the maximum of the absorption band to larger wavelengths (that we attribute to the higher effective refractive index of the surrounding medium SiO_2/TiO_2/Ethanol).

c) *Monitoring giant dye absorption in BMs with variable thickness*

To further analyze the influence of the dye in the BM spectra we have used a thickness gradient device where the position of the resonant peaks progressively shifts when laterally moving the sample. For this purpose we have prepared an inhomogeneous BM structure for a zenithal deposition angle of 60^0 that we integrated in a device *type 2* (see **Figure5.1b)**). This system was systematically investigated both in transmission and in reflection modes, this latter to minimize any influence of the dye absorption in the solution outside the BM structure. For three different dye concentrations in the ethanol solutions, **Figure 5.10** shows the evolution of the transmission spectra measured with this device at analysis positions varying by approximately 0.15 mm along the sample. A similar set of spectra is shown in **Figure 5.11**, this time recorded in reflection mode. Clearly the spectra experience an overall shift which we attribute to a progressive increase in the total thickness of the BM from about 2480 to 2750 nm in this observation range. The series of spectra with a high concentration of dye in the solution shows a net decrease in the intensity of peak **P_1** that must be attributed to the light absorbed by the dye. In addition, the analysis of the curves obtained when representing **P_2-P_1** vs. **P_2** clearly reveals an oscillatory variation that confirms the already discussed modulation effects associated with the anomalous dispersion changes in refractive index associated to the presence of the absorption band of the dye. Similarly to the angle-dependent experiments in **Section 5.3.1.b)**, an accurate simulation of the spectra and of the decoupling in the position of **P_1** has been possible with the absorption and **$n(\lambda)$** curves reported in **Figure 5.4** for the 10^{-3} M Rh101 solution infiltrating the BM. These simulated spectra are presented in **Figure 5.12**.

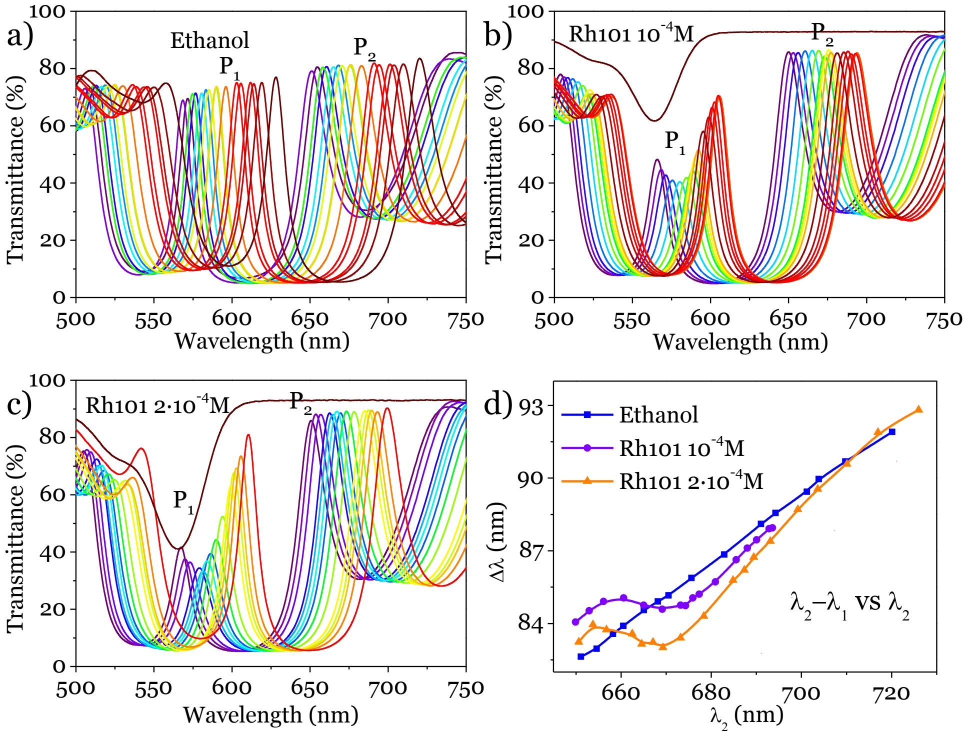

Figure 5.10. a)-c) Series of UV-vis transmission spectra for the infiltrated large BM of variable thickness recorded at different positions along the direction of increasing thickness. Each plot corresponds to a different concentration of Rh101 as indicated. The absorption band of the Rh101 ethanol solution is included for comparison. d) Plot of **P_2-P_1** vs. **P_2** for the 10^{-4} and $2{\cdot}10^{-4}$ M solutions depicting an anomalous deviation attributed to the overlapping of the high absorption band of the dye and the **P_1** resonant peak.

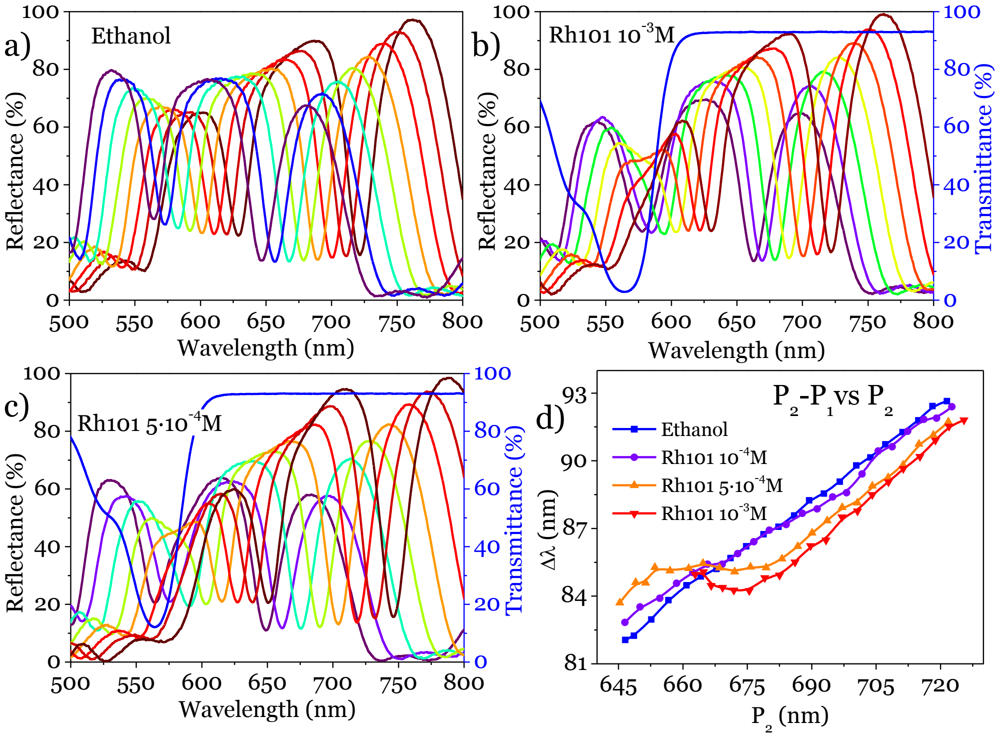

Figure 5.11. a)-c) Series of UV-vis reflectance spectra recorded with the infiltrated large BM of variable thickness at different positions along the direction of increasing thickness. Each plot corresponds to a different concentration of Rh101 as indicated. In b) and c) the blue plot refers to the blue axis and represents the UV-vis transmission spectrum of the infiltrating Rh101 solution. d) Plot of $\mathbf{P_2}$-$\mathbf{P_1}$ vs. $\mathbf{P_2}$ for the indicated dye concentrations.

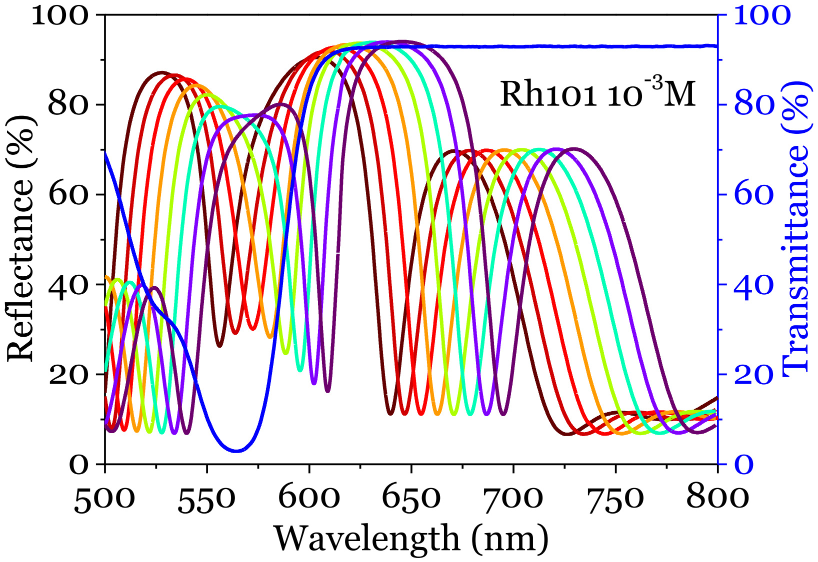

Figure 5.12. Series of simulated UV-vis reflectance spectra of a BM infiltrated with a solution of Rh101 10^{-3}M in ethanol. Each plot corresponds to the simulation of a BM of different thickness. The blue plot refers to the blue axis and represents the UV-vis transmission spectrum of the infiltrating Rh101 solution.

5.4. Discussion and Conclusions

The refractive index of a porous film infiltrated with a liquid is a convolution of both, the refractive index of the material (i.e. $\mathbf{n}_{\mathbf{TiO2}}$ or $\mathbf{n}_{\mathbf{SiO2}}$ in our case) and that of the liquid $\mathbf{n}_{\mathbf{L}}$ according to effective medium theory. For transparent liquids, **n** follows a smooth variation[23] with very little dispersion with wavelength between the positions of the two resonant peaks of the BM (for example $\mathbf{n}_{\mathbf{ethanol}}$ is 1.362 and 1.360 for λ= 564 and 646 nm, and the positions of the resonant peaks after infiltration of the BM with this liquid does not vary significantly, see **Figures 5.11 and 5.12**). The hypothesis sustaining the present chapter is precisely that infiltrating the BM with a liquid presenting an intense absorption band close to or overlapping the resonant peaks of the BM will modulate the position of this peak without affecting the others, i.e., the resonant effects in porous BMs can be selectively tuned by infiltration of highly absorbent liquids. The phenomenology described in the previous sections has been linked to the sharp increase of the dye absorption and the anomalous wavelength dispersion of the refractive index functions within a short interval of wavelengths. However, for a proper quantitative evaluation of the observed effects our simulations have shown that the experimental results can only be reproduced by assuming that the dye molecule infiltrating the BM should have an apparent absorption (and therefore an associated **n(λ)** function) much higher than that determined for the same solution in a cuvette or infiltrated in a simple layer of porous SiO_2 or TiO_2 films prepared by OAD as reported in **Figure 5.13**.

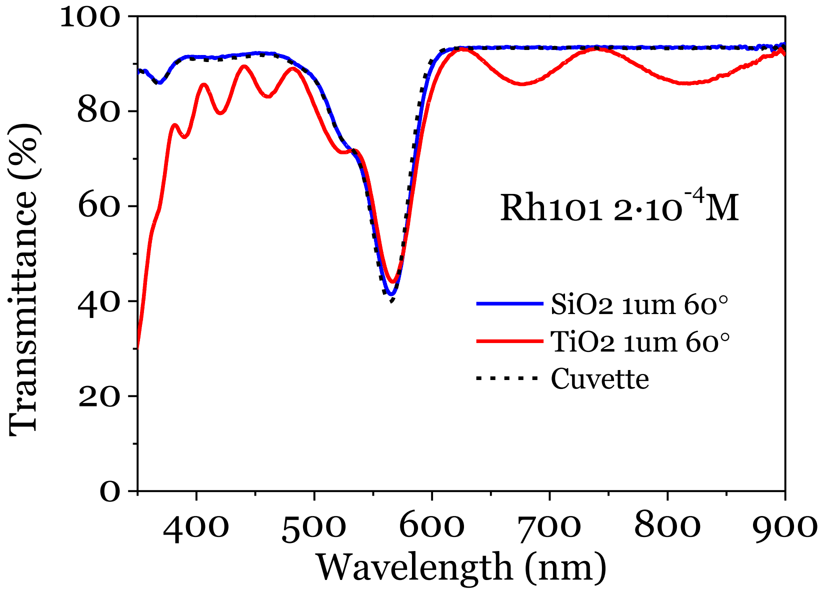

Figure 5.13. UV-vis transmission spectra of simple layers of SiO_2 and TiO_2 in a device *type 2* infiltrated with a selected solution of Rh101 and the transmittance spectrum of this solution (dashed line).

To account for this apparent contradiction, we have calculated the distribution of the electrical field through the BM and found the variation presented in **Figure 5.14.** In this figure we compare the transmission spectrum of the BM with the calculated electrical field along the device thickness coordinate and as a function of the wavelength. **Figures 5.14 a)** and **c)**, represent the total electric field within the BM (blue lines) as a function of the wavelength and reveal the existence of maxima at the wavelengths of the BM resonant peaks. Comparing both spectra, in the case with dye solution the electric field in the absorption region (**P**$_1$) clearly decreases as a result of the enhanced absorption. **Figures 5.14 b)** and **d)** break down the strength of the electric filed in a 3D plot as a function of the BM thickness besides the wavelength. These figures show the concentration of the electric field in the optical defect region at the wavelengths of the resonant peaks and a smooth increase along the whole layer in the other regions.

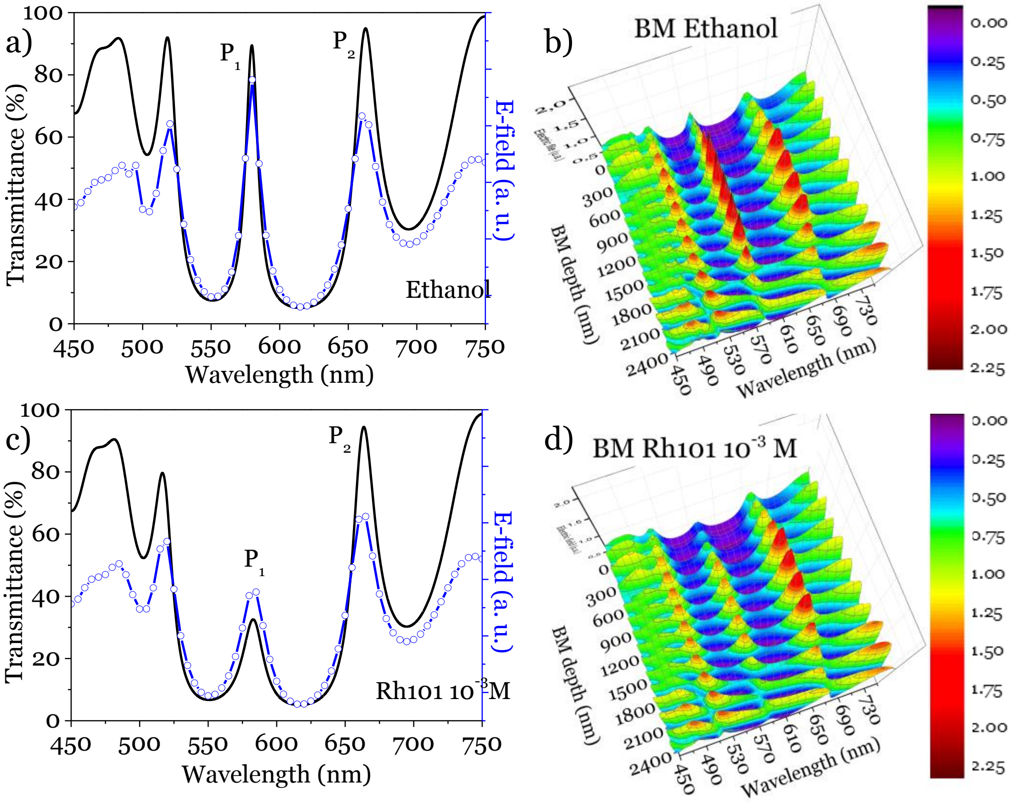

Figure 5.14. a) UV-vis transmission spectrum of the large BM infiltrated with ethanol and calculated electrical field strength as a function of the wavelength (blue axis). b) Color plot of the electrical field intensity as a function of both the wavelength and thickness coordinates for the latter case. c) & d) Ditto for a) & b) for the BM with an infiltrated Rh 101 solution 10^{-3} M in ethanol.

This behavior is exposed in **Figure 5.15** where a) clearly exhibits the concentration of the electric filed in the positions of the resonant peaks. The concentration of the electric field as well as its depletion in the presence of dye is shown in b). Note that the condition for a given wavelength to have a resonance at the BM is that an integer number of half wavelength equals the thickness of the defect layer of the BM. The black curve in **Figure 5.15b)** represents the case of a wavelength that doesn’t match this condition. Thus, this calculation reveals that the electric field is much smaller at the first resonant peak for the BM infiltrated with the dye solution. This selective decrease in the electrical field intensity at the wavelength region of the first resonant peak must be interpreted in the light of the observed modulation of resonant peak position: the electric field maximum at this wavelength zone becomes depleted because the dye takes advantage of the electric field concentration and the amount of light absorbed increases. This is manifested by an apparent increase in the dye absorption coefficient and in its associated **n(λ)** function which, in turn, provokes the decoupling of the resonant peak position.

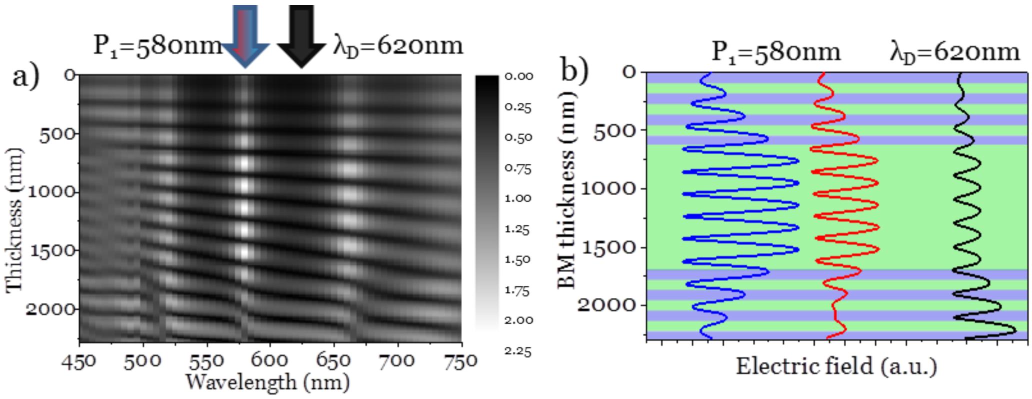

Figure 5. 15. a) Top view of **Figure 5.14b).** b) Representation of the electric field along the BM for P_1 (λ=580nm in this case) with (red line) and without (blue line) dye and for a wavelength corresponding to the depth of the spectrum (λ=620nm, black line).

In particular, the comparison of the calculated extinction coefficients determined for the BM and an equivalent single SiO_2 layer reveals an apparent enhancement of extinction coefficient, of ca. 0.020 μm^{-1}, that would correspond to a variation of ca. 0.025 units in the value of **n** at a wavelength of **P_1**. Herein, we have estimated these values by just measuring the decoupling of the resonant peak position using either the angular dependent effect (**Section 5.3.1.b)**) or the device with variable thickness (**Section 5.3.1.c)**).

Besides its fundamental interest to understand the optical behavior of infiltrated BM, the experiments reported in the previous sections and their explanation above open a way to experimentally asses the inhomogeneous distribution of electromagnetic fields in BM and other related Bragg mirror and planar resonant structures. Selectively localized enhancements of electrical fields has been systematically used for photovoltaic applications[24] where the incorporation of resonant structures has been utilized to increase the photon absorption capacity of the device by the selective confinement of light.

In relation with the objectives of this thesis work focused on, optofluidic sensing and applications, the results reported henceforth would open new possibilities for applications. For example, these results are relevant for the determination of the concentration of highly absorbent molecules following the position of the resonant peaks. We also believe that pH determination using dye indicators[25,26], formation of colored molecular complexes[27], molecular recognition[28–30] and other sensing applications might utilize the BM decoupling principle described in the present work as an efficient transduction mechanism for detection.

5.5 References.

1. Nishimura, S. *et al.* Standing Wave Enhancement of Red Absorbance and Photocurrent in Dye-Sensitized Titanium Dioxide Photoelectrodes Coupled to Photonic Crystals. *J. Am. Chem. Soc.* **125,** 6306–6310 (2003).
2. Colodrero, S. *et al.* Porous One-Dimensional Photonic Crystals Improve the Power-Conversion Efficiency of Dye-Sensitized Solar Cells. *Adv. Mater.* **21,** 764–770 (2009).
3. Colodrero, S., Mihi, A., Anta, J. A., Ocaña, M. & Míguez, H. Experimental Demonstration of the Mechanism of Light Harvesting Enhancement in Photonic-Crystal-Based Dye-Sensitized Solar Cells. *J. Phys. Chem. C* **113,** 1150–1154 (2009).
4. Chow, E., Grot, A., Mirkarimi, L. W., Sigalas, M. & Girolami, G. Ultracompact biochemical sensor built with two-dimensional photonic crystal microcavity. *Opt. Lett.* **29,** 1093 (2004).
5. Lee, M. R. & Fauchet, P. M. Nanoscale microcavity sensor for single particle detection. *Opt. Lett.* **32,** 3284 (2007).
6. Lee, M. R. & Fauchet, P. M. Two-dimensional silicon photonic crystal based biosensing platform for protein detection. *Opt. Express* **15,** 4530 (2007).
7. Nunes, P. S., Mortensen, N. A., Kutter, J. P. & Mogensen, K. B. Photonic crystal resonator integrated in a microfluidic system. *Opt. Lett.* **33,** 1623 (2008).
8. Mandal, S., Goddard, J. M. & Erickson, D. A multiplexed optofluidic biomolecular sensor for low mass detection. *Lab. Chip* **9,** 2924–2932 (2009).
9. Fink, Y. *et al.* A Dielectric Omnidirectional Reflector. *Science* **282,** 1679–1682 (1998).

10. Ganesh, N. *et al.* Enhanced fluorescence emission from quantum dots on a photonic crystal surface. *Nat. Nanotechnol.* **2,** 515–520 (2007).
11. Smolka, S., Barth, M. & Benson, O. Highly efficient fluorescence sensing with hollow core photonic crystal fibers. *Opt. Express* **15,** 12783 (2007).
12. Coscelli, E. *et al.* Toward A Highly Specific DNA Biosensor: PNA-Modified Suspended-Core Photonic Crystal Fibers. *IEEE J. Sel. Top. Quantum Electron.* **16,** 967–972 (2010).
13. Liu, Y., Wang, S., Park, Y.-S., Yin, X. & Zhang, X. Fluorescence enhancement by a two-dimensional dielectric annular Bragg resonant cavity. *Opt. Express* **18,** 25029 (2010).
14. Lola González-García, J. P.-B. Correlation lengths, porosity and water adsorption in TiO_2 thin films prepared by glancing angle deposition. *Nanotechnology* **23,** 205701 (2012).
15. González-García, L., Lozano, G., Barranco, A., Míguez, H. & González-Elipe, A. R. TiO2–SiO2 one-dimensional photonic crystals of controlled porosity by glancing angle physical vapour deposition. *J. Mater. Chem.* **20,** 6408–6412 (2010).
16. Oliva-Ramirez, M., Barranco, A., Löffler, M., Yubero, F. & González-Elipe, A. R. Optofluidic Modulation of Self-Associated Nanostructural Units Forming Planar Bragg Microcavities. *ACS Nano* (2015). doi:10.1021/acsnano.5b06625
17. *Kramers-Kronig Relations in Optical Materials Research*. **110,** (Springer-Verlag, 2005).
18. Joannopoulos, J.D., Johnson, S.G., Winn, J.N., Meade, R.D.: Photonic Crystals: Molding the Flow of Light. (Second edition) (eBook and Hardcover). at <http://press.princeton.edu/titles/8696.html>
19. Guo, M. *et al.* Enhanced Light Harvesting in Dye-Sensitized Solar Cells Coupled with Titania Nanotube Photonic Crystals: A Theoretical Study. *ACS Appl. Mater. Interfaces* **5,** 13022–13028 (2013).
20. Sánchez-Sobrado, O. *et al.* Environmentally responsive nanoparticle-based luminescent optical resonators. *Nanoscale* **2,** 936–941 (2010).
21. Sánchez-Sobrado, O. *et al.* Angular emission properties of a layer of rare-earth based nanophosphors embedded in one-dimensional photonic crystal coatings. *Appl. Phys. Lett.* **99,** 051111 (2011).
22. Frezza, L., Patrini, M., Liscidini, M. & Comoretto, D. Directional Enhancement of Spontaneous Emission in Polymer Flexible Microcavities. *J. Phys. Chem. C* **115,** 19939–19946 (2011).
23. RefractiveIndex.INFO - Refractive index database. at <http://refractiveindex.info/>

24. González-García, L., Idígoras, J., González-Elipe, A. R., Barranco, A. & Anta, J. A. Charge collection properties of dye-sensitized solar cells based on 1-dimensional TiO2 porous nanostructures and ionic-liquid electrolytes. *J. Photochem. Photobiol. Chem.* **241,** 58–66 (2012).
25. Castillero, P. *et al.* Active and Optically Transparent Tetracationic Porphyrin/TiO2 Composite Thin Films. *ACS Appl. Mater. Interfaces* **2,** 712–721 (2010).
26. Cano, M. *et al.* A transparent TMPyP/TiO2 composite thin film as an HCl sensitive optochemical gas sensor. *Sens. Actuators B Chem.* **150,** 764–769 (2010).
27. Sánchez-Valencia, J. R., Toudert, J., González-García, L., González-Elipe, A. R. & Barranco, A. Excitation transfer mechanism along the visible to the Near-IR in rhodamine J-heteroaggregates. *Chem. Commun.* **46,** 4372 (2010).
28. Yang, X. *et al.* High-sensitivity molecular sensing using hollow-core photonic crystal fiber and surface-enhanced Raman scattering. *J. Opt. Soc. Am. A* **27,** 977 (2010).
29. Khaing Oo, M. K., Han, Y., Kanka, J., Sukhishvili, S. & Du, H. Structure fits the purpose: photonic crystal fibers for evanescent-field surface-enhanced Raman spectroscopy. *Opt. Lett.* **35,** 466 (2010).
30. Cho, H., Lee, B., Liu, G. L., Agarwal, A. & Lee, L. P. Label-free and highly sensitive biomolecular detection using SERS and electrokinetic preconcentration. *Lab. Chip* **9,** 3360–3363 (2009).

Chapter 6

General conclusions

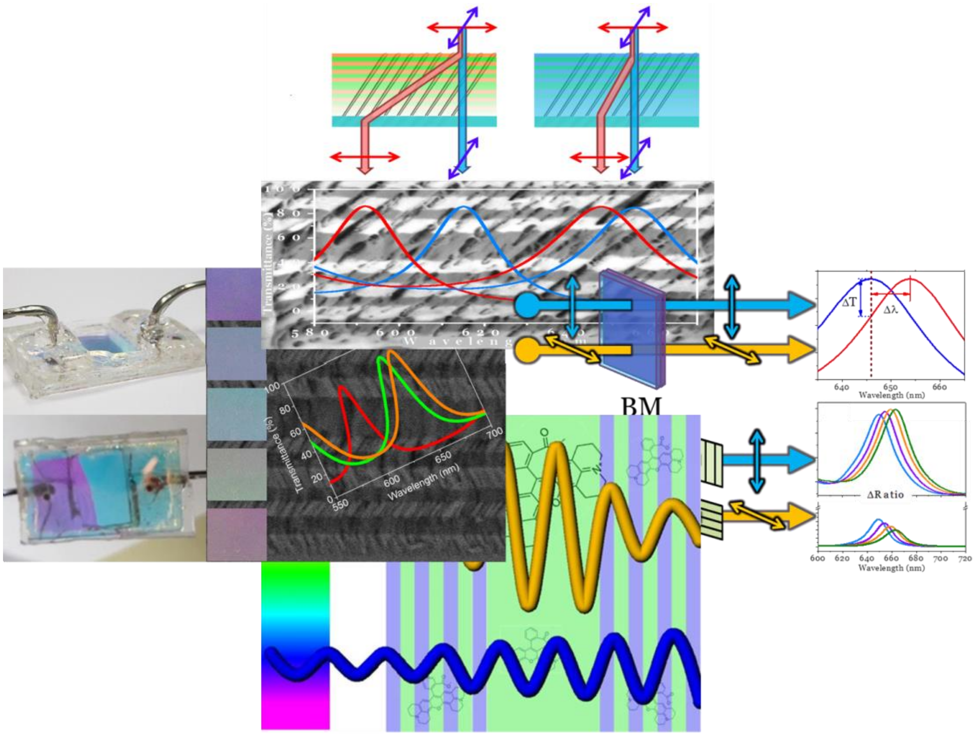

The present chapter gathers and summarizes the main achievements and conclusions of the work developed throughout the present thesis.

- In this thesis we have shown the electron-beam fabrication of PVD-OAD planar porous Bragg Microcavities (BM) consisting of successive layers of two oxides (SiO_2 and TiO_2) of different refractive indices.

- A strategy consisting of azimuthally turning the substrate from one layer to the next has been developed to minimize the light scattering effects and to manufacture different microstructures with *slanted*, *zigzag*, *chiral* and *vertical* nanocolumns.

- The high porosity of the BMs has enabled their integration as a part of a microfluidic device where liquids fill and circulate through the void space of these structures. This device allows the posterior optical testing of liquids within the BM.

- We have demonstrated that, a structural feature associated with PVD-OAD growth, named as *fence-bundling* association of nanocolumns, can be engineered to develop polarization active BMs acting as wavelength retarders.

- The liquid modulation of the retarder function of the BM has been shown as well as the possibility to use it to detect the orientation of polarization plane of light or for the analysis of liquids when integrated in microfluidic devices.

- Bragg microcavities have been used systematically to determine liquid solutions by several methods: measuring the position of the maximum; monitoring the transmittance at a selected wavelength and by turning the photonic structure by a certain angle to restore the maximum intensity of the resonance peak at its initial wavelength. In addition, as an up to date new method, the variation of the optical activity with the refractive index of the infiltrating liquid in the BM *zig-zag* has been also confirmed.

- BMs with large optical defects have been infiltrated with colored liquids and an enhanced absorption has been obtained as a result of the electric field concentration within the photonic structure. This is manifested by an apparent increase in the dye absorption coefficient and in its associated n(λ) function which, in turn, provokes the decoupling of the resonant peak positions.

- The experimental results obtained this thesis have been successfully reproduced in each case by simulation confirming their validity.

- The low volume of liquid required to fill the BMs makes easy the implementation of the developed technology into complex microfluidic systems where it could provide a simple and reliable method of analysis. In addition, it could be also employed to develop switchable optofluidic components for switchable photonic applications.

Chapter 7

Resumen en español.

Sensores optofluídicos de capas finas fabricados mediante deposición a Ángulo Oblicuo.

7.1. Análisis de líquidos con Microcavidades de Bragg Optofluídicas.

En este primer apartado presentamos la fabricación de Microcavidades de Bragg (MB) planas y su posible uso como transductor para el análisis de líquidos. Las MB son estructuras fotónicas sencillas que consisten en el apilamiento sucesivo de capas de dos índices de refracción distintos. En nuestro caso, hemos fabricado las MB alternando capar de SiO_2 y TiO_2 depositadas por evaporación electrónica en fase vapor a ángulo oblicuo (PVD-OAD)[15]. Esta configuración geométrica da lugar al crecimiento de capas compuestas por nanocolumnas inclinadas con alta porosidad y baja dispersión óptica.

En el desarrollo de este trabajo se han incorporado por primera vez capas PVD-OAD como componentes microfluídicos planos sin incurrir en la aparición de efectos de dispersión de luz y permitiendo circular líquidos a través de ellas con facilidad. Como resultado, se presenta que las MB planas se pueden usar de forma eficiente como transductores optofluídicos para determinar las concentraciones de disoluciones en líquidos o el análisis de mezclas líquidas. El trabajo se completa con ejemplos de la respuesta de estos dispositivos en casos prácticos y simulando su comportamiento mediante un modelo convencional de interferencia óptica.

La **Figura 7.1** muestra micrografías de microscopía electrónica de barrido (de sus siglas en inglés Scanning Electron Microscopy, SEM) de las MB fabricadas para ángulos de deposición de 70^0 y 80^0 que consisten en 2 conjuntos de 7 capas apiladas de TiO_2 y SiO_2 con una capa de SiO_2 de mayor espesor entre ellas como se muestra en el esquema. Los espesores de las capas de TiO_2 y SiO_2 rondan los 85 nm y el de la capa central, conocida como defecto óptico, los 200 nm. Las estructuras se depositaron mediante PVD-OAD a un ángulo cenital fijo de 70^0 y 80^0 para uno y otro caso girando los sustratos 90^0 entre capa y capa. Esta rotación azimutal es la responsable de la estructura columnar *quiral* de estas capas y se llevó a cabo para disminuir la dispersión de luz en las capas porosas.

Las ventajas de usar estos materiales y esta técnica para preparar las MB reside en el contraste de índice de refracción que presentan las capas de SiO_2 y TiO_2 preparadas por esta técnica (1.22/1.20 y 1.70/1.55 para SiO_2 y TiO_2 preparados a 70^0 y 80^0 respectivamente[22,23]) y su alto volumen de poros (aproximadamente 49% y 60% para estos ángulos de evaporación[22,23]). Estas características hacen que estos dispositivos ópticos resulten atractivos para un rango amplio de aplicaciones optofluídicas.

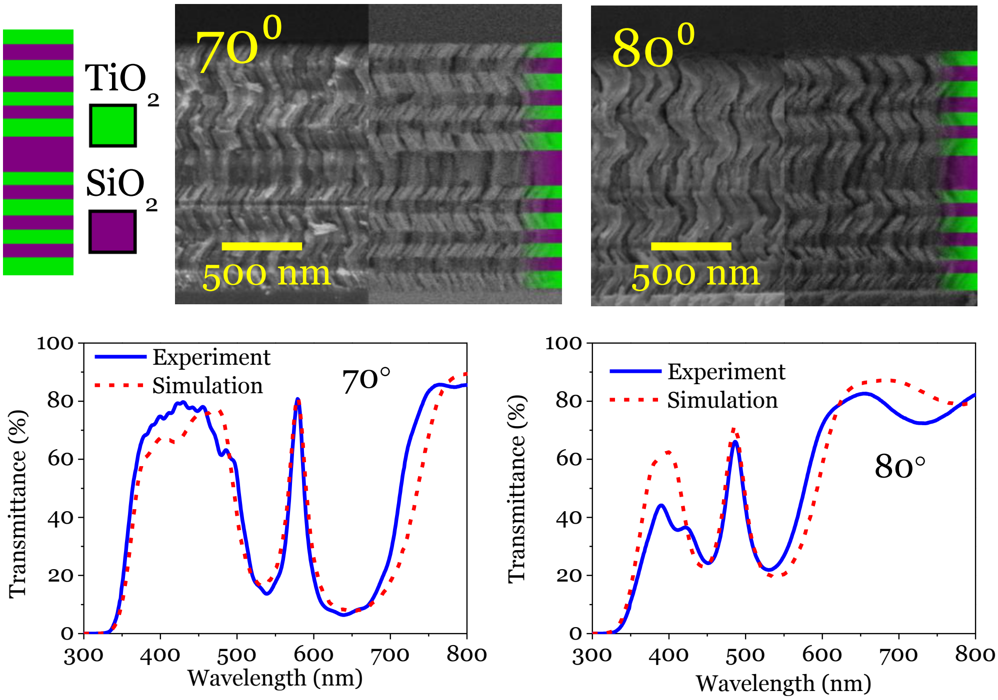

Figura 7.1. (Parte superior) micrografías SEM de las MB preparadas a ángulos de evaporación de 70^0 y 80^0. El esquema muestra el orden de apilamiento de las capas individuales que conforman la MB. (Parte inferior) Espectro de transmisión UV-visible de las MB preparadas a 70^0 (izquierda) y 80^0 (derecha). Como comparación, se añaden simulaciones de los espectros.

La respuesta óptica de las MB se midió en un espectrofotómetro (**Figura 7.1**) y presentan el comportamiento típico de MB, con una banda extensa de longitudes de onda prohibidas y una región estrecha permitida en ella conocida como pico resonante. Este pico resonante resulta de gran utilidad para una medida directa de cambios en la respuesta óptica. En los espectros además se observa que al concordar las medidas con las simulaciones se han reproducido correctamente las MB.

Para poder infiltrar las MB con líquidos y analizar su respuesta óptica, construimos un dispositivo microfluídico como se puede ver en la **Figura 7.2** Este consiste en colocar encima de nuestra MB otro sustrato de vidrio con dos orificios conectados cada uno a un tubo y que permiten la entrada y salida de líquidos. En la **Figura 7.3** se muestran los espectros de la MB depositada a 70^0 tras su infiltración con distintos líquidos. El resultado, que se corroboró mediante las simulaciones que se incluyen en la figura, es un desplazamiento del espectro a mayores longitudes de onda cuya magnitud está directamente relacionada con el índice de refracción del líquido. Esto se debe a que al llenar la porosidad cambia el índice de refracción efectivo de cada capa y por tanto su respuesta óptica. Para facilitar la medida del desplazamiento, nos centramos en medir las posiciones del pico resonante, que ofrece una referencia clara y directa para medir. Este comportamiento posibilita el uso de nuestro dispositivo microfluídico para identificar líquidos de distintos índices de refracción.

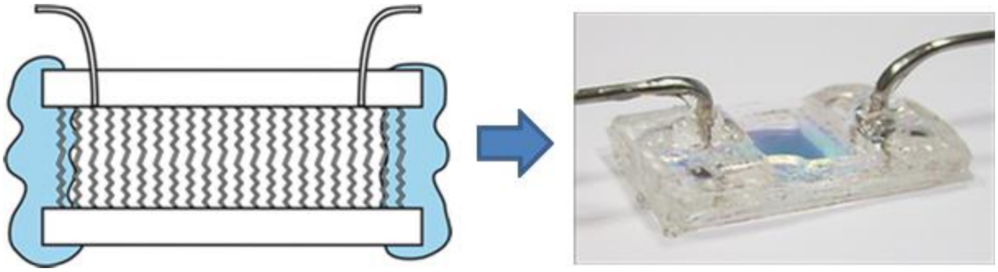

Figura 7.2. Esquema e imagen real del dispositivo microfluídico integrando la MB.

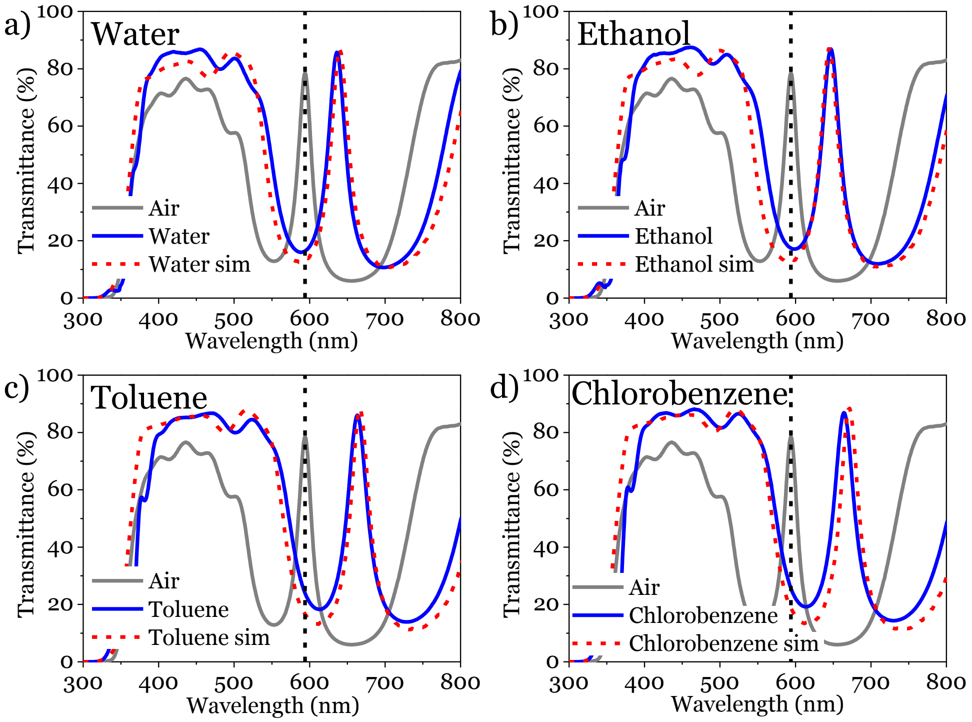

Figure 7.11. Espectros de transmisión UV-visible experimentales (líneas continuas) y simulados (líneas discontinuas) de la MB preparada a 70^0 infiltrada con: a) agua; b) etanol; c) tolueno; d) clorobenceno.

Partiendo de que nuestro dispositivo detecta variaciones de índice de refracción, se podría usar para determinar concentraciones de un soluto en disolución o medir mezclas de líquidos de distintos índices de refracción. Por ello, infiltramos disoluciones de cloruro sódico y de glucosa en nuestro dispositivo y obtuvimos que el desplazamiento del pico resonante depende linealmente de la concentración como puede verse en la **Figura 7.4**. Estas líneas pueden servir como curvas de calibración para cloruro sódico y glucosa en este dispositivo en particular.

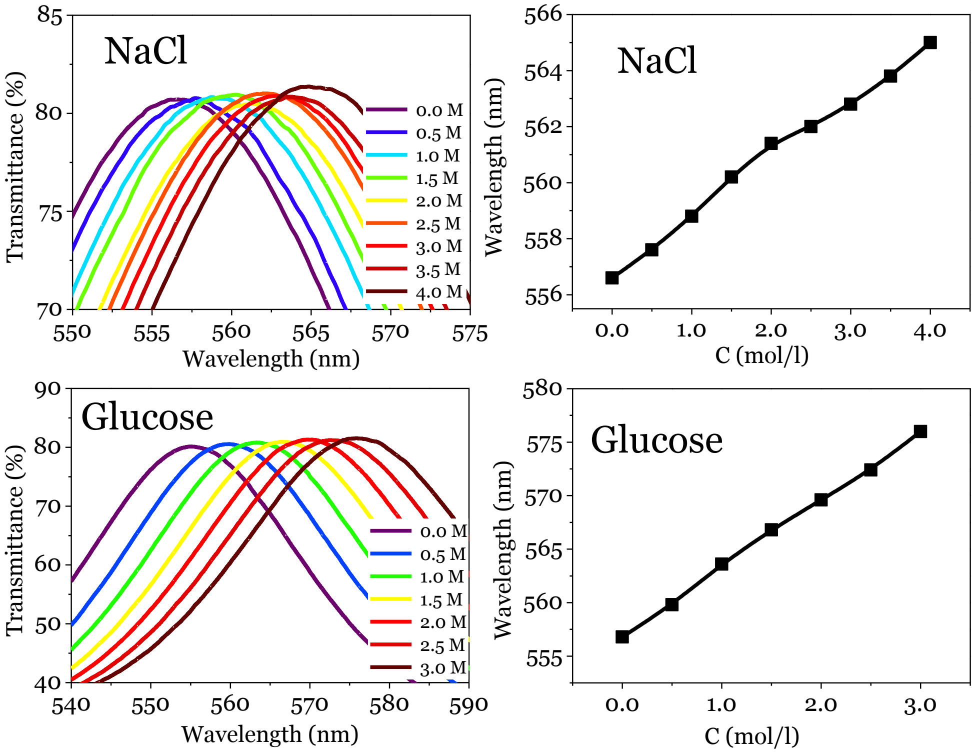

Figure 7.4. (Izquierda) Espectros de transmisión UV-visible centrados en el pico resonante de una BM depositada a 70^0 infiltrada con agua y con una serie de concentraciones de cloruro sódico y glucosa. (Derecha) Representación de la posición del pico resonante con respecto a la concentración para las disoluciones anteriores.

Como seguir el desplazamiento del pico resonante requiere un espectrofotómetro, en la **Figura 7.5** hemos propuesto un procedimiento de medida que permite soslayar su uso basándose en las propiedades de las MB. Un comportamiento conocido de las MB es el desplazamiento de su espectro a menores longitudes de onda cuando se gira con respecto a la dirección del haz de luz incidente. Como al infiltrarlo con un líquido el pico se desplaza a mayores longitudes de onda, nuestra propuesta consiste en balancear ese efecto girando el dispositivo para devolver el pico resonante a su posición inicial. Así, con un led sintonizado a la longitud de onda del pico resonante, un detector de intensidad y un goniómetro podríamos determinar la concentración de una disolución desconocida a partir de una calibración previa. En la **Figura 7.5** se aprecia cómo se relaciona la concentración de disoluciones de cloruro sódico y glucosa con el ángulo girado para restaurar el máximo de intensidad y aunque no tiene una relación lineal, sí presenta una buena dependencia que nos permite usarla como curva de calibrado.

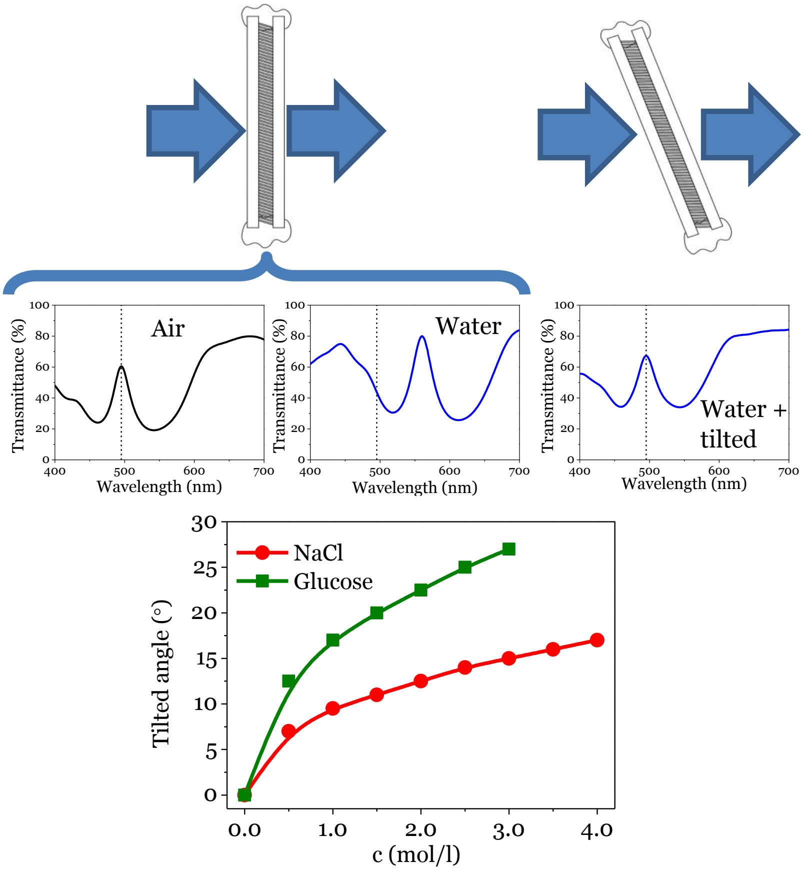

Figura 7.5. (Parte superior) Esquema que muestra la que muestra la variación de la posición del pico resonante de una MB cuando se llena con agua y el balanceo del efecto cuando se gira el dispositivo un ángulo determinado con respecto a la luz incidente. (Parte de abajo) Correlación entre los ángulos girados de la MB y la concentración de cloruro sódico y glucosa de acuerdo al procedimiento descrito en el esquema.

Los mismos conceptos analíticos basados en el desplazamiento del pico resonante y en el giro de la MB se probaron también con mezclas de agua (n=1,33) y glicerol (n=1,42) y con líquidos de la vida cotidiana como refrescos y aceites obteniéndose un comportamiento análogo al de las disoluciones presentadas.

7.2. Modulación Optofluídica de unidades nanoestructurales autoasociadas formando microcavidades de Bragg planas.

En esta sección se presenta la fabricación de MB mediante PVD-OAD con distintas microestructuras y se realiza un estudio estructural detallado de cada morfología. Además, se estudia en profundidad el comportamiento óptico de estas capas y se establece una relación entre las características estructurales y las propiedades ópticas de las distintas construcciones. Se completa el estudio con la caracterización y análisis de la respuesta optofluídica de las MB.

En el trabajo, se muestra por primera vez la fabricación de MB ópticamente activas de dos óxidos distintos mediante PVD-OAD que se comportan como retardadores ópticos dependientes de la longitud de onda. Debido a la porosidad de estas MB, se muestra que al infiltrarlas con líquidos su actividad óptica se puede sintonizar de forma metódica ajustando el índice de refracción del líquido infiltrado. El estudio se completó identificando las características nanoestructurales responsables de la actividad óptica de estas MB y reproduciendo mediante simulación su comportamiento polarizador. Con este fin, se desarrolló un modelo óptico simple donde cada capa de la MB presenta carácter birrefringente en un grado que depende del índice de refracción del líquido infiltrado.

Tanto la composición como la configuración de espesores de las MB, son iguales que en el apartado anterior para el ángulo de deposición 70º variando sólo la morfología. En la **Figura 7.6** se presentan las 4 microestructuras que hemos conferido a las MB. Estas microestructuras se consiguieron manteniendo el sustrato en la misma posición durante el proceso completo de deposición en el caso de la microestructura *inclinada*, girando el sustrato acimutalmente entre capa y capa para las microestructuras en *zigzag* (180º) y *quiral* (90º como en el apartado anterior) y continuamente (40 rpm) en el caso *vertical*.

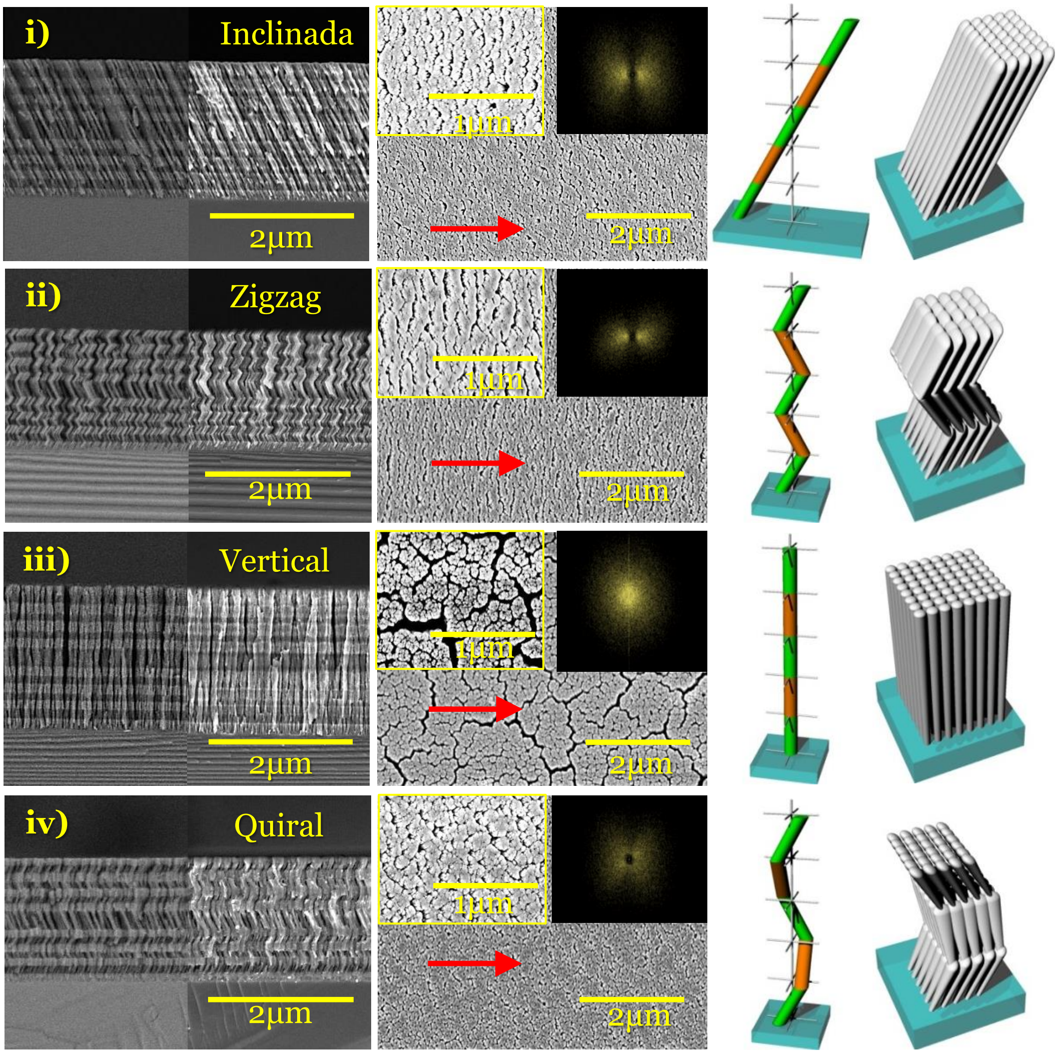

Figura 7.6. i-iv) Micrografías SEM de las 4 microestructuras de MB de sección transversal (izquierda) y vista superficial (derecha) en dos escalas con zum en el recuadro superior izquierdo. El otro recuadro corresponde a la transformada de Fourier de la micrografía ampliada. Los esquemas de la derecha representan la configuración geométrica ideal de las distintas capas que conforman las MB.

En la **Figura 7.7** se muestran los espectros de transmitancia óptica de las cuatro construcciones. Sorprendentemente las dos primeras microestructuras tienen carácter birrefringente mientras que las otras dos son prácticamente insensibles a cambios en la polarización. Gracias a un análisis combinado en nuestras MB de micrografía SEM y haz de iones focalizados (se sus siglas en inglés Focused Ion Beam, **FIB**) hemos conseguido identificar la asociación lateral de columnas, un fenómeno conocido como *apilamiento*[31,32] (del inglés *bundling*), como la característica crítica que determina la presencia de birrefringencia en las microestructuras *inclinada* y *zigzag*. En concordancia con este resultado, las microestructuras *quiral* y *vertical* que carecen de este apilamiento debido a sus condiciones especiales de crecimiento, no presentan cambios apreciables al ser interrogadas con luz polarizada.

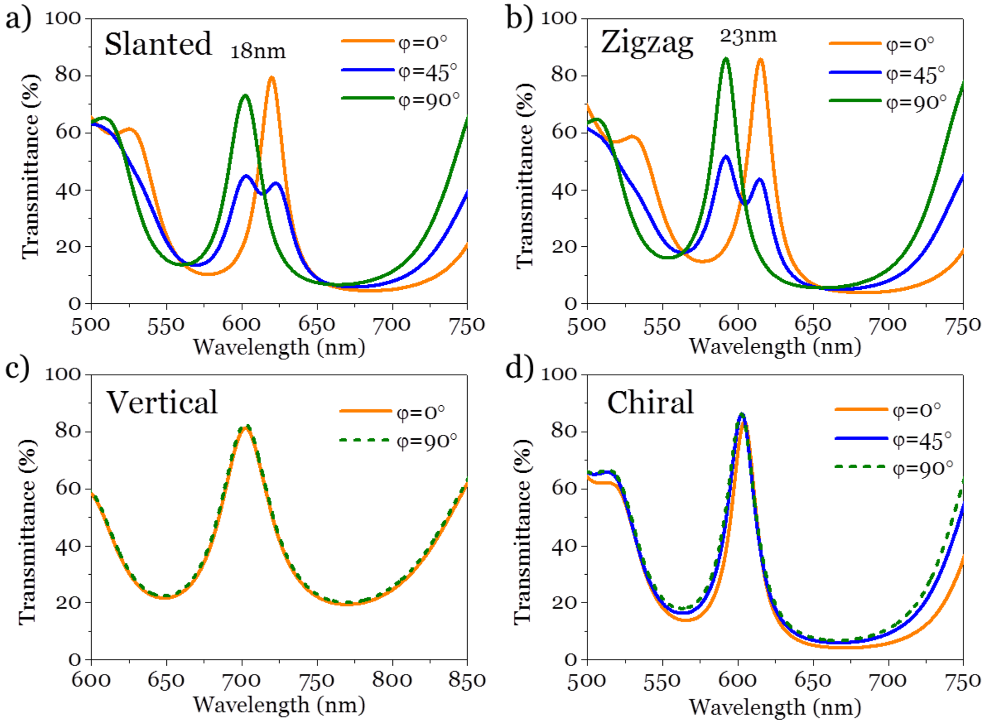

Figure 7.7. Espectro de transmisión óptica en torno al pico resonante para las MB a) *inclinada*, b) *zigzag*, c) *vertical* y d) *quiral*. El ángulo φ representa el ángulo que forma el plano de polarización de la luz con respecto a la dirección perpendicular al flujo de material durante el crecimiento (línea roja en la Figura 7.6.)

Debido a la presencia del este apilamiento lateral de nanocolumnas, las microestructuras *inclinada* y *zigzag* se comportan como retardadores ópticos o láminas cuarto de onda[35]. Con el objeto de investigar el carácter retardador de la MB *zigzag*, en la parte inferior de la **Figura 7.8** se puede observar su respuesta óptica cuando se orienta formando 45° con respecto al eje de polarización de la luz entre polarizadores cruzados y alineados. La luz transmitida en este caso reproduce aproximadamente la forma del espectro de la MB y muestra el carácter retardador de la construcción *zigzag*.

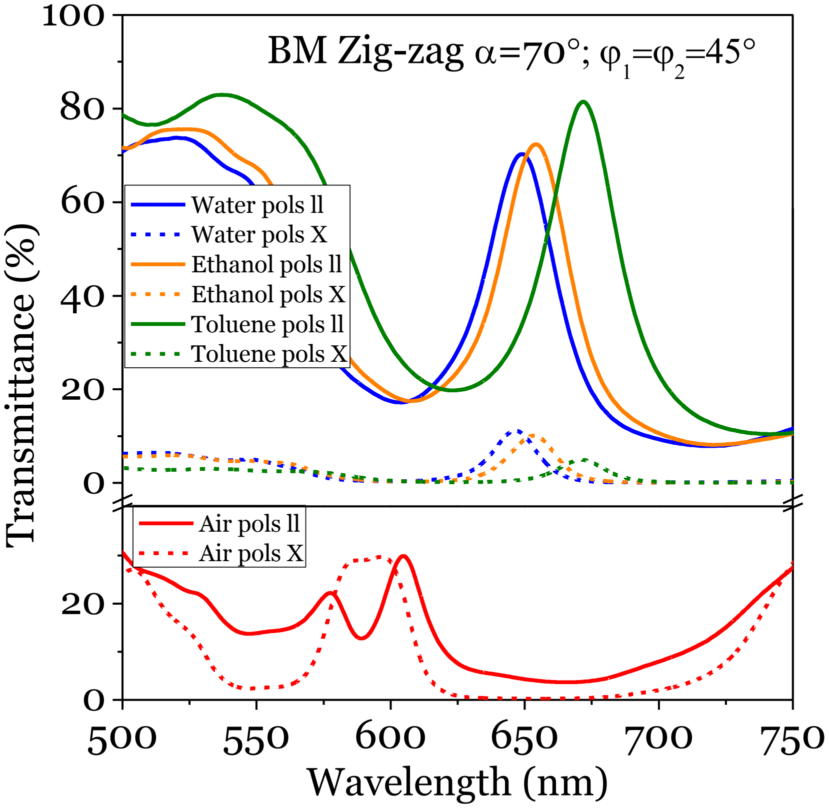

Figura 7.8. Sintonización optofluídica del carácter retardador de la MB *zigzag*. Espectros de transmitancia óptica registrados con la muestra girada 45° con respecto al eje de polarización de la luz y situada entre polarizadores cruzados (líneas discontinuas) y alineados (líneas discontinuas).

El siguiente paso de nuestro estudio consistió en estudiar la respuesta optofluídica de la MB *zigzag*. Para ello la encapsulamos en un dispositivo como el de la **Figura 7.2** y estudiamos su respuesta óptica con luz polarizada infiltrándola con distintos disolventes. La **Figura 7.9** muestra como al llenarse los poros, además del desplazamiento a mayores longitudes de onda descrito en el apartado anterior, el carácter birrefringente se atenúa y los picos resonantes de las distintas polarizaciones se acercan. El valor del decrecimiento de la birrefringencia está directamente ligado al índice de refracción del líquido infiltrado.

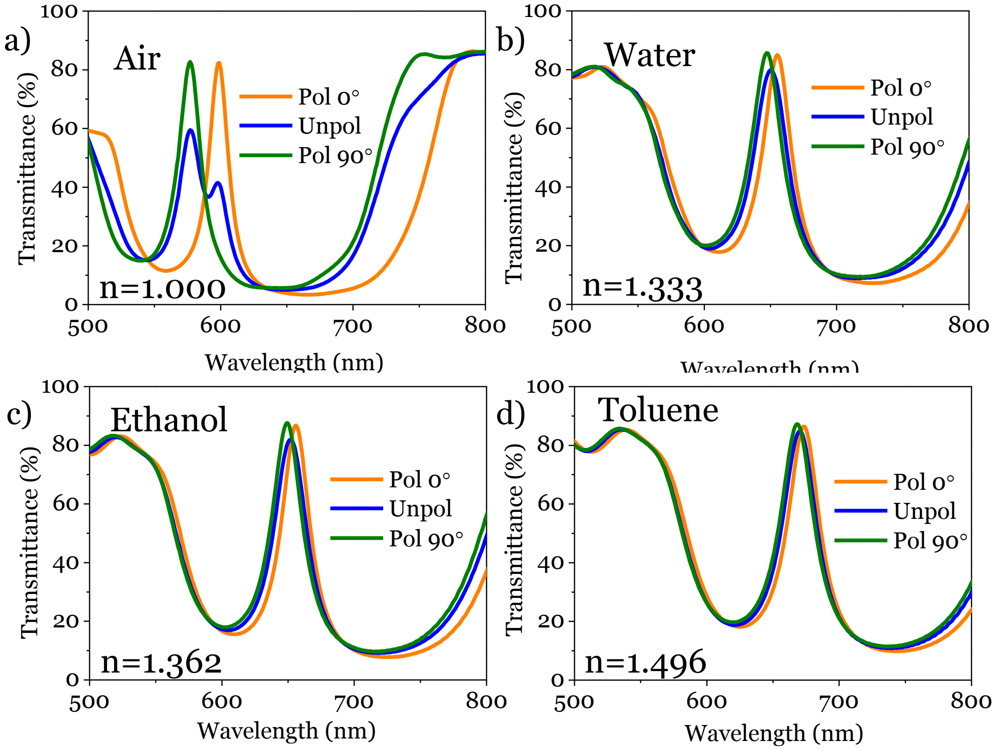

Figura 7.9. Espectros de transmisión óptica de la sintonización optofluídica del comportamiento birrefringente de la MB *zigzag* registrado con luz polarizada y no polarizada. Infiltrada en cada caso con: a) aire, b) agua, c) etanol y d) tolueno.

En la parte superior de la **Figura 7.8** se verifica que el carácter retardardor de la MB se puede sintonizar mediante la infiltración de líquidos y al igual que en el caso de la birrefringencia, disminuye al aumentar el índice de refracción del líquido infiltrado. Como muestra la figura, al disminuir el carácter retardador de la MB, la transmitancia tras polarizadores cruzados disminuye y tras alineados aumenta de forma proporcional.

El comportamiento descrito de las MB se simuló usando un modelo óptico sencillo que tenía en cuenta la porosidad y los cambios de índice debido al llenado de líquidos, con lo que corroboramos teóricamente nuestras hipótesis experimentales.

7.3. Análisis Optofluídico con Microcavidades de Bragg ópticamente activas preparadas por Deposición a Ángulo Oblicuo.

Una vez desentrañado el comportamiento optofluídico de las MB nanoestructuradas, hemos aplicado este conocimiento para realizar análisis de líquidos. Como la respuesta de nuestras MB depende del índice de refracción del líquido infiltrado, a través de él hemos propuesto tres métodos distintos de análisis usando concentraciones de glucosa.

En esta sección, se han usado tres métodos para analizar nuestras MB con concentraciones de glucosa extrayendo de cada uno de ellos una curva de calibrado que se pueda usar para el análisis de líquidos. Hemos comparado la respuesta optofluídica de la microestructura *quiral* y la *zigzag* estableciendo dos procedimientos de medida a partir del desplazamiento a mayores longitudes de onda que se produce al infiltrar, y un tercero aprovechando la modificación de la actividad óptica de la MB *zigzag*.

Para este estudio hemos usado dos MB porosas, una con estructura *quiral* (**Figuras 7.1** y **7.6 iv)**) y otra con estructura *zigzag* (**Figura 7.6 ii)**) fabricadas por PVD-OAD y con la misma distribución de espesores que en los apartados anteriores. Para posibilitar su infiltración y manejo encapsulamos ambas en un dispositivo microfluídico como el de la **Figura 7.2**.

En primer lugar nos vamos a centrar en explotar las posibilidades analíticas de las MB a partir de su espectro de transmitancia óptica. Como veíamos en la **Figuras 7.3**, **7.4** y **7.9**, al infiltrar estas MB porosas, el espectro se desplaza hacia mayores longitudes de onda, efecto que se puede rastrear fácilmente siguiendo la posición del pico resonante. En el caso de la MB *zigzag*, seguiremos los picos resonantes que aparecen para cada polarización (**Figura 7.7**), que al acercarse uno a otro como se ve en la **Figura 7.9**, darán respuestas ópticas distintas. La **Figura 7.10** muestra las posiciones de los picos resonantes de la MB *quiral* y de la *zigzag* para las dos polarizaciones frente a distintas concentraciones de glucosa. Como ya se comentó en la **Figura 7.4**, el desplazamiento de los picos presenta una dependencia lineal con la concentración de glucosa debido a su relación con el índice de refracción. Mediante este método se aprecia que el dispositivo con la BM *quiral* es el que presenta mayor *sensibilidad*, definida ésta como la pendiente de la recta.

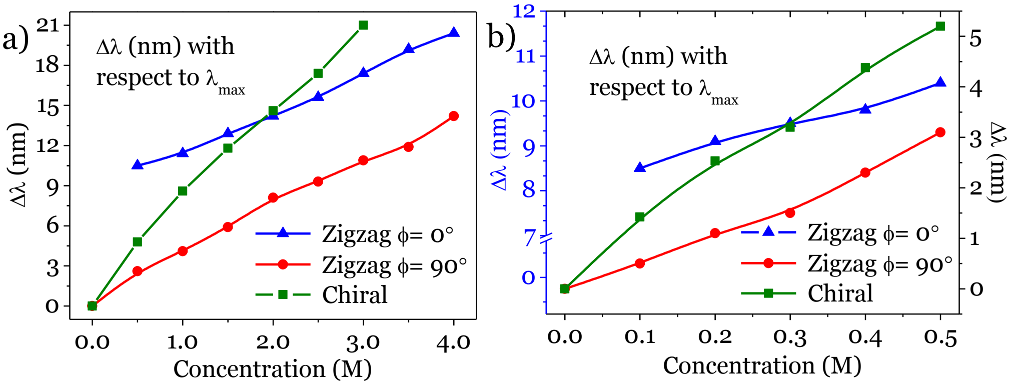

Figura 7.10. a) Desplazamiento de los picos resonantes frente a la concentración de glucosa para la MB *quiral* y la *zigzag* para las dos polarizaciones. b) Lo mismo para bajas concentraciones.

Otro método para medir variaciones en el espectro de transmitancia al infiltrar consiste en medir el cambio en transmitancia en una longitud de onda fija, en concreto en la posición del pico resonante. De esta forma se saca partido de la forma escarpada del pico resonante al desplazarse el espectro. La **Figura 7.11** muestra los cambios en transmitancia en la posición del pico resonante para las MB *quiral* y *zigzag*. En el caso de la MB *zigzag* con luz polarizada en la dirección del *apilamiento* (ϕ=0°), hemos tomado como referencia la longitud de onda del pico de la otra polarización (ϕ=90°) como se muestra en la **Figura 7.11 a)**. De esta forma, nos hemos situado mediante una referencia intrínseca del espectro en la zona de mayor cambio de la transmitancia al encontrarse en la "ladera" del pico resonante. La **Figura 7.11 b)** muestra cómo, gracias a este cambio de referencia, un pequeño desplazamiento en longitudes de onda supone un desplazamiento considerable en transmitancia. En las **Figuras 7.11 c)** y **d)** se presentan los valores de variaciones en transmitancia con respecto a la concentración de glucosa. La MB *quiral* presenta ligeramente más sensibilidad que la *zigzag* en sus dos polarizaciones. Sin embargo, al analizar bajas concentraciones, la MB *zigzag* para ϕ=0° presenta la mayor sensibilidad gracias a la estrategia seguida para colocarnos en su zona de mayor variación.

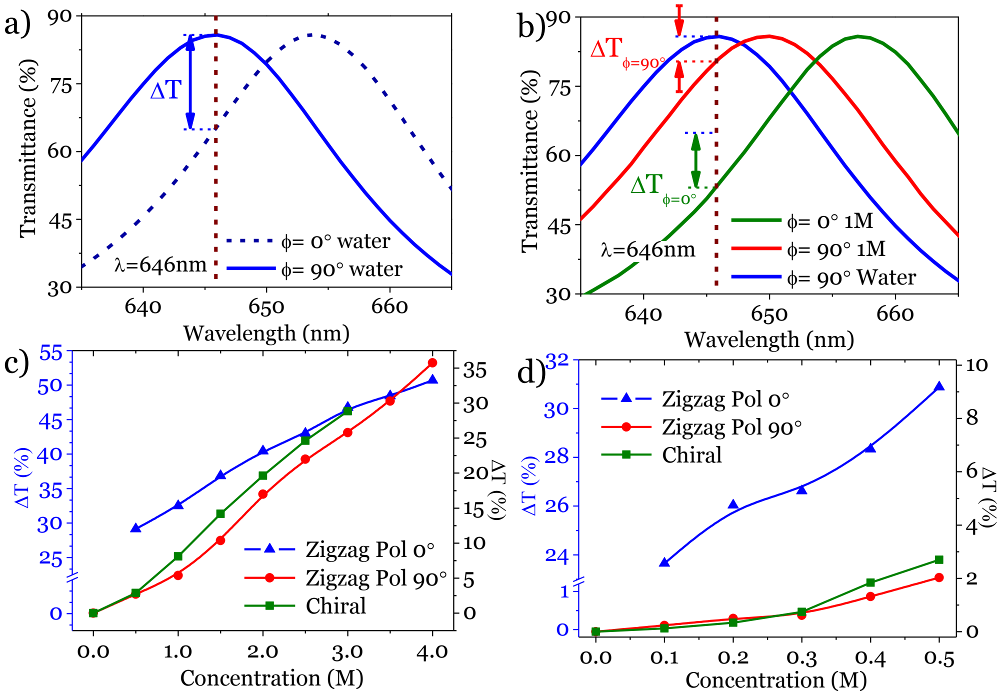

Figura 7.11. a) y b) Espectro de transmitancia óptica de la MB *zigzag* con agua a), y con una concentración de glucosa 1M para explicar la metodología de media. c) Diferencia en transmitancia con respecto al pico resonante en función de la concentración para la MB *quiral* y la *zigzag* con las dos polarizaciones. d) Igual que c) para bajas concentraciones.

El último método propuesto se basa en la sintonización de la actividad óptica descrita en el apartado anterior por lo que el análisis sólo se ha realizado con la MB *zigzag*. Para ello hemos infiltrado y medido la MB *zigzag* entre polarizadores cruzados y alineados como se muestra en la **Figura 7.12**. La cuantificación de este efecto la hemos hecho a través del cociente entre la cantidad de luz transmitida para polarizadores alineados y cruzados como se puede ver en c) y d). El valor de este cociente frente a la concentración de glucosa describe una curva de calibrado que puede usarse con fines analíticos. Una ventaja de este método reside en que al tratarse de un cociente de intensidades, se evitan desviaciones por posibles inestabilidades de la lámpara y se puede evitar sustituyéndolo por un fotodiodo.

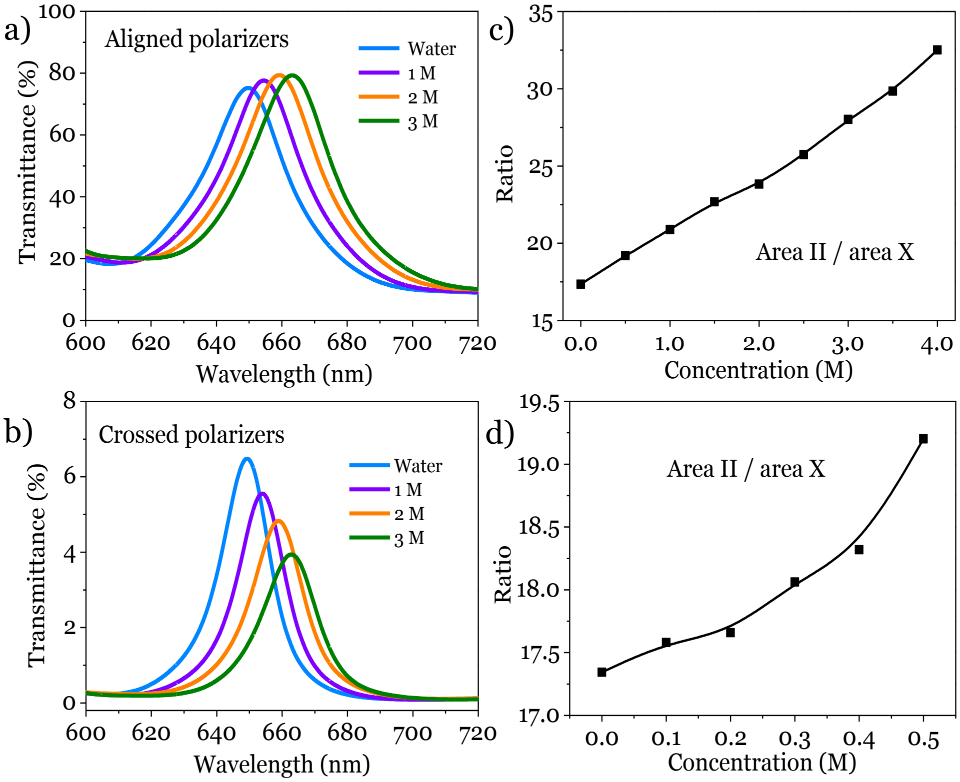

Figura 7.11. Espectro de transmitancia óptica de la MB *zigzag* alrededor del pico resonante. La muestra estaba girada acimutalmente 45° y se midió en configuración de polarizadores a) alineados y b) cruzados. c) Cociente entre la intensidad de luz transmitida en configuración de polarizadores alineados con respecto a cruzados frente a la concentración de glucosa. d) Igual que c) para bajas concentraciones.

7.4. Absorción colosal anómala de colorantes infiltrados en Microcavidades de Bragg Planas.

En las secciones anteriores se ha mostrado la utilidad de las MB porosas como transductores para el análisis de líquidos no coloreados. En esta sección vamos a extender el concepto y analizar líquidos coloreados que presenten un coeficiente de extinción alto para ver su efecto en las MB.

Dado que los colorantes presentan absorción dentro de un intervalo concreto de longitudes de onda, hemos usado MBs con un defecto óptico mayor que los de las secciones anteriores con el fin de obtener más de un pico resonante en la banda de transmisión prohibida. De esta forma, se ha usado la distancia entre los picos resonantes para analizar la absorción situando uno de ellos en la zona de absorción y el otro fuera como referencia. Además del esperado incremento del índice de refracción debido a la absorción del colorante[7], hemos encontrado efectos resonantes que involucran tanto al colorante como a la estructura fotónica y que dan lugar a una absorción exaltada que se manifiesta mediante un coeficiente de absorción colosal aparente.

En este análisis hemos usado dos MB porosas fabricadas por PVD-OAD, una con estructura *zigzag* y otra con estructura *inclinada* como ya se mostró en la **Figura 7.6**. La MB *inclinada* se creció en un sustrato de mayor tamaño y a una distancia más cercana a la fuente de deposición con la finalidad de obtener un gradiente de espesor en la muestra. Este gradiente de espesor se traduce en una variación de la posición del espectro de la MB hacia mayores longitudes de onda en el sentido del aumento de espesor de la capa. En esta ocasión, los dos apilamientos de 7 capas tienen la misma distribución de espesores que en los apartados anteriores sin embargo, el defecto óptico se fabricó de mayor espesor (∼1μm) dando lugar a la aparición de dos picos resonantes en la banda prohibida de transmitancia. La **Figura 7.12** muestra micrografías SEM de estas construcciones así como la respuesta óptica de la MB *zigzag* con luz polarizada.

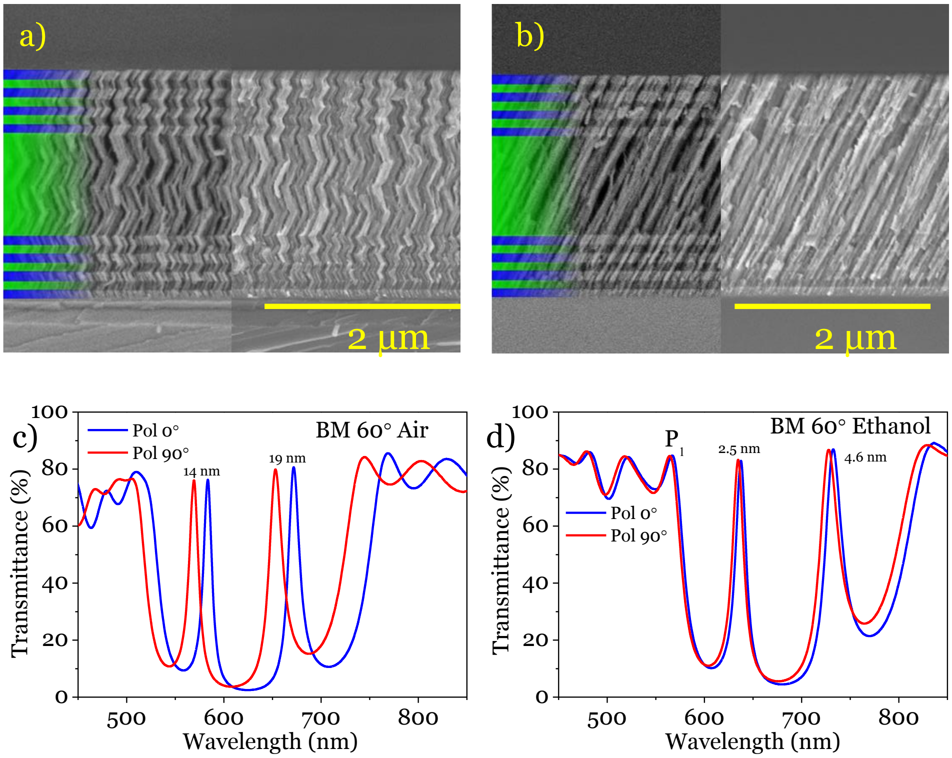

Figura 7.12 a) y b) Micrografías SEM de las MBs *zigzag* e *inclinada*. c) Espectro de transmisión óptica de la MB *zigzag* con luz polarizada. d) Igual que c) pero infiltrada con etanol.

Para poder analizarlas con líquidos, encapsulamos las MBs en los dos tipos de dispositivos microfluídicos que se pueden ver en la **Figura 7.13**. El *tipo 1*, es como el usado en los casos anteriores (**Figura 7.2.**), y el *tipo 2* es una cubeta de 125 µm de espesor que implementa la MB en una de sus caras.

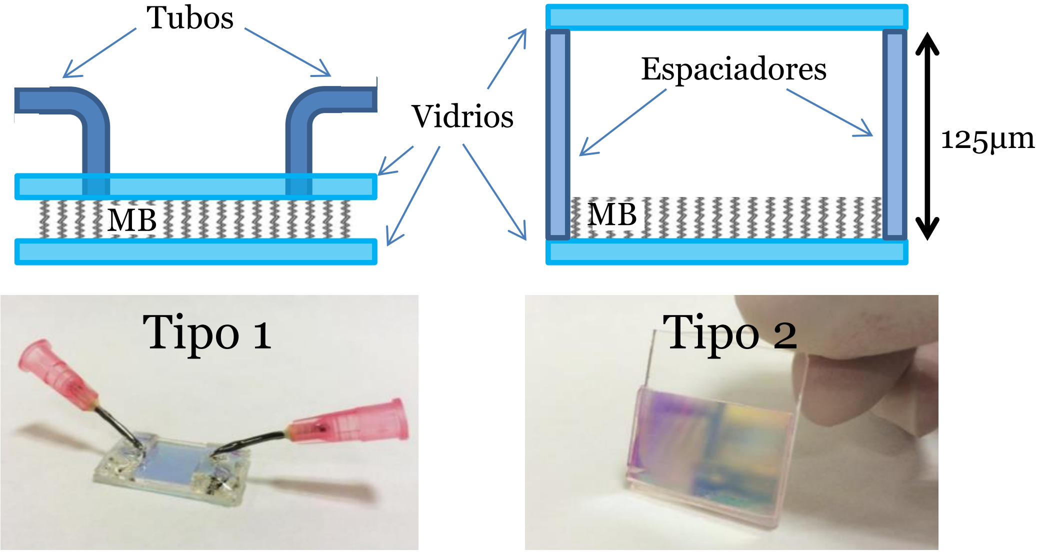

Figura 7.163. Esquemas y fotografías de los dispositivos microfluídicos tipo 1 y tipo 2 con la MB incorporada. Nota: el esquema no está a escala real.

En primer lugar, infiltramos la MB *zigzag* con disoluciones de distintas concentraciones de Rhodamina B (RhB) en etanol como se muestra en la **Figura 7.14**. Siguiendo las posiciones de los tres picos resonantes que aparecen en los espectros, vemos que **P_1**, que coincide con la zona de absorción de la RhB, presenta un desplazamiento anómalo con respecto a los que muestran los dos otros picos **P_2** y **P_3** (**Figura 7.14 d)**) cuando se aumenta la concentración. Este desplazamiento anómalo indica un incremento del índice de refracción del líquido infiltrado en esta zona del espectro y podrá caracterizarse usando como referencia interna la posición de otro pico resonante del espectro fuera de la zona de absorción del colorante, **P_2** o **P_3** en este caso.

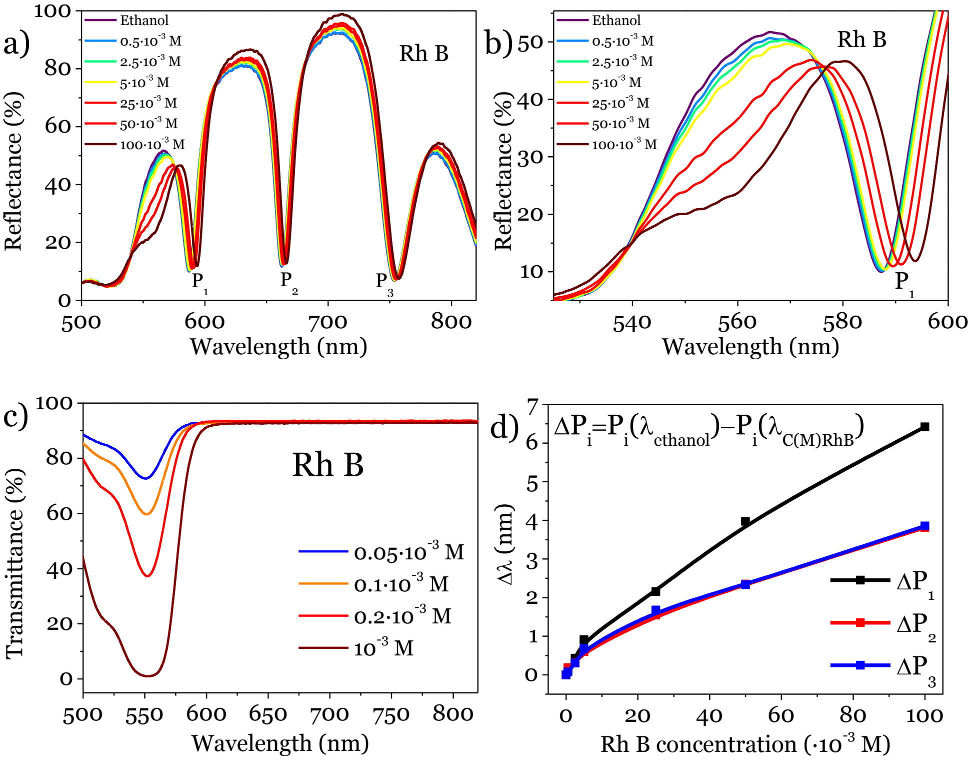

Figura 7.14. a) Espectros de reflectancia óptica de la MB *zigzag* infiltrada con etanol y concentraciones crecientes de RhB en etanol. b) Detalle ampliado de a) alrededor de **P_1**. c) Espectro de transmitancia óptica de disoluciones de RhB en etanol. d) Variaciones en la posición de los picos resonantes con respecto a la concentración de las disoluciones.

Para tener una información más detallada de este efecto, hemos recurrido a la respuesta angular de las MB (**sección 7.1**) que permite barrer la zona de absorción del colorante con uno de los picos resonantes, como se presenta en la **Figura 7.15**. En este caso se han usado distintas concentraciones de Rhodamina 101 (Rh101) para tener la absorción localizada en las inmediaciones de uno de los picos resonantes y se ha hecho un barrido angular para cada caso con un dispositivo *tipo 1*. En las figuras a) y b) se puede apreciar una caída en la intensidad del pico resonante de la izquierda al pasar por la zona de absorción del colorante. La figura c) muestra la diferencia de la posición de un pico resonante con respecto al otro y, mientras que para el caso del etanol la curva es monótona decreciente, conforme aumenta la concentración de colorante se produce una oscilación en la curva que sigue las variaciones del índice de refracción debida a la absorción en cada caso.

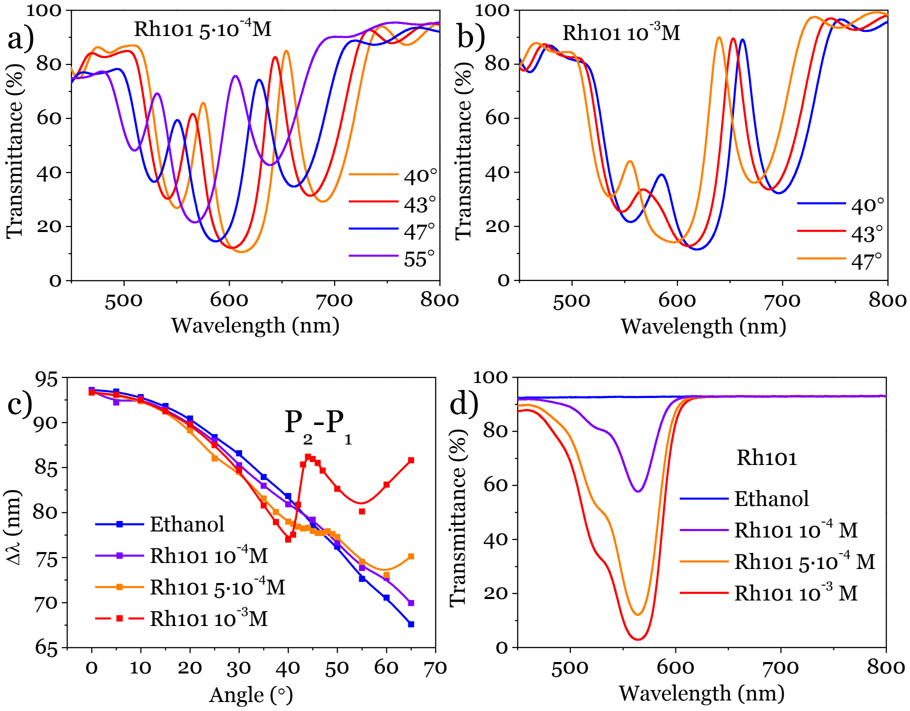

Figura 7.15 a) Espectros de transmisión óptica registrados para la MB *zigzag* con respecto al ángulo de incidencia de la luz para una concentración de Rh101 de 10^{-3} M. b) Análogo a a) pero para Rh101 de $5 \cdot 10^{-4}$ M. c) Representación de $\mathbf{P_2}$-$\mathbf{P_1}$ para los casos estudiados. d) Espectro de transmisión óptica para disoluciones de Rh101 analizadas.

Otra forma de analizar el efecto del colorante consistió en usar la MB *inclinada* que gracias a su gradiente de crecimiento nos proporciona una posición de su espectro distinta en cada punto. De esta forma, un desplazamiento lateral en la posición de la muestra nos proporcionó un barrido con un pico resonante sobre la región con el colorante. Encapsulamos esta MB en un dispositivo *tipo 2* y realizamos su análisis tanto en transmitancia (omitida en este resumen) como en reflectancia, asegurándonos así de medir únicamente el colorante dentro de la estructura fotónica. **La figura 7.16** muestra los espectros de reflectancia de la MB *inclinada* para un barrido de posiciones y distintas concentraciones de Rh101. La figura d) muestra cómo la diferencia entre las posiciones de los picos resonantes siguen reproduciendo la oscilación en los índices de refracción detectada en el análisis angular con la MB *zigzag*.

Los resultados obtenidos mediante los dos métodos se simularon mediante el programa WVASE y se obtuvo que para justificar los desplazamientos de los picos resonantes, la absorción del colorante tenía que verse exaltada dentro de la MB. Este efecto, que matemáticamente se reproduce como un aumento del coeficiente de absorción (**α**), se atribute a que la concentración del campo eléctrico de la luz que se produce en la estructura fotónica[8], provoca una mayor absorción por parte del colorante. El comportamiento del campo eléctrico en el interior de nuestras MB se simuló con el programa Filmstar y se obtuvo que, para las longitudes de onda del pico resonante, se producía una concentración del campo eléctrico que corrobora nuestra hipótesis experimental.

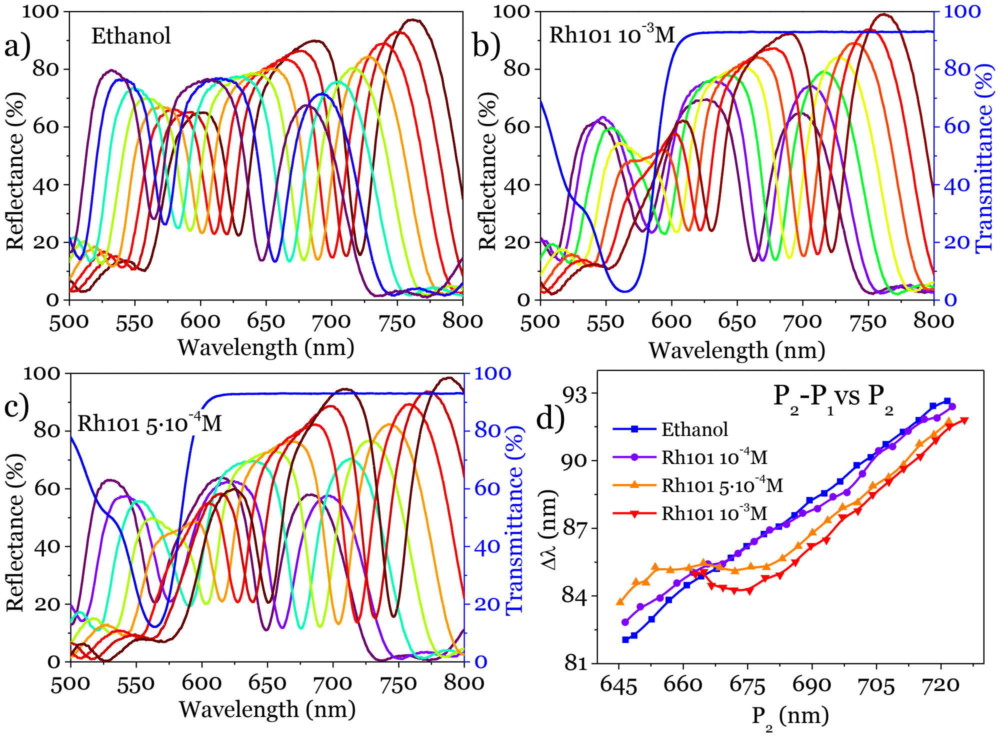

Figura 5.17. a)-c) Espectros de reflectancia óptica para varias posiciones de la MB *inclinada*. Cada espectro corresponde a una concentración distinta de Rh101 como se indica en cada caso. En b) y c) se presentan además los espectros de transmitancia de las concentraciones de Rh101 analizadas medidas en una cubeta de 125 µm. d) Representación de **P_2-P_1** frente **P_2** para las concentraciones de Rh101 estudiadas.

7.5. Referencias.

1. González-García, L., Lozano, G., Barranco, A., Míguez, H. & González-Elipe, A. R. TiO2–SiO2 one-dimensional photonic crystals of controlled porosity by glancing angle physical vapour deposition. *J. Mater. Chem.* **20,** 6408–6412 (2010).
2. Lola González-García, J. P.-B. Correlation lengths, porosity and water adsorption in TiO_2 thin films prepared by glancing angle deposition. *Nanotechnology* **23,** 205701 (2012).
3. Gonzalez-García, L. *et al.* Tuning Dichroic Plasmon Resonance Modes of Gold Nanoparticles in Optical Thin Films. *Adv. Funct. Mater.* **23,** 1655–1663 (2013).
4. van Kranenburg, H. & Lodder, C. Tailoring growth and local composition by oblique-incidence deposition: a review and new experimental data. *Mater. Sci. Eng. R Rep.* **11,** 295–354 (1994).
5. Stagon, S. P., Huang, H., Baldwin, J. K. & Misra, A. Anomaly of film porosity dependence on deposition rate. *Appl. Phys. Lett.* **100,** 061601 (2012).
6. Handbook of Optics, Volume I - Fundamentals, Techniques, and Design - Handbook of optics second edition Vol 1 - - Bass M.pdf. at <http://iate.oac.uncor.edu/~manuel/libros/Optics/Handbook%20of%20optics%20second%20edition%20Vol%201%20-%20%20-%20Bass%20M.pdf>
7. *Kramers-Kronig Relations in Optical Materials Research*. **110,** (Springer-Verlag, 2005).
8. Nishimura, S. *et al.* Standing Wave Enhancement of Red Absorbance and Photocurrent in Dye-Sensitized Titanium Dioxide Photoelectrodes Coupled to Photonic Crystals. *J. Am. Chem. Soc.* **125,** 6306–6310 (2003).